Department of Oceanography

University of Cape Town

Climate Change Impact on Ecosystems of Prince Edward Islands:

Role of Oceanic Mesoscale Processes

Sarah Asdar

A thesis presented for the Degree of

Doctor of Philosophy

University of Cape Town June 2018

Declaration

This thesis is a presentation of my original work, written with the full support of my supervisors. Wherever contributions of others are involved, every effort is made to indicate this clearly, with due reference to the literature. Aside from the guidance provided by my supervisors, I have received no assistance, except as acknowledged.

Signed by candidate

Supervisors:

Associate Prof. Isabelle Ansorge
Department of Oceanography, University of Cape Town
Cape Town, South Africa

Dr. Pierrick Penven
Institut de Recherche pour le Développement, Laboratoire d'Océanographie Physique et Spatiale
Plouzané, France

Dr. Julie Deshayes
Centre National de Recherche Scientifique, Laboratoire d'Océanographie et du Climat Expérimentations et Approches Numériques
Paris, France

Acknowledgements

There are many people that I would like to express my gratitude to.
Firstly, I would like to thank my supervisors Pierrick Penven, Julie Deshayes, Isabelle Ansorge and Thomas Gorgues, without whom nothing would have been possible.
Pierrick,thank you for your honesty, for your enthusiasm, for countless and constructive discussions of all kinds (scientific or not), for your immense availability and for precious modelling expertise.
Julie, thank you for your energy, for your infinite inspiration, for your benevolence, for believing in me more than myself and for your undisputed faith in science that motivated me every day.
I am very thankful for all animated discussions we had, your ideas, your advices and your encouragement (and for so many other things)!
Isabelle, thank you for believing in me, for sharing your knowledge about Prince Edward Islands and for giving me the opportunity to go to Marion Island and see with my own eyes (other than through a screen) my region of study. These oceanographic cruises were wonderful experiences that will remain etched in my mind forever.
Thomas, thank you for your support, especially during the last weeks (the best!), for your proofreading, your precious advices and your kindness. Thank you all for supporting me and for your guidance during this unique adventure. I enjoyed doing science with you (may we continue to do so)!
I gratefully acknowledge DEA, especially Marcel Van Der Berg, for sharing the precious mooring and CTD data with me.
A big "thank you" to the whole UCT team/Upper leeuwen Street: Serena for your great computing expertise, your patience and your pedagogy; Fab for ambushes on Thursday, Friday (Monday?); Malou for ambushes on the other days of the week; Ele for your support at UCT and at Upper Leeuwen Street and cat's videos; Rachel for your incredible good mood; Marion because it is you; Charlie for your humour and your melodious voice; Fehmi, Danee, Laura, Jeremy, Laura because we were in the same boat! And now, this is the turn of the Brest City team. To Isis, Este, Anjela, Justine and Clement for all the good times, for supporting me and encouraging me when I had the "PhD blues". To my parents for all their love and unconditional support. Thank you.

Abstract

The subantarctic Prince Edward Islands (PEIs, 47°S-38°E) are classified as isolated and hostile regions, in which the terrestrial and marine ecosystems are relatively simple and extremely sensitive to perturbations. The island's location, between the Subantarctic Front (SAF) and the Polar Front (PF), bordering the Antarctic Circumpolar Current (ACC) provides an ideal natural laboratory for studying how organisms, ecological processes and ecosystems respond to a changing climate in the Southern Ocean. Recent studies have proposed that climate changes reported at the islands may correspond in time to a southward shift of the ACC and in particular of the SAF. This southward migration in the geographic position of major ocean fronts is likely to coincide with dramatic changes in the distribution of species and total productivity of this region. However, there are other sources of variability in the hydrodynamic conditions around the PEIs: upstream of the islands, at the South West Indian Ridge (SWIR), a region of high eddy kinetic activity produces mesoscale features that directly irrigate the PEIs and may impact their marine environment. Based on satellite altimetry in that region, the positions of the SAF and PF were found to be highly variable at interannual and monthly time scales. They also revealed a significant long-term southward trend which was highlighted at the Southern Ocean scale. The mesoscale activity also showed an interannual and intra-annual variability and a decrease in eddy kinetic energy over 24 years was observed in the region. At a more local scale, we highlighted that the archipelago's environment was impacted by the mesoscale features produced at the SWIR. The temperature, the mixed layer and velocities recorded between the islands were clearly affected by the eddies passing in the vicinity of the PEIs. Moreover, a large signal dominating the main current time series appeared to be a tidal signal, another important driver of variability of the circulation in between the two islands. On a second hand, an idealised model configuration was designed for the PEIs region to study the mesoscale eddy properties and the physical mechanisms of their formation at the ridge. The Eddy Available Potential Energy revealed a maximum of energy around 800 m depth, confirming the deep reaching characteristic of the eddy originated in the region and suggested the presence of a local energy source at this depth. This eddies activity was shown to be the result of a combination of barotropic and baroclinic instabilities occurring at the ridge. Finally, we investigated on the potential consequences of a southward shift of the SAF in the region of the islands. Because the model was idealised, it allowed us to simulate an SAF southward shift by shifting the initial and boundary conditions. The main result was the clear decrease of mesoscale activity in the region which could potentially impact the ecosystems of the PEIs.

Contents

List of Figures

List of Tables

List of Acronyms

ABFZ Andrew Bain Fracture Zone

ACC Antarctic Circumpolar Current

ADT Absolute Dynamic Topography

EKE Eddy Kinetic Energy

MOC Meridional Overturning Circulation

PEIs Prince Edward Islands

PF Polar Front

PFZ Polar Frontal Zone

SACCF Southern ACC Front

SAF SubAntarctic Front

SAM Southern Annular Mode

SB Southern Boundary

STF Subtropical Front

SWIR South West Indian Ridge

1 Introduction

Contents

1.1 Context

The climate of our planet is governed largely by the ocean which, by absorbing carbon dioxide (CO_2) and heat from the atmosphere, moderates climate and its changes. In this context of climate change, the Southern Ocean plays a critical role (Le Quéré et al., 2007; Tollefson, 2016). Although the latter is the most isolated ocean of any human activity, many observers have reported significant changes in ecosystems like a decline in Antarctic krill densities in the South West Atlantic sector or a long term downward trend in the populations of some seals and sea birds in the Indian and Pacific sectors of the Southern Ocean (Atkinson et al., 2004; Constable et al., 2014). Since the beginning of the industrial era, the concentration of CO_2 has greatly increased in the ocean. By absorbing copious amount of anthropogenic CO_2 (approximately 30% of the total human emissions of CO_2, Le Quéré et al., 2010), the ocean contributes to slow down the rate of global warming. However, this carbon uptake is not distributed homogeneously around the globe. The Southern Ocean is a crucial sink for anthropogenic CO_2: more than 40% of anthropogenic CO_2 is absorbed by the ocean south of 40^oS (Khatiwala et al., 2013). The effectiveness of the Southern Ocean to store CO_2 decreased between 1981 and 2004 (Le Quéré et al., 2007). Other studies suggest that several processes could decrease or slow down this natural carbon sink (Tollefson, 2016). Carbon is only one piece of the Southern Ocean puzzle. As a consequence of excessive greenhouse gas emissions, beyond absorption by the ocean, ocean waters have warmed and observations reveal that this warming is faster for the Southern Ocean than the global ocean average (Gille, 2002; Gille, 2008; Böning et al., 2008). These changes in the Southern Ocean are likely to be associated with changes on the westerly wind belt that encircle Antarctica. Those winds have strengthened and shifted southwards presumably causing a southward shift of the Antarctic Circumpolar Current (ACC). Besides such a warming event, the Southern Ocean have revealed a strong freshening signal over the past few decades which could be explained by changes in sea-ice drift and thickness (Haumann et al., 2016). Global warming impacts differ between regions around Antarctica (East Antarctica and West Antarctica) but is particularly pronounced at the subantarctic islands (Constable et al., 2014). It is in this environment that subantarctic islands, including Prince Edward Islands, are found, lying between the subantarctic Front and the Polar Front. They form ideal sentinels to climate change (Ansorge et al., 2014b).

1.2 The Southern Ocean: important key in the global ocean system

1.2.1 The Southern Ocean

Over the past 40 million years, Antarctica gradually detached itself from the other continents opening the Drake passage and allowing Antarctic water masses to flow all around Antarctica (Barker and Burrell, 1977; Siegert et al., 2008). The Southern Ocean is the principal conduit for exchanges between the Pacific, Atlantic and Indian Oceans. It is bounded to the south by the Antarctic continent and extends up to 30°S. This ocean has two major indentations, the Weddell Sea and the Ross Sea and two significant constrictions, the Drake Passage between the Antarctic Peninsula and South America as well as south of Tasmania and New-Zealand (Figure 1.1). Dominating the Southern Ocean's

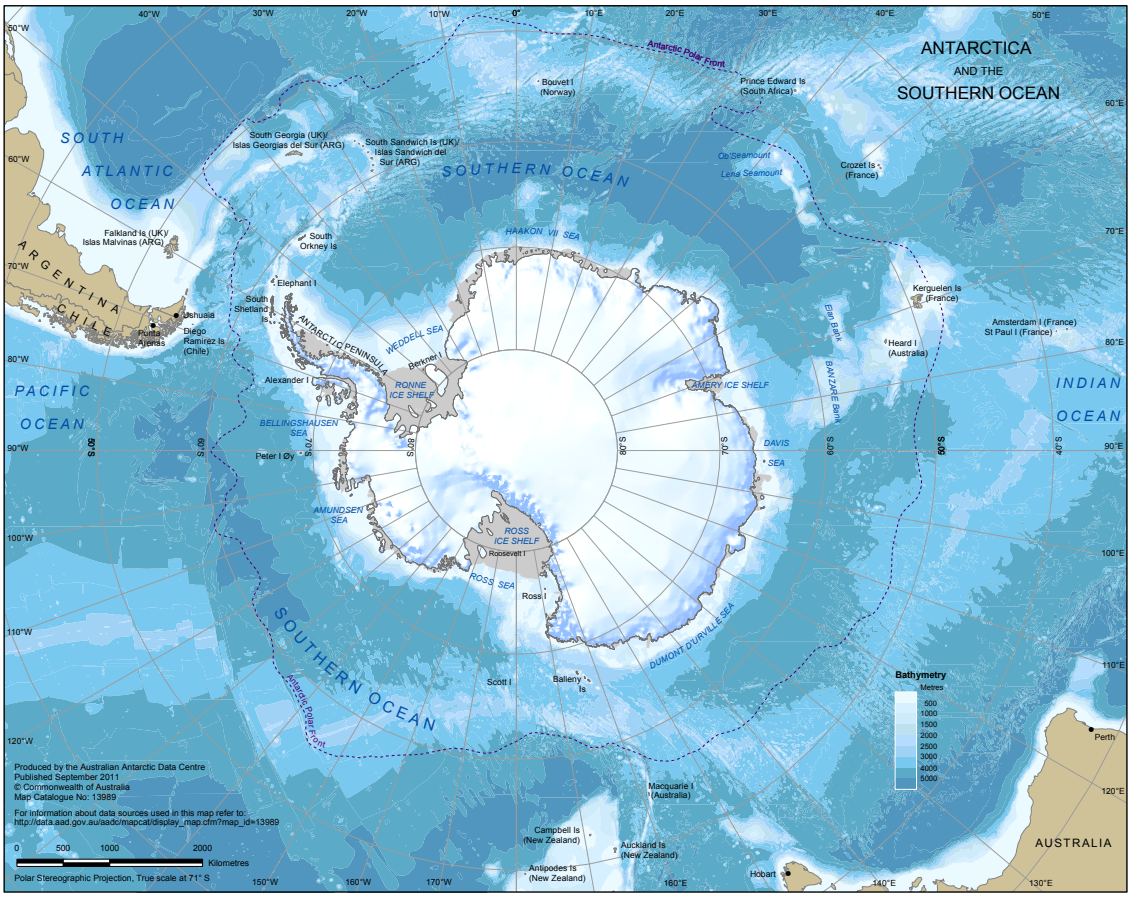

Figure 1.1: *Bathymetry of the Southern Ocean. The dashed line represents the position of the Polar Front (Source: Australian Antarctic Division :* `http://data.aad.gov.au/aadc/mapcat` *).*

large scale circulation, the strong flowing eastward Antarctic Circumpolar Current (ACC), which extends unbroken along a roughly 25 000 km path around Antarctica, is the primary way by which heat, salt and nutrients are exchanged between different ocean basins and

thus a primary factor shaping Southern Ocean ecosystems (Tynan, 1998). These inter-basin exchanges are important mechanisms for the Global Overturning Circulation which plays a central role in the climate system (Marshall and Speer, 2012; Rintoul and Naveira Garabato, 2013; Schmittner et al., 2013) and allow climate anomalies to be transmitted from one basin to another.

The absence of land barriers in the atmosphere has also a big influence on the atmospheric dynamics. The Southern Ocean is dominated by strong westerly winds between the latitudes 40^{o}S and 60^{o}S, known as the roaring forties and the furious fifties, which have been formidable for sailors for a long time.

The Southern Annular Mode (SAM) is the dominant mode of atmospheric variability in the Southern Ocean (Thompson et al., 2000; Marshall, 2003). It is a measure of the pressure gradient between the polar and subpolar regions of the Southern hemisphere, describing the north-south movement of the westerlies circling Antarctica. During its positive phase, westerlies are more intense around 60°S, shifting the maximum westerlies to the south. The SAM impacts many variables such as the sea surface temperature (Thompson and Solomon, 2002; Sen Gupta et al., 2006) or sea-ice (Simpkins et al., 2012; Holland et al., 2017), and also chlorophyll (Lovenduski and Gruber, 2005). But it is not the only climate mode to impact the Southern Ocean. Hoskins et al. (1981) showed that Niño Southern Oscillation generates atmospheric Rossby waves that travel polewards.

The Southern Ocean, characterised by its remoteness and hostile environment, makes observations challenging, especially during austral winter. Satellites and observations programs, such as Argo project[1], have brought many progresses in the knowledge of the ocean. By having deployed more than 3700 Argo floats since 2000, this project has allowed us to take a giant leap forward. Furthermore, top predators, such as elephant seals, have been instrumented (Guinet et al., 2013) in order to directly observe their behaviour and also to get unique oceanographic data. Since 2004, over 500,000 vertical profiles of temperature and salinity have been collected[2]. In spite of all this incredible improvement of observing the Southern Ocean, the spatial and temporal cover is still rudimentary and observation efforts need to be sustained.

1.2.2 Understanding the structure of the Antarctic Circumpolar Current

The ACC, driven predominantly by the prevailing westerly winds that overly the Southern Ocean, is characterised by a large zonal transport and a weak and deep stratification (Rintoul and Naveira Garabato, 2013). The ACC, bounded by the Subtropical Front (STF) to the north and by the Southern Boundary (SB) to the south (Orsi et al., 1995),

[1] http://www.argo.ucsd.edu/
[2] http://www.meop.net/)

is mostly constrained by the bathymetry. Bottom topography has a strong influence on its circulation and intensity due to the topographic Beta effect (Craneguy and Park, 1999; Moore et al., 1999; Sinha and Richards, 1999; Lacasce, 2000; Dong et al., 2006). In flat-bottom areas, large spatial variability of the ACC can be induced by atmospheric forcing (Sallée et al., 2008; Graham et al., 2012). The ACC carries 134±11.2 Sv (± standard deviation of the annual average) (Whitworth and Peterson, 1985) through Drake Passage, 160 Sv south of Africa (Park et al., 2001) and 147±10 Sv south of Australia (Rintoul and Sokolov, 2001; 1 Sv = $10^6 m^3.s^{-1}$). The major part of the flow associated with the current is concentrated at a number of circumpolar fronts (Deacon, 1982; Orsi et al., 1995 Belkin and Gordon, 1996) separating water masses of different characteristics and associated with jets (Sokolov and Rintoul, 2007). The principal fronts are: the Subantarctic Front (SAF) which demarcates the northern boundary of the Polar Frontal Zone (PFZ), the Polar Front (PF) marking the southern boundary of the Polar Frontal Zone and the beginning of the Antarctic Zone and the Southern ACC Front (SACCF). The fronts are usually defined by subsurface hydrological features (Orsi et al., 1995). The intense westerlies

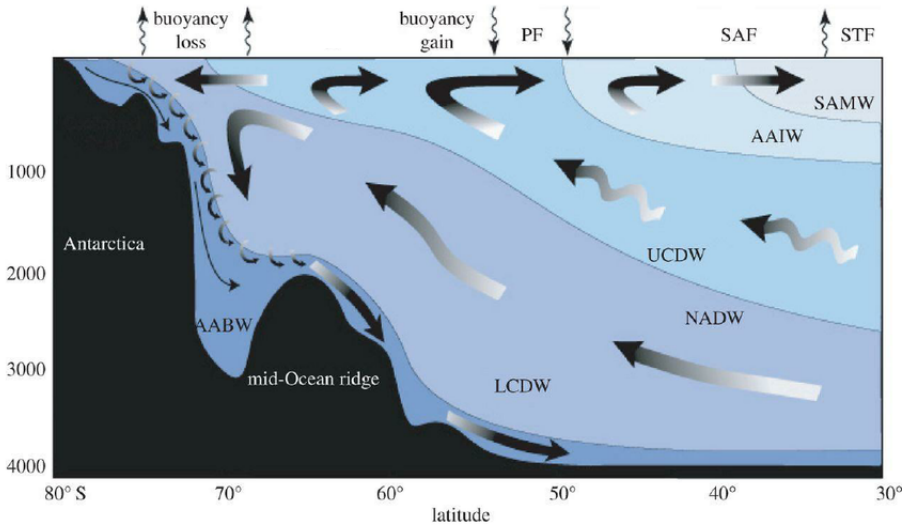

Figure 1.2: *Schematic of the Southern Ocean meridional overturning circulation and its associated fronts and water masses, plus the atmospheric forcing and fluxes (vertical curly arrows). The overturning circulation is indicated by dark arrows, with wavy arrows intended to represent transport by eddies. Small dark arrows show the diapycanal mixing. The colored surfaces represent layers of constant density. Acronyms: Subantarctic Mode Water (SAMW), Antarctic Intermediate Water (AAIW), Upper Circumpolar Deep Water (UCDW), North Atlantic Deep Water (NADW), Lower Circumpolar Deep Water (LCDW), Antarctic Bottom Water (AABW), Subtrpoical Front (STF), Subantarctic Front (SAF), and Polar Frant (PF). Figure from Gent (2016) based on Figure 8 of Speer et al. (2000).*

establish a northward Ekman transport driving cold water masses towards the Equator. This transport is balanced by an Ekman pumping, upwelling water into the surface layer, which tend to tilt isopycnals and thus favour baroclinic instability. The pumping is maximum at the Antarctic Divergence near to 60°S. The potential energy introduced by the steepening of isopycnal slopes is released as Eddy Kinetic Energy (EKE) and generate mesoscale eddies. By dissipating the potential energy, the eddies contribute to

flatten isopycnals, counterbalancing the steepening of density surfaces induced by the wind (Meredith and Hogg, 2006; Marshall and Speer, 2012). The sum of the eddy-induced and wind-driven circulation is called the residual-mean circulation. South of 60°S, closer to Antarctica, easterly winds blow and produce Ekman transport toward the continent. At the boundary, a negative Ekman pumping is induced, downwelling surface waters into the ocean interior. This circulation connecting the interior ocean to the sea surface via upwelling and downwelling constitutes the Southern Ocean overturning circulation and is defined as a double-celled overturning circulation. The North Atlantic Deep Water (NADW) flows southwards across the Atlantic Ocean. When it reaches the Southern Ocean, some of the NADW is carried at lower latitudes, where if forms the Lower Circumpolar Deep Water (LCDW), a high-salinity layer, and upwells close to Antarctica. Due to heat loss and brine rejected during sea ice formation, this water mass is converted into the very dense Antarctic Bottom Water (AABW). Then, it sinks and moves northwards out of the Southern Ocean. This process forms the lower cell of the Southern Ocean overturning circulation. This dense water formation mainly takes place in the Ross and Weddell Seas (Orsi et al., 1993 for Weddell gyre).

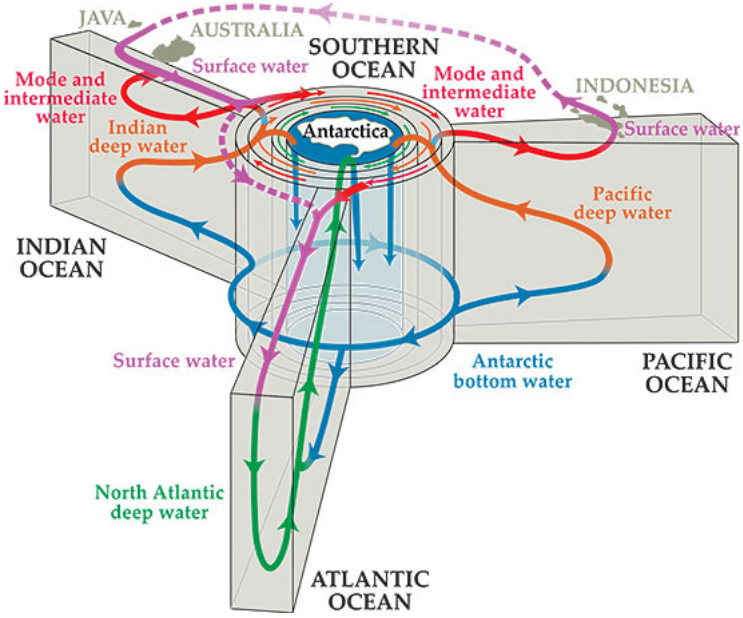

Figure 1.3: *Schematic of the Global Overturning Circulation from a Southern Ocean perspective. Figure from Morrison et al. (2015) adapted from Talley et al. (2011).*

Another type of deep water upwells in the Southern Ocean and forms the upper cell of the overturning circulation which is largely driven by Ekman pumping. The water mass originates from the Pacific and Indian Oceans and is called Upper Circumpolar Deep Water (UCDW). Less dense than NADW, it is characterised by low oxygen concentration, reflecting its long isolation from the atmosphere. UCDW is driven polewards above LCDW and subducts within the ACC belt, where it is freshened and warmed at the surface, transformed to less dense Antarctic Intermediate Water (AAIW) and subantarctic

Mode Water (SAMW) and spreads northwards with the Ekman transport (Figure 1.2). The meridional circulation in the Southern Ocean is connected with the meridional circulation in the Atlantic, Indian and Pacific basins, hence is a fundamental actor of the global meridional overturning circulation (Figure 1.3). The latter ensures stability of the current climate, as it redistributes heat from the equator to high latitudes, and consequently the Southern Ocean plays a key role in climate. More precisely, in the Southern Ocean, Ekman pumping that induces upwelling of the deep branch of the Meridional Overturning Circulation (MOC) to the upper ocean, where it connects with the surface branch, has been identified as one of the fundamental drivers of the MOC (Kuhlbrodt et al., 2007; Marshall and Speer, 2012). Formation of AABW in the Southern Ocean is also a driver of the MOC, precisely the deep cell that flows northwards along the ocean floor in all basins and upwells until mid-depth below NADW. Therefore the Southern Ocean should not be considered only as a passive conduit for the global ocean circulation. Such processes in the Southern Ocean are likely to have repercussions on a much larger scale and beyond the ocean surface, because the Southern Ocean is a key actor of the global ocean hence climate.

1.2.3 Importance of the mesoscale activity in the Southern Ocean

In the Southern Ocean, mesoscale features play a crucial role in meridional exchanges. They contribute to the dynamical and thermodynamical balances of the Southern Ocean by transporting heat (de Szoeke and Levine, 1981; Thompson, 1993; Jayne and Marotzke, 2002; Volkov et al., 2008) and salt (Keffer and Holloway, 1988; Lee et al., 2007) across its frontal zones. Indeed, it has been shown that the mean geostrophic flow carries little heat (de Szoeke and Levine, 1981; Sun, 2002). For instance, at the Drake Passage, to balance the heat lost to the atmosphere at high latitudes and the heat transported equatorwards by Ekman transport, eddies must carry heat polewards (Nowlin et al., 1985). These mesoscale features also carry vertical and horizontal momentum imparted to the Southern Ocean by westerlies, from the surface to the deep layers. Moreover, these mesoscale features also have a significant impact on primary productivity either by pumping nutrients towards the surface, which support the biological activity (McGillicuddy et al., 2007; Lévy et al., 2010) or by spatially redistributing the plankton and nutrients (Gorgues et al., 2005; José et al., 2014). It has been clearly highlighted that eddy formation is not geographically uniform along the length of the ACC but occurs at specific regions correlating to prominent bathymetry (Lutjeharms and Baker, 1980; Gille, 2003; Morrow et al., 2004). In Figure 1.4, the mean Eddy Kinetic Energy (EKE) distribution in the Southern Ocean is shown, with EKE maxima corresponding to the western boundary currents location (the Agulhas current, the Malvinas current, the East Australian current) and to some "hotspots". Regions of high mesoscale variability in the Southern Ocean correlate closely

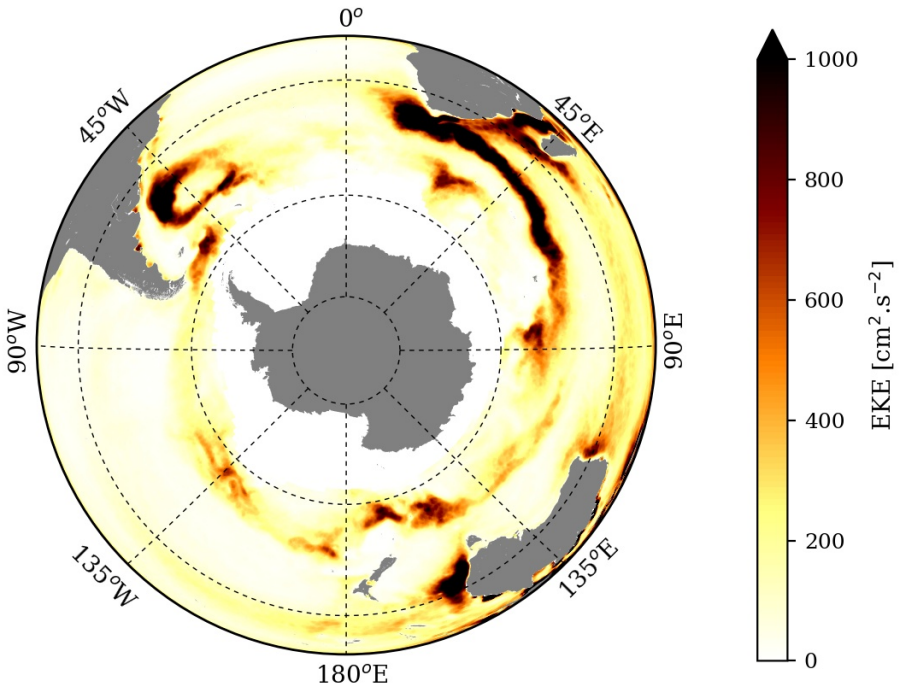

Figure 1.4: *Map highlighting the mean distribution of EKE within the Southern Ocean (Aviso from 1993 to 2017). The warm colours highlight the western boundary currents and where the ACC interacts with prominent bathymetry such as the South West Indian Ridge.*

with areas where the core of the ACC interacts with prominent bottom topography such as the Drake Passage (Joyce et al., 1981), the Crozet and Kerguelen Plateaux, south of Australia (Phillips et al., 2000) and South of Africa at the South-West Indian Ridge (SWIR).

1.2.4 Characterisation of the fronts

The STF is strongly surface intensified while fronts within the ACC are more barotropic and are therefore more steer by the topography (Graham et al., 2012). Three typical frontal regimes are known to exist in the Southern Ocean and have been defined as merging, shoaling, and lee meandering, depending on their position relative to the bathymetry (Sallée et al., 2008). Topography influences the pathway of the fronts as seen in previous studies (Chelton et al., 1990; Gille, 1994; Moore et al., 1999; Sokolov and Rintoul, 2009a; Dong et al., 2006), but also influences the mean intensity of the jet associated with the fronts. In areas where topography is not prominent, fronts are especially subject to large meandering due to mesoscale activity and atmospheric forcing (Sallée et al., 2008). The strong bottom geostrophic flow associated with fronts over topographic features generates lee waves. These internal waves, when they break, produce turbulent mixing and dissipate a significant fraction of the Southern Ocean eddy field energy (Garabato et al., 2004; Nikurashin et al., 2010; Nikurashin et al., 2012). The radiation and breaking of lee

waves are important processes for closing the abyssal overturning circulation (Nikurashin and Ferrari, 2013; Melet et al., 2014).

Frontal systems are essential features of the ACC. They have a direct influence on both the physical and biological processes (Graham, 2014), that is why it is crucial to have a good knowledge of their position in the Southern Ocean. But defining ocean fronts is not a trivial matter (Sokolov and Rintoul, 2007; Chapman, 2014). Orsi et al. (1995) and Belkin and Gordon (1996) derived fronts from hydrographic sections, defining ACC fronts as water mass boundaries. In their study (Orsi et al., 1995 and Belkin and Gordon, 1996) related fronts to strong gradients in water mass properties such as temperature or salinity. From historical data, they developed a map showing the distribution of the three primary continuous circumpolar fronts we mentioned previously: the SAF, the PF and the SACCF. This view of the fronts of the ACC has become the "traditional" view (blue lines on Figure 1.5). However, the introduction of satellite observations and advances in numerical modelling provided new sets of high resolution data and revealed a more complex, multi-filamented frontal structure of the ACC than once though (Gille, 1994; Hughes and Ash, 2001; Sokolov and Rintoul, 2007; Sallée et al., 2008; Sokolov and Rintoul, 2009a). Exploiting these data, several studies have developed criteria from SSH or SST gradients to determine the jets locations (Hughes and Ash, 2001; Sallée et al., 2008; Sokolov and Rintoul, 2009a; Swart et al., 2010). In Figure 1.5, we show different views of

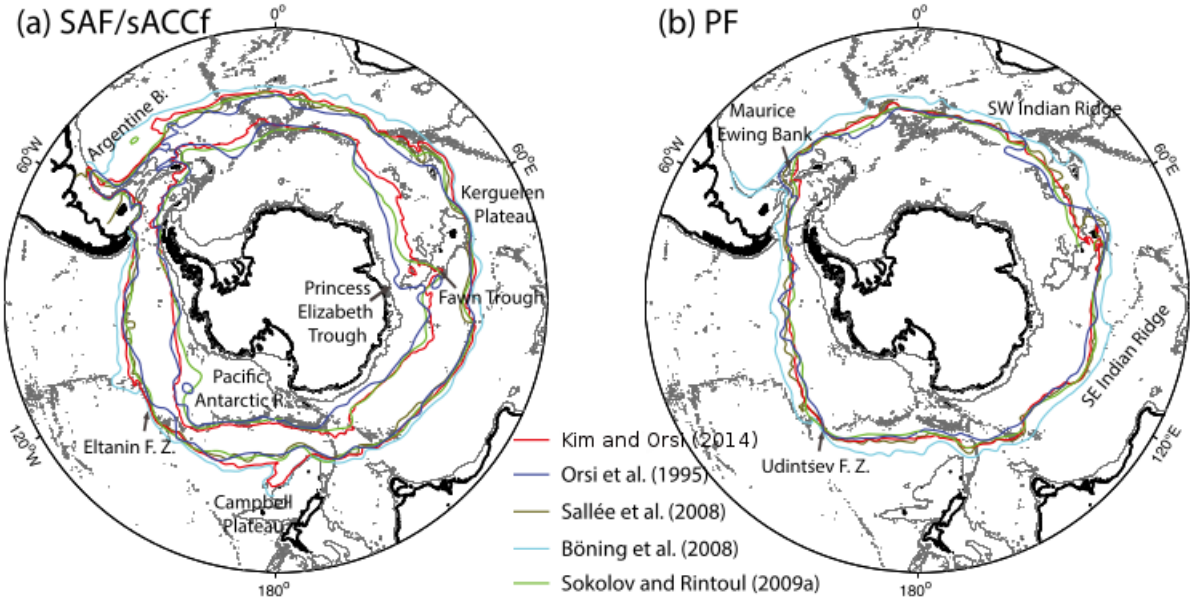

Figure 1.5: *The climatological distribution of (a) SAF and sACCf and of (b) PF derived from Kim and Orsi, 2014 (red), Orsi et al., 1995 (blue), Sokolov and Rintoul, 2009a (green), Böning et al., 2008 (cyan) and Sallée et al., 2008 (olive). The 2500 m isobath (thin gray contour) is included for reference (Source: figure from Kim and Orsi, 2014).*

frontal positions. The positions present discrepancies according to the criterion they are based on, especially at locations where bottom topography is prominent. For instance, at 50°E, the SWIR and the Del Caño Rise forces the SAF to flow northwards before turning

back to the east (Pollard et al., 2007). This particular feature is clearly displayed by Kim and Orsi (2014), Sokolov and Rintoul (2009a) and Sallée et al. (2008), but is missing in Orsi et al. (1995) and Böning et al. (2008) frontal representations. Another example is the northeastward deflection of the SAF, south of the Campbell Plateau at 180°E. Previous studies brought out this northward turn of the SAF that only Kim and Orsi (2014) and Böning et al. (2008) manage to represent. Concerning the PF, it is worth noting that Orsi et al. (1995) is the only one to show a PF reversing at 30°E. In Figure 1.5, the complexity of determining frontal systems locations is well highlighted. Recently, jets and fronts have been a subject of debate and Graham and De Boer (2013) and Chapman (2014) highlighted that "front" and "jet" are two different features and are often used interchangeably in the literature: a "front" is a water mass boundary whereas a "jet" is a strong current. However, even though it is not always the case, fronts and jets are found to coincide quite often (Orsi et al., 1995; Sokolov and Rintoul, 2007, Belkin and Gordon, 1996; Graham et al., 2012). We have focused on the fronts in the Southern Ocean in this section because they constitute important features of the region of the Prince Edward Islands. We will see further on that theses fronts, especially the SAF, play an important role in the dynamics of the region.

1.2.5 Important changes in the Southern Ocean

Over the past decades, the Southern Ocean has experienced substantial changes in properties of its water masses. Recently, observations and reanalysis have showed a shift of the SAM index toward an increasingly positive phase (Marshall, 2003, Figure 1.6), resulting in a strengthening (Thompson and Solomon, 2002) and a contraction of the westerly wind belt towards the Antarctic continent (Fyfe and Saenko, 2006; Swart and Fyfe, 2012). This trend is likely the result of anthropogenic activities (Fyfe et al., 1999; Thompson and Solomon, 2002). In agreement, Gille (2002) has demonstrated by using float observations and shipboard measurements, a warming of the Southern Ocean between 700 and 1100 m since the 1950's. This observed warming, concentrated in the ACC, appears to be consistent with a poleward shift of the ACC by 1° latitude, due to an enhancement of westerly winds in the Southern Ocean (Gille, 2008; Morrow et al., 2008; Sprintall, 2008). However, this migration of the ACC fronts and their link to the SAM are very discussed. Recent studies have shown no coherent trend in the meridional position of the ACC fronts at global scale (Graham et al., 2012; Gille, 2014; Shao et al., 2015; Chapman, 2017). Other studies have highlighted trends in frontal position but only in particular locations where the ACC is weakly control by the topography like Abyssal plains, southeast Indian and Pacific basins (Sallée et al., 2008; Kim and Orsi, 2014). Sallée et al. (2008) and Kim and Orsi (2014) also found significant correlation between the SAM and the position of the ACC fronts but only in the southeast Indian and Pacific basins. These results highlight

that the long-term variability of the fronts in the ACC is not very clear.
Besides warming, Böning et al. (2008) showed, by comparing Argo float data to historical oceanographic data that the Southern Ocean has freshened due to an increase of precipitation over evaporation (Helm et al., 2010; Durack et al., 2010) and also an increase in sea-ice melting (Jacobs et al., 2002, 2010). Haumann et al. (2016) suggested that a stronger northward sea-ice transport could also contribute to salinity change in the Southern Ocean. Observations and models suggest that the time-mean ACC transport is relatively insensitive to decadal changes in wind stress, a tendency commonly referred to as "eddy saturation" (Straub and Straub, 1993; Hogg et al., 2008). Although westerlies have strengthened, Böning et al. (2008) has shown that the isopycnal tilt of the ACC has not changed over the past 50 years and thus the MOC remained unchanged. The steepening of isopycnal slopes induced by excess energy imparted by the wind, is compensated by eddy activity that flatten isopycnals (Hallberg et al., 2006; Böning et al., 2008; Farneti et al., 2010; Abernathey et al., 2011; Meredith et al., 2011). This independance of the MOC to changes in wind stress is termed "eddy compensation". Meredith and Hogg (2006) point out a delay between wind forcing and the eddy response of about 2-3 years. To explain this lag, they suggest that the excess wind energy is initially stored as potential energy and then slowly transfer to EKE. However, Southern Ocean responses to variations in winds and the time scales at which they occur remain controversial. Albeit

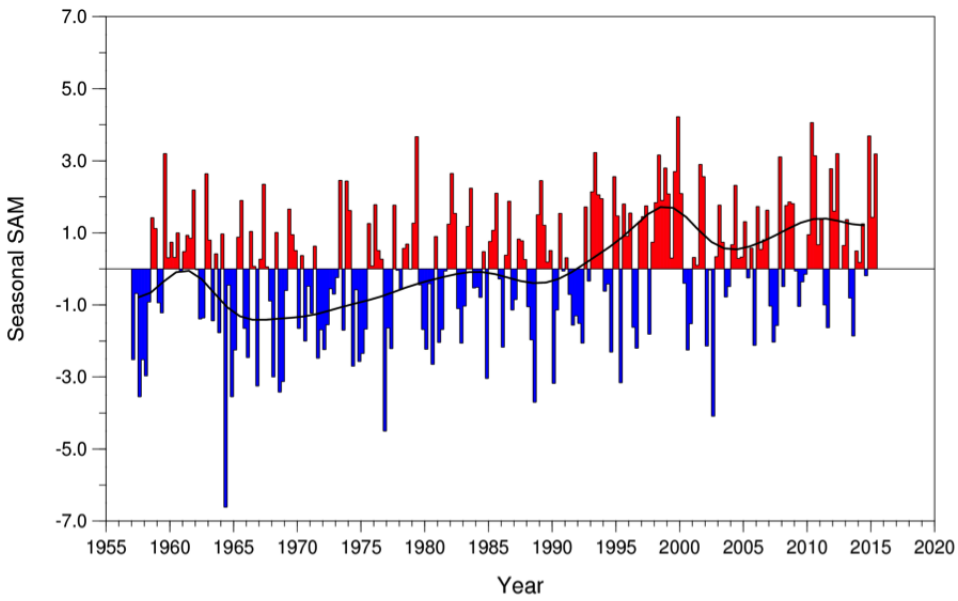

Figure 1.6: *Seasonal values of the observation-based SAM index. The red colour and the blue colour represent the positive values and the negative values of SAM index respectively. The smooth black curve shows decadal variations. This figure is updated from Figure 3.32 in Trenberth et al. (2007) by Marshall (2016).*

ACC transport seems insensitive to changing winds, Meredith et al. (2011) and Jones et al. (2011) suggest that isopycnal slopes could significantly increase but at centennial time scales.

Besides, Sallée et al. (2010) suggested that changes in winds associated to SAM could drive variations in the Southern Ocean mixed-layer depth with consequences for biological productivity and significant implications for physical processes.

1.3 Prince Edward Islands

In the Southern Ocean, between 46°S and 60°S, subantarctic islands (Prince Edward Islands, Crozet, Kerguelen, Campbell...) are found lying between warmer subtropical and cooler Antarctic waters. They experience one of the windiest and humidest climate on Earth. Very remote, these terrestrial and marine ecosystems of these inhospitable regions are relatively simple and extremely sensitive to perturbations. They provide ideal laboratories for studying ecosystems response to climate change in the Southern Ocean (Smith, 2002; Ansorge et al., 2014b). Although the PEIs are found in a low productivity region (Laubscher et al., 1993), the subantarctic islands seasonally support large numbers of land-based predators, including seals, flying birds and penguins (Williams et al., 1979; Condy, 1981; Ryan and Bester, 2008) and biomass-rich inter-island benthic community (Branch et al., 1993). The physical-biological driving mechanisms that supply the necessary food to sustain to the islands ecosystem are referred to as "life support system" of the PEIs(McQuaid and Froneman, 2008). The position of the SAF is one of the key factors.

1.3.1 Historical Background

The islands were first discovered on March, 4th 1663, by Captain Baren Barentzoon Ham, sailing to Batavia (present-day Jakarta), capital of the Dutch East Indies. No landing was made at that time. The more northerly island was called Dena and the southerly island Maerseveen, after Captain's ship. A hundred years later, the island was approached by the French explorer, Marc-Joseph Marion du Fresne on 13 January 1772. He named them *Ile de l'espérance* (Marion Island) and *Ile de la Caverne* (Prince Edward Island). Again, nobody put ashore on the islands. The next visit was done by Captain James Cook in December 1776. Like du Fresne and Barentzoon, he just sailed between the islands without landing. He renamed the island group the Prince Edward Islands (PEIs hereafter) after Prince Edward, the fourth son of King George III, king of the United Kingdom.

Figure 1.7: *The sealers' hut at Mixed Pickle Cove, Marion Island (photo by Sergeant William John Deysel, 1954).*

Figure 1.8: *Current scientific base on Marion Island (photo from* `www.sanap.ac.za/stations/marion-base`*).*

The name Marion Island was originally used by Cook to refer to the modern-day Crozet Islands as Marion and Crozet islands. Later on, in the middle of the 19th century, the sealers used the name Marion Island for the largest island of the archipelago and since then, it has become its official name. The first recorded landing was in either December 1803 or January 1804 by Captain Henry Fanning who disembarked a shore-sealing crew. Even if the first vessel to land at PEIs remains unknown, it is very likely that it has been made by sealers (Figure 1.7 shows evidence of a past sealing activity on Marion Island). South Africa annexed the archipelago in 1948 and established a meteorological station on the north-east coast of Marion Island (see Cooper and Headland (1991) for all the historical references). Since then, a new scientific base was built and was inaugurated in 2011 (Figure 1.8). In 1993, the South African government declared the PEIs a Special Nature Reserve. In 2013, its status was upgraded to Marine Protected Area, granted more environmental protection.

Since the end of the 1980s, many surveys, supported by the South African National Antarctic Programme, have been undertaken (MOES: *Marion Offshore Ecosytem Study*, MIOS: *Marion Island Offshore Variability Study* and DEIMEC: *the Dynamics of Eddies Impact on Marion's ECosystem*) but they remained sparse. In 2013, an annual monitoring of PEIs's marine environment was initiated and, one year later, two long-term moorings were deployed between the two islands, continually recording water column temperature and current (Ansorge et al., 2014b; von der Meden et al., 2017).

1.3.2 Island Setting

The PEIs, the most southerly part of South Africa's official territory, are located in the Indian sector of the Southern Ocean at approximately 46°50'S and 37°50'E. The islands rise steeply from a region of complex bottom topography and lie east of the South-West Indian Ridge and southwest of Del Caño Rise (Figure 1.9). They constitute an isolated

surface from which the nearest landfall is the Crozet archipelago, 950 km to the east whereas South Africa lies 2000 km to the north-west. The islands group of volcanic

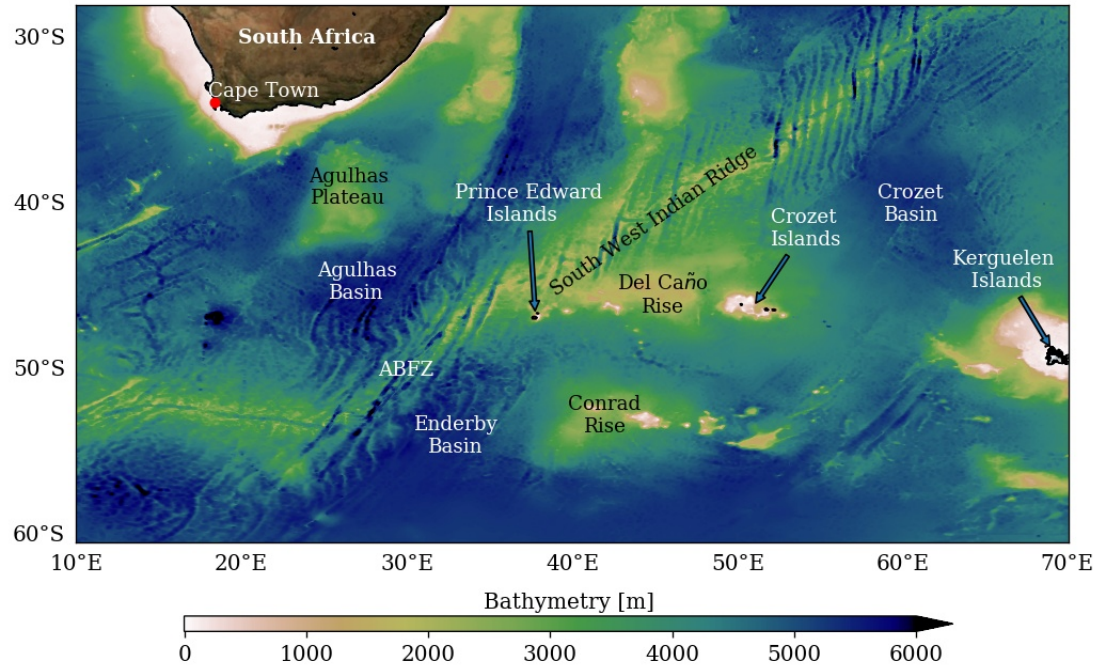

Figure 1.9: *Bathymetry of the Southern Ocean part where the PEIs are found (ETOPO2 bathymetry[3]). The major bathymetric features of the region are indicated. ABFZ stands for the Andrew Bain Fracture Zone.*

origin, less than one million years old (McDougal, 1971), consists of Marion Island and Prince Edward Island, Marion Island being the largest of the two. They are 19 km apart and separated by a shallow saddle which is between 40 and 200 m deep rising of a depth of over 3000 m (Ansorge et al., 1999; Ansorge and Lutjeharms, 2002). In the center of the Island plateau, a deep ($>$ 200 m) and narrow ($>$ 9 km) channel runs southeastwards (Pakhomov et al., 2000).

1.3.3 Circulation around the Islands

The PEIs lie directly in the path of the ACC, within the PFZ. They are sandwiched between the SAF to the north, and the PF to the south (Lutjeharms, 1985). These fronts separate warm subantarctic Surface Water (SASW), commonly found north of the SAF, from cooler Antarctic Surface Water (AASW) found south of the PF. The SAF and PF exhibit high degrees of latitudinal variability in this region (Lutjeharms, 1985; Nagata et al., 1988; Duncombe Rae, 1989) and the latitudinal position of the SAF is a critical component that determines hydrographic and biologic conditions at the islands.
Previous investigations have shown that when the SAF lies far north of the islands, the PFZ is broader and advective forces are weak (Figure 1.10). The flow rate of the ACC is

[3] `https://www.ngdc.noaa.gov`

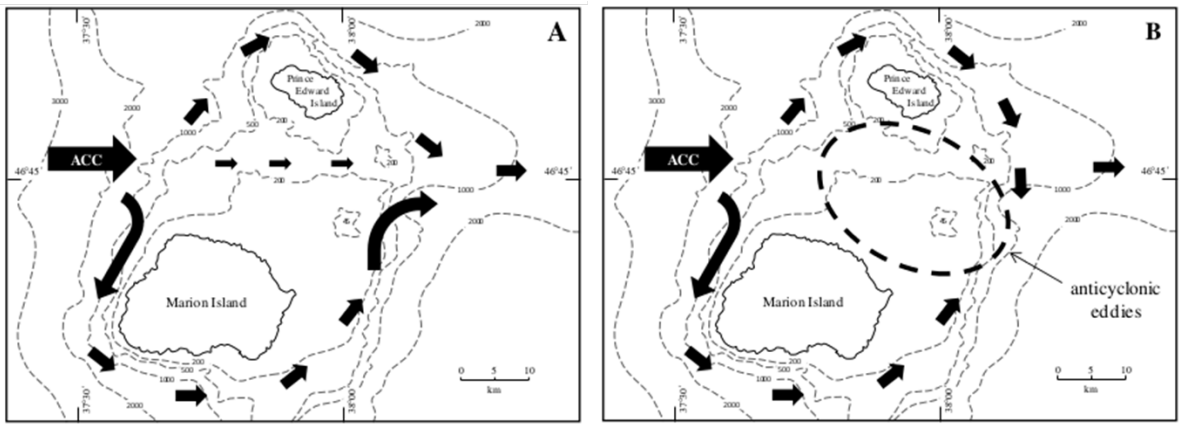

Figure 1.10: *Schematic showing the hydrodynamics around the Prince Edward Islands when (A) the SAF lies in closer proximity to the islands, resulting in a flow-through system and when (B) the SAF lies far to the north of the islands, resulting in the formation of anticyclonic eddies between and within the lee of the islands (Allan, 2011).*

reduced enough to allow the frictional forces between the islands and the flow to result in the formation of trapped anticyclonic eddies (Perissinotto and Duncombe Rae, 1990; Pakhomov et al., 2000; Ansorge and Lutjeharms, 2002). During these periods, signature Antarctic species dominate. In this situation of water retention, nutrient inputs via runoff from the islands lead to a phenomenon called the "island mass effect" which produces blooms between and downstream of the islands (Boden, 1988; Perissinotto and Duncombe Rae, 1990). Perissinotto and Duncombe Rae (1990) pointed out that a minimum of 15 days of water retention is necessary to enable blooms. This situation is favorable to the rich benthic community as well as for some predators which are near-shore feeders, such as rockhopper penguins and imperial cormorants. In contrast, when the SAF meanders southwards and thus in closer proximity to the islands, advection forces prevail and a flow-through system, rich in both subantarctic and subtropical species, is established (Pakhomov et al., 2000). This flow-through system prevents eddies to be trapped in the inter-island region (Ansorge et al., 1999; Perissinotto et al., 2000). While some predators feed close to the islands, others feed elsewhere and tend to feed primarily in the vicinity of the fronts. Thus, the case of the SAF lying close to the islands is favorable to offshore feeding predators (fur seal, grey-headed albatross, northern giant petrel).

The islands are strongly influenced by the position of the SAF but they are also impacted by intense mesoscale features, originated at the South West Indian Ridge (SWIR, Figure 1.11). Several investigations have shown that this prominent topographic feature exerts a large influence on the location and dynamics of the ACC (Moore et al., 1999), resulting in substantial fragmentation of the jets downstream of the ridge (Pollard and Read, 2001) and causing a remarkably enhanced production of EKE. This "hotspot", centered at 50°S-30°E, coinciding with the Andrew Bain Fracture Zone (ABFZ), lies directly upstream of the PEIs. The region immediately downstream of the SWIR has been identified as an eastward eddy corridor (Ansorge and Lutjeharms, 2003; Ansorge and Lutjeharms,

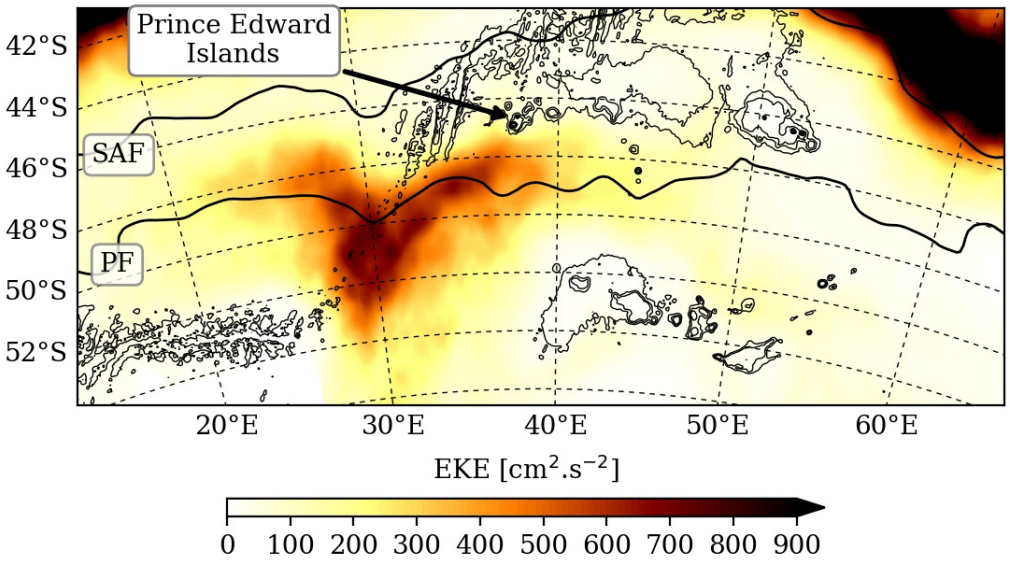

Figure 1.11: *EKE in the vicinity of the PEIs averaged over the 1993-2017 period. EKE is derived from altimetry (Aviso). Bathymetric contours (1000 m, 2000 m, 3000 m) are overlaid in grey (ETOPO2). The two black lines denote the mean position of the SAF and PF. The fronts locations come from Swart et al. (2010).*

2005) extending to the PEIs vicinity, in which cyclonic and anti-cyclonic eddies, acting as vehicles, transport physical and biological characteristics typical of both the subantarctic Zone and Antarctic Zone across the PFZ. Many studies have shown that seals and birds exploit eddies for their foraging (Nel et al., 2001; Simmons et al., 2007; Cotté et al., 2015). The easterly extension of this eddy corridor appears to be restricted to the deep channel separating the Conrad Rise from the Del Caño and Crozet Plateau. Besides the eastward extension, a southward eddy corridor has been identified by Ansorge et al. (2014a). This southward passage acts as a conduit in which warm-core eddies travel southwards. In their paper, Durgadoo et al. (2010) summarized the results of oceanographic observations of eddies impacting PEIs and found that an average of three intense eddies is observed per year. These eddies can extend to depths of more than 1000 m and have a longevity of 7-11 months.

1.3.4 Evidence of Climate Change at Prince Edward Islands

Since the 1950s, Prince Edward Islands have experienced rapid changes in climate. Changes in the intensity and geographic position within the frontal systems of the ACC are likely to coincide with dramatic changes in the distribution of species and total productivity in the Southern Ocean and in particular at the PEIs. The impacts that a southward migration of the ACC would have on the ecosystem of these islands over the next century are complex (Ansorge et al., 2012).

Ansorge et al. (2009) have shown that the SAF has shifted southwards by about 1^o. Furthermore, data from the vicinity of the PEIs indicate that the surface water temperature

has increased by 1.4°C since 1950s (Mélice et al., 2003) and air temperature has increased by 1.21°C (Smith, 2002; le Roux and McGeoch, 2008). In addition to this rise in temperature, a decrease in annual precipitation by 25% since the beginning of the 1970s, changes in wind speed and direction and an increase in sunshine hours have been recorded (Smith, 2002; Rouault et al., 2005). Sumner et al. (2004) has also revealed a conspicuous melting of snow and ice on Marion Island. Furthermore, the southward migration of the SAF, by favouring a through-flow regime, seems to have contributed to a long-term decline in the frequency of phytoplankton blooms in the inter-island region (Pakhomov and Chown, 2003; Allan et al., 2013). Besides, a substantial change in zooplankton populations has been noticed. The occurrence of Antarctic zooplankton species has decreased in the PFZ whereas that of subtropical species has increased, which suggests a more frequent intrusion of warmer subantarctic surface waters into the PFZ (Pakhomov et al., 2001). The decrease in bloom occurrences ("island mass effect") may have strong consequences on higher trophic levels (McQuaid and Froneman, 2008; Allan et al., 2013).
Mirrored to this primary production decline, some changes in top predators populations found seasonally on the islands have been observed. Population sizes of land-based predators foraging offshore (Grey-headed Albatrosses, Northern Giant Petrels, Subantarctic and Antarctic seals...) have increased (Pakhomov and Chown, 2003; Hofmeyr et al., 2006; Ryan et al., 2009). It may be a consequence of a decrease in foraging distance from the PEIs to frontal systems, characterised by enhanced primary productivity. In contrast, predators that feed predominantly inshore, such as gentoo or rockhopper penguins, have decreased, likely as a result of decreased food availability (Ryan and Bester, 2008).
Allan et al. (2013) suggests that the decline of top predators relying on prey inhabiting the inshore system of the islands confirms the vulnerability of marine ecosystems to changes in physical conditions. This highlights that the effect of climate change may be indirect and need to be further explored to determine if this is natural variability or anthropogenic.

1.4 Aims of the PhD

In this general introduction, we pointed out that the Southern Ocean has a complex dynamic and it plays a key role in the regulation of the climate of our planet by being an essential actor of the global MOC. It is highly impacted by the global warming which is particularly pronounced at the subantarctic islands among which are the PEIs. The islands support rich terrestrial and marine ecosystems, and its physical environment is extremely variable and highly sensitive to perturbations in climate change. Lying in a zone where the position of the SAF is very variable and mesoscale activity is intense make the PEIs an ideal laboratory to study how climate change impacts the hydrodynamics in the subantarctic region. Besides these large scale processes, some local processes, like tides and winds, take part in the variability of the islands.

This PhD aims to clarify the impacts of those different processes on the PEIs. To investigate this, we divided the issue in three questions:

- **Offshore processes versus local processes: What are their impacts on the circulation observed at the PEIs?**
  As a first step, it seems important to differentiate and quantify the impact of the position of the SAF and eddies from tide and wind impact. This study is based on analysis of available data (moorings, CTD, altimetry) in the region of interest.

- **What are the processes at play in eddies formation in this region?**
  Eddies are important features for the island sustainability and they have been extensively studied. A detailed investigation into the role the SWIR plays on the formation of mesoscale eddies is carried out in order to characterize the instabilities responsible of their generation.

- **How does the southward shift of the SAF affect eddies generation?**
  The consequences of a frontal shift in the ACC, at large scale, has been largely documented in literature. Here we focus on a small region, namely from the SWIR to the PEIs, and investigate the potential impact of the SAF shift on the hydrodynamics of this area.

Chapter 2 presents the methodology we followed to address these questions. First, the observational datasets are described as well as the numerical model and configurations that were used during the PhD. Then, the method used to detect front from altimetry in the PEIs region is detailed.
Chapter 3 assesses the data available in the area and highlights the insufficiency of long term data to fully understand the oceanic variability around the islands, justifying a numerical modelling strategy.
The question about processes at play in eddies formation at the South West Indian Ridge is addressed in Chapter 4. We also present a sensitivity test of eddies to bathymetry.
Chapter 5 deals with the southward shift of the SAF and set out the potential impact of such a frontal migration on eddies production at the SWIR.
The last part of this PhD dissertation summarizes the results and proposes general perspectives of this study.

2 Material & Methods

Contents

2.1 Data description

2.1.1 Satellite Altimetry data

The Southern Ocean is poorly sampled due to its remoteness. Recent advances in remote sensing have provided new opportunities to study the circulation in the ACC, such as measurements of sea surface height. The altimeter products are produced by Ssalto/Duacs and distributed by Aviso, with support from CNES[1]. The data used in this thesis covers the period from January 1993 to May 2017. In this study we use the maps of Absolute Dynamic Topography (MADT) of Duacs 2014 version, which combine the Sea Level Anomalies (SLA) with the CNES-CLS13 Mean Dynamic Topography (Rio et al., 2014). A mapping procedure (Ducet et al., 2000) is used to generate MADT, merging measurements from two altimeter missions. The global gridded data is computed on a Cartesian $\frac{1}{4}^\circ \times \frac{1}{4}^\circ$ spatial resolution every day at a delayed-time. Aviso provides also the zonal and the meridians components of surface geostrophic velocities, derived from Absolute Dynamic Topography.
Sea surface height data are used to detect the position of the fronts in the region of the PEIs (see section 2.4) and to study the mesoscale activity.

2.1.2 Mooring Data

A pair of subsurface long-term moorings were deployed on 7 April 2014, across the inter-island plateau, during the SA Agulhas II's annual relief voyage to Marion Island. They are directed at measuring, through temperature and velocity profiles, the position of the SAF in order to separate the impacts of short-term variability from the long-term southward migration on the islands (Ansorge et al., 2014b).
Mooring 1 is positioned on the inter-island plateau (46°46.5' S - 37°54' E) and Mooring 2 is closer to Prince Edward Island (46°42.75' S - 37°54' E). Depth of the mooring sites is 169 m for Mooring 1 which sits on the plateau and 318 m for Mooring 2 which is on the slope. Figure 2.1 illustrates the location of the moorings between the islands overlaid to the SRTM30 (30 seconds resolution) bathymetry. Each mooring consists of an upward facing 150 kHz Acoustic Doppler Current Profiler (ADCP) installed in a 36" Floating Technologies buoy. Data were configured to record hourly temperature and velocity readings. The sub-surface floats provide temperature readings 5 m above the sea floor while the ADCP records current (intensity and direction) of the water column above the mooring system (von der Meden et al., 2017). The ADCP records current velocities by sampling the water column above the moorings into 30 bins of 8 m each. Mooring 1 has 17 workable bins which allow for a span of velocities between 20-150 m whereas

[1] http://www.aviso.altimetry.fr/duacs/
[2] http://www.topex.ucsd.edu/WWW_html/srtm30_plus_html

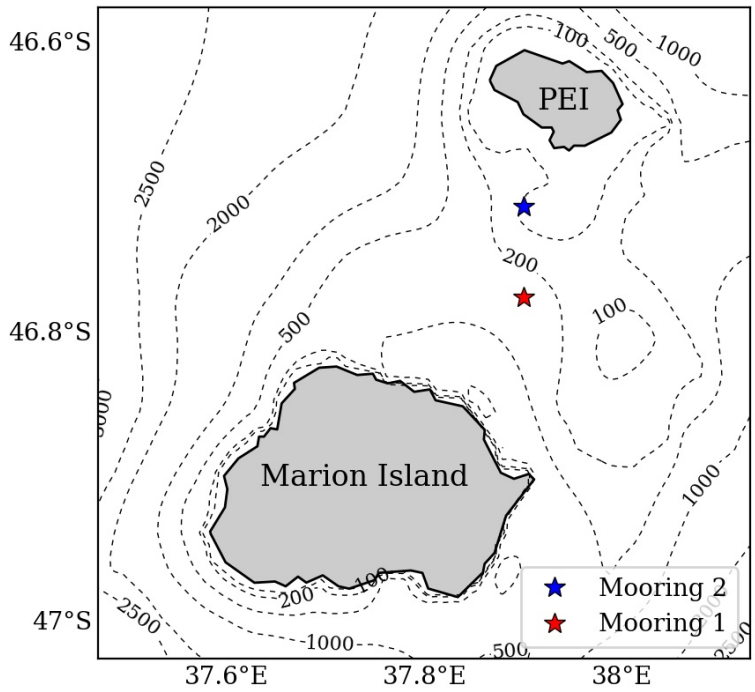

Figure 2.1: *Locations of the moorings (stars) overlaid to SRTM30[2] bathymetry (1 km resolution). Isobars show depth in meters. The islands are separated by a shallow saddle with a deep and narrow channel in the center running southeastwards. Mooring 1 sits on the plateau at 169 m deep and Mooring 2 is located on the slope of the channel at 318 m.*

Mooring 2, with 28 workable bins, give velocities from 250 m extending to 30 m.
To date the moorings have recorded current (intensity and direction) and temperature every hour, over two years (from April 2014 to May 2016). The temperature was measured at the mooring depth, respectively at 169 m and 318 m, while the ADCPs allowed to get water current velocities over a depth range, above the mooring system. Mooring 1 provided a workable dataset from 150 m extending to 20 m and Mooring 2 from 250 m to 30 m.

2.1.3 CTD Data

Initiated in 2013, a long-term annual monitoring is performed in the vicinity of the islands in order to measure the impact of the long-term southward migration of the ACC on the PEIs' environment (Ansorge et al., 2014b), during the Marion Relief Voyages on board of the SA Agulhas II. It consists of two CTD transects comprising 8 stations running north-south upstream of the islands and 6 stations running east-west downstream of and between the two islands (Figure 2.2). CTD stations are deployed for analysis of various physical, chemical and biological water column parameters including temperature, salinity and oxygen (we only use temperature and salinity in this study). The transects are available for years 2013-2015.

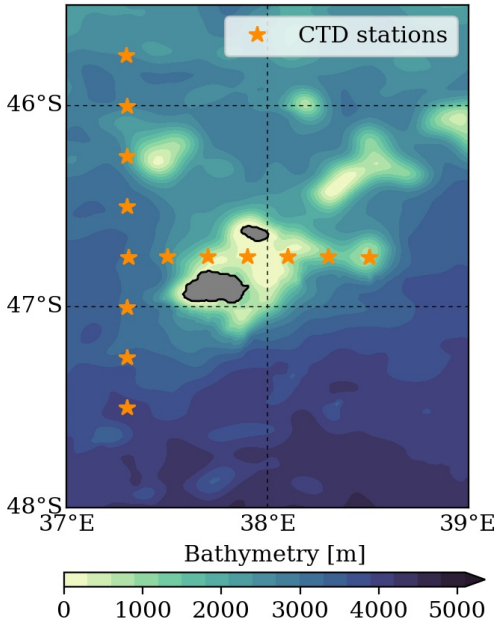

Figure 2.2: *Map showing positions of the 14 stations of the PEIs Monitoring Transects: 8 stations for the upstream transect (north-south) and 6 stations downstream and between the islands (east-west).*

2.1.4 Wind data

The South African Weather Service[3] provided us hourly wind in-situ data, recorded at Marion Island since 1950. We daily-averaged these data before using them.

2.2 The Coastal and Regional Ocean COmmunity model

The Coastal and Regional Ocean COmmunity model (CROCO) is a three-dimensional, free-surface, split-explicit, ocean model (Shchepetkin and McWilliams, 2005; Penven et al., 2006; Debreu et al., 2012). It solves the primitive equations and uses terrain-following curvilinear coordinates. The primary equations are derived from the Navier-Stokes equations by making the approximations of Boussinesq, of hydrostatic vertical momentum balance and of incompressibility of the fluid. In Boussinesq approximation, seawater density variations are small enough to be neglected in the Navier-Stokes equations, except in their contribution to the buoyancy force. The hydrostatic approximation assumes that ocean depth is smaller compared to the horizontal basin-scale and thus that the vertical pressure gradient is balanced by gravity. Incompressibility is based on the assumption that the volume of fluid does not vary with pressure.

[3] http://www.weathersa.co.za/

2.2.1 Equations of Motion

The primitive equations of motion, under Boussineq and hydrostatic approximations, for an incompressible ocean in Cartesian coordinates can be written:

- Horizontal momentum equations

$$\frac{\partial u}{\partial t} + \vec{v}.\nabla u - fv = -\frac{1}{\rho_0}\frac{\partial p}{\partial x} + \nabla_h(\kappa_{Mh}.\nabla_h u) + \frac{\partial}{\partial z}(\kappa_{Mv}\frac{\partial u}{\partial z})$$

$$\frac{\partial v}{\partial t} + \vec{v}.\nabla v + fu = -\frac{1}{\rho_0}\frac{\partial p}{\partial y} + \nabla_h(\kappa_{Mh}.\nabla_h v) + \frac{\partial}{\partial z}(\kappa_{Mv}\frac{\partial v}{\partial z})$$

- Hydrostatic balance

$$\frac{\partial p}{\partial z} = -\rho g$$

- Continuity equation

$$\frac{\partial u}{\partial x} + \frac{\partial v}{\partial y} + \frac{\partial w}{\partial z} = 0$$

- Tracers advection-diffusion equations

$$\frac{\partial T}{\partial t} + \vec{v}.\nabla T = \nabla_h(\kappa_{Th}.\nabla_h T) + \frac{\partial}{\partial z}(\kappa_{Tv}\frac{\partial T}{\partial z})$$

$$\frac{\partial S}{\partial t} + \vec{v}.\nabla S = \nabla_h(\kappa_{Sh}.\nabla_h S) + \frac{\partial}{\partial z}(\kappa_{Sv}\frac{\partial S}{\partial z})$$

- Equation of state for sea water

$$\rho = \rho(S, T, p)$$

where u, v and w are velocity components in the x, y and z directions respectively, f is the Coriolis parameter, g is the acceleration of gravity, p is the dynamic pressure, ρ is the density, ρ_0 is the reference density for seawater, T is the potential temperature, S is the salinity, κ_{Mv}, κ_{Sv} and κ_{Mv} are the vertical turbulent mixing coefficients, κ_{Mh}, κ_{Th} and κ_{Sh} are horizontal turbulent mixing coefficients.

2.2.2 Vertical boundary conditions

- Surface boundary condition (z = ζ)

$$\frac{\partial \zeta}{\partial t} + u\frac{\partial \zeta}{\partial x} + v\frac{\partial \zeta}{\partial y} = w$$

$$\kappa_{Mv}\frac{\partial u}{\partial z} = \frac{\tau_x}{\rho_0}$$

$$\kappa_{Mv}\frac{\partial v}{\partial z} = \frac{\tau_y}{\rho_0}$$

$$\kappa_{Tv}\frac{\partial T}{\partial z} = \frac{Q}{\rho_0 C_p}$$

$$\kappa_{Sv}\frac{\partial S}{\partial z} = \frac{S(E-P)}{\rho_0}$$

- Bottom boundary condition (z = -H)

$$-u\frac{\partial H}{\partial x} - v\frac{\partial H}{\partial y} = w$$

$$\kappa_{Mv}\frac{\partial u}{\partial z} = \frac{-C_d|\vec{u}|u}{\rho_0}$$

$$\kappa_{Mv}\frac{\partial v}{\partial z} = \frac{-C_d|\vec{u}|v}{\rho_0}$$

$$\kappa_{Tv}\frac{\partial T}{\partial z} = 0$$

$$\kappa_{Sv}\frac{\partial S}{\partial z} = 0$$

Where ζ is the free surface elevation, τ_x and τ_y are the surface wind stress components, Q is the surface heat flux, E is the evaporation, P is the precipitation and C_d is the bottom drag coefficient.

2.2.3 Spatial discretization

The equations of the model are horizontally discretized on the Arakawa C-grid which is suited to model resolutions that are finer than the first Rossby radius of deformation (Arakawa and Lamb, 1977). The variables are vertically staggered at different levels.

- ζ, H, f, ρ and active/passive tracers (T,S) are located at the center of the cell.
- Horizontal velocity (u and v) are located at the center of cell's lateral faces.
- The vertical velocity (w) and vertical mixing variables are located at the top and bottom of cell's faces.

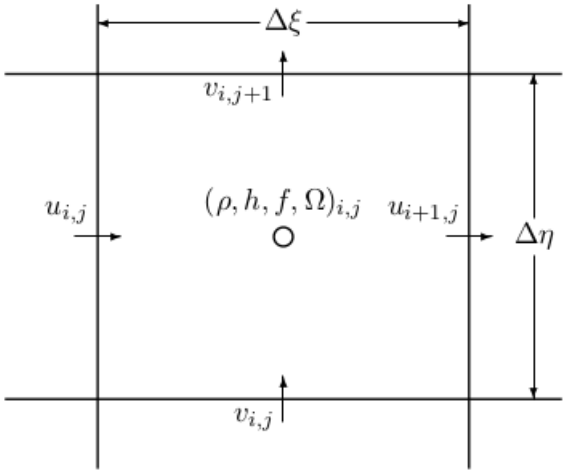

Figure 2.3: *The position of the variables on the Arakawa horizontal C-grid.*

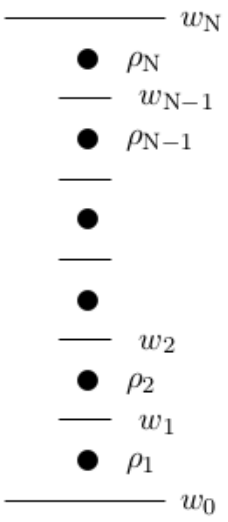

Figure 2.4: *The vertical positions of variables.*

2.2.4 Temporal discretization

For reasons of efficiency, a split-explicit time-stepping scheme is used to separate barotropic (fast) and baroclinic (slow) modes: a 2D surface model is coupled to the 3D model to consider separately the surface gravity waves and the internal waves. A finite number of barotropic time steps, within each baroclinic step, are run in order to develop the free-surface and vertically integrated momentum equations. To avoid aliasing of frequencies resolved by the barotropic steps but unresolved by the baroclinic step, the barotropic fields are averaged over one baroclinic time step before being reinjected (Shchepetkin and McWilliams, 2005). Time discretization follows a third-order accurate predictor (Leap-Frog) and corrector (Adams-Molton) time-stepping algorithm which is very robust and stable (Shchepetkin and McWilliams, 2005).

2.2.5 Advection scheme

CROCO offers various options for advection schemes: second- and forth-order centered differences; and third-order, upstream biased. By default, the advection scheme is third-order upstream biased which allows the generation of steep gradient (Shchepetkin et al., 1998), with a weak dispersion and diffusion.

2.2.6 Turbulent closure scheme

The parametrization of the unresolved vertical subgrid-scale mixing processes is done with a non-local, K-profile (KPP) boundary layer scheme(Large et al., 1994). This scheme uses two distinct parametrizations to solve vertical mixing in the boundary layer and in the ocean interior. The boundary layer depth varies with buoyancy, surface forcing and the velocity profile, and it is determined by comparing a bulk Richardson number (measure

of turbulence: $Ri = N^2/(du/dz)^2$ where N is the Brunt-Väisälä frequency) relative to the surface to a critical value. Below the boundary layer, the vertical mixing depends on the vertical shear, internal wave breaking and double diffusion. At the base of the surface boundary layer, both diffusivity and its gradient are forced to match to the interior values.

2.3 The Prince Edward Islands Configuration

We chose to set up a semi-idealised configuration with a realistic bathymetry but with non-seasonal forcings. The approach is a two-way nesting which allow interaction between the parent and the child. The fine grid (child) is forced by the coarse grid (parent) at the lateral boundaries and then the parent, in turn, is updated by the child model.

2.3.1 The Parent Grid

The parent grid extends from 17°E to 61.25°E and from 55.25°S to 44°S (Figure 2.5). It encompasses the Andrew Bain Fracture zone (ABFZ) and partially the South West Indian Ridge (SWIR), with a maximum depth of 5000 m. The fracture zone is a region of high mesoscale variability where eddies are generated and travel along the SWIR toward the PEIs. Hence, explaining the variability around the islands necessitates to properly resolve the dynamic circulation and mesoscale events that are formed by the ABFZ cross-cutting the SWIR (Ansorge and Lutjeharms, 2003; Ansorge and Lutjeharms, 2005). Between the Del Caño Rise and the Crozet Plateau,the ACC flows northwards and then turns back eastwards north of the plateau (Pollard et al., 2007). As such, we chose to extend the grid downstream of the Crozet Plateau, in order to avoid circulation problems at the boundaries.

The spatial resolution of the grid is $\frac{1}{4}^\circ$. It has 178×72 horizontal ρ-points and 45 σ levels on the vertical. The horizontal resolution ranges from 15.8 km inv the south to 20 km in the north. The vertical levels are refined near the surface, above $h_c = 10$ m, using stretching parameters $\theta_s = 5.5$ (surface) and $\theta_b = 0$ (bottom). The bathymetry used is GEBCO1 (General Bathymetric Chart of the Oceans[4]), 1' horizontal resolution. In order to minimize the error in the pressure gradient leaded by steep gradient in bathymetry, the latter is smoothed to keep the slope parameter $r = \frac{\Delta h}{h}$ inferior at 0.25.

Lateral boundaries and initial conditions

The parent model has all its physical lateral boundaries opened (north, south, east, west). The initial condition and lateral open-boundaries fields are derived from the GLobal Ocean ReanalYsis and Simulation (GLORYS). GLORYS is based on the NEMO Ocean General Circulation Model (OGCM) at $\frac{1}{4}^\circ$ horizontal resolution and 75 vertical levels. Here we used

[4] `http://www.gebco.net`

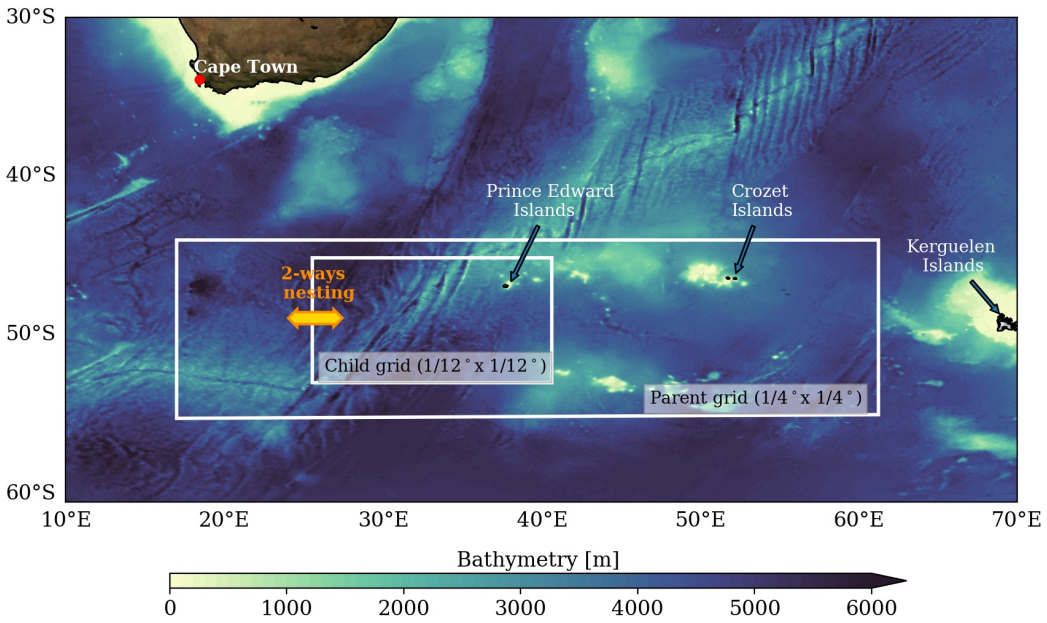

Figure 2.5: *Bathymetry of the Southern Ocean part where the PEIs lie (GEBCO1). White frames are the parent and child configuration domains. The 2-ways nesting arrow indicates that interactions are allowed between the parent grid and the child grid.*

the monthly means of GLORYS2V3 outputs from January 1993 to December 2013. We chose to force the simulation with climatological fields (no seasonal cycle). The parameters of the sponge layers at the open boundaries are assigned internally of the model: it selects the sponge layer extension (10 points with cosine shape function) and enhanced viscosity and diffusivity values near lateral boundaries, according to the horizontal resolution. We impose a nudging to the annual mean climatology.

Surface Forcing

The wind stress chosen to force the configuration is from the Scatterometer Climatology of Ocean Winds (QuikSCOW) data set (Risien et al., 2008), computed on 122 months (September 1999 to October 2009) of QuikSCAT scatterometer data with a horizontal resolution of $\frac{1}{4}^{\circ}$. Atmospheric fluxes (heat and fresh-water fluxes) come from the Comprehensive Ocean Atmosphere Dataset (COADS05, da Silva et al., 1994). This dataset provides monthly climatology fluxes , with a horizontal resolution of $\frac{1}{2}^{\circ}$.

Numerical Parameters

We chose the Von-Karman quadratic bottom stress formulation with a roughness length $z_{ob} = 10^{-3}$ m and a drag coefficient C_D varying from 10^{-4} m.s^{-1} to 10^{-1} m.s^{-1}.

2.3.2 The Child Grid

The Rossby radius of deformation is small in the region (10-13 km, Chelton et al., 1998). As such, resolve the dynamics in the region of the PEIs requires a high resolution configuration. The strategy of having a high resolution grid (child) nested into a coarse resolution grid (parent) is a good compromise, allowing to model the processes at play in the area at a reasonable computational cost. The grid is centered on the SWIR, embedding the ABFZ and the islands. It spans meridionally 25.59°E - 40.67°E and zonally 53.01°S - 45.13°S and has a horizontal resolution of $\frac{1}{12}^{\circ}$, which is one third of the parent resolution. The child's resolution increases from 5.3 km in the south to 6.3 km in the north. The grid has 182×146 ρ-points and the same number of σ levels as in the parent grid. Stretching parameters θ_s and θ_b are also the same as the parent configuration.
The bathymetry of the nested configuration is similar to the parent's one. In the same way than for the coarse grid, the bathymetry is smoothed under the constraint $\frac{\Delta h}{h}$ inferior at 0.25 in order to avoid pressure gradient errors caused by steep slopes.

Lateral boundaries and initial conditions

The boundaries conditions are supplied by the parent domain. The initial state is derived from GLORYS2V3.

Surface Forcing

Surface forcing uses the same data COADS05 and QuikSCAT as in the parent configuration.

2.4 Following the ACC major fronts from altimetry

Several options exist to detect the major fronts of the ACC. They can be derived from hydrological data (Orsi et al., 1993; Belkin and Gordon, 1996) or by using satellite data such as sea surface temperature or Sea Surface Height (SSH) (Hughes and Ash, 2001; Sallée et al., 2008; Sokolov and Rintoul, 2009b; Swart et al., 2010), which can be confusing and also innacurate given the complexity of the frontal bands associated with the ACC. Sokolov and Rintoul (2009b) provide SSH values associated with each branch of the ACC fronts, using 15 years (1992-2007) of weekly SSH gradients fields (Le Traon et al., 1998). The approach used is described in details by Sokolov and Rintoul (2007). The idea is to associate fronts to SSH contours coinciding with zone of large SSH gradients. Sokolov and Rintoul (2009c) subdivided the circumpolar belt into 12 sectors and calculated the SSH gradient in each sector. The authors provide a mean SSH value associated with each frontal branch of the circumpolar current.

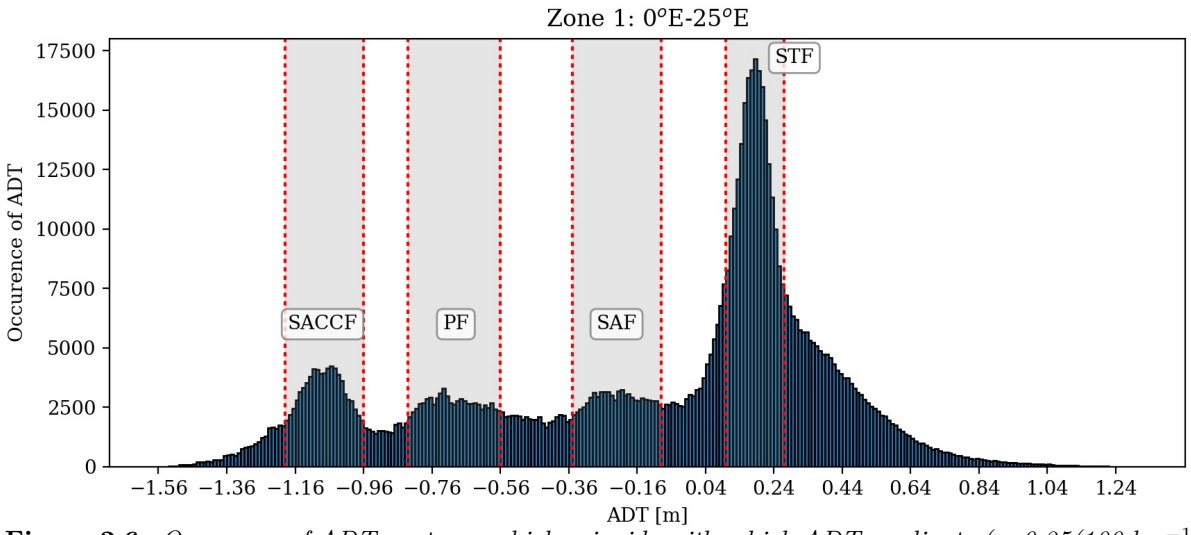

Figure 2.6: *Occurence of ADT contours which coincide with a high ADT gradients (> 0.25(100 km^{-1})) in the sector 0-30° E.*

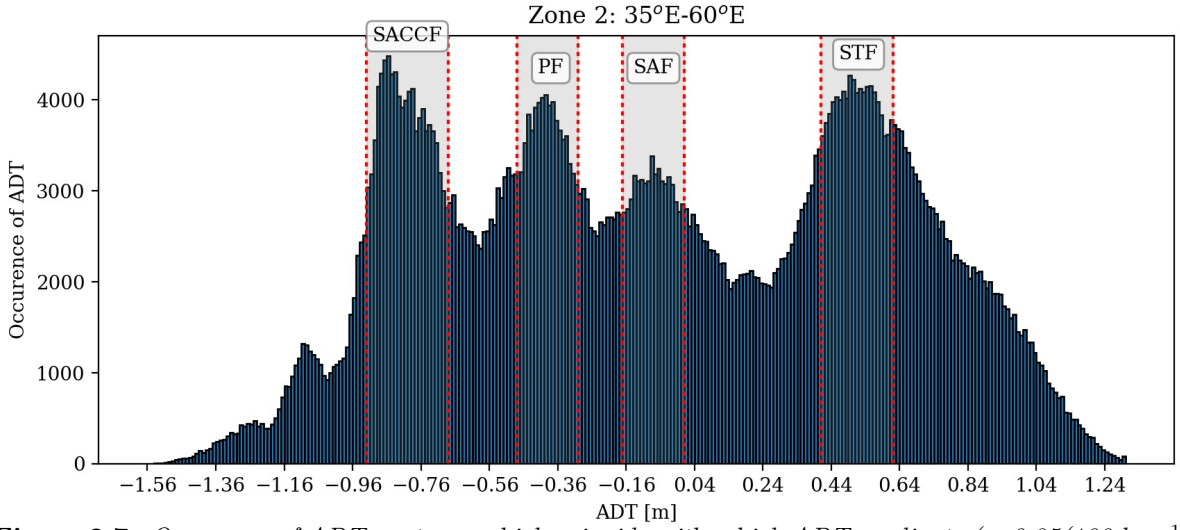

Figure 2.7: *Occurence of ADT contours which coincide with a high ADT gradients (> 0.25(100 km^{-1})) in the sector 30-60° E.*

However, we want to be more specific and provide the best estimate of the position of the fronts in our region of interest. Therefore, based on an approach similar to the one described by Sokolov and Rintoul (2007), we present an update of the positions of the fronts in the region 0-60°E/60-30°S. We use 24 years (1993-2016) of daily Aviso Absolute Dynamic Topography (ADT) product. For each day and each longitude, ADT gradients are computed and a threshold is used in order to keep only the higher SSH gradient regions. Sokolov and Rintoul (2007) uses a threshold of 0.25 m per 100 km which happens to be the best value in our case as well. Hence, only values bigger than this threshold are considered. Then, these values of ADT gradients are associated to the corresponding ADT contour found at the same location. Next, we divide the region around the archipelago in two sectors (0°-25°E and 35°-60°E), one on each side of the fracture zone, and average the ADT values over longitudes. It is well known that the ridge at 30°E has a substantial influence over the pathway of the fronts, that is why we decide to share its influence in

two distinct zones. The frequency distribution of the ADT contours over the 24 years is then visualised by plotting a histogram for each sector (Figure 2.6 and Figure 2.7). Four peaks can be distinguished and are assigned to the following fronts: the STF, SAF, PF and SACCF. We fit a normal distribution around each peak and extract the average ADT contour. The means represent the optimized ADT values which best describe the positions of the fronts. The results are given in Table 2.1. Note that our criteria are different from those determined by Sokolov and Rintoul (2009a), probably due to the fact that we use a different dataset and that our method focuses only on a small region and not on the whole ACC.

Front	0-25°E	35-60°E	Mean
STF	0.18	0.51	0.34
SAF	-0.22	-0.09	-0.15
PF	-0.69	-0.39	-0.54
SACCF	-1.07	-0.80	-0.93

Table 2.1: *Optimized ADT values in meters associated with each fronts in two sectors (0°-30°E and 30°-60°E). The last column is the mean of the two sectors. These criteria are derived from 24 years of Aviso Mapped Absolute Dynamic Topography.*

3 Offshore and local controls for the current and temperature around the Prince Edward Islands

Contents

3.1 Introduction

The Prince Edward Islands constitute a unique system: they form a coastal oceanic environment embedded into the largest current system which is the ACC. Therefore, this archipelago is under the direct influence of large scale physical processes as well as local processes.

One of the most significant large scale process driving the physical dynamics of the region is the latitudinal position of the frontal systems and their interaction with the islands. As aforementioned, the PEIs are sandwiched between two fronts of the ACC: the SAF and the PF. Some studies have shown that there is a tendency for the ACC fronts to shift southwards during the past 50 years (Gille, 2002; Gille, 2008; Downes et al., 2011). Because the ACC is strongly controlled by the topography in some locations, this poleward displacement has been shown to be likely not uniform in the Southern Ocean (Gille, 1994; Dong et al., 2006). However, more recent studies have shown no coherent trend in the meridional position of the ACC fronts (Graham et al., 2012; Gille, 2014; Shao et al., 2015; Chapman, 2017), except in particular regions where the ACC is weakly constrained by the bottom topography such as Abyssal plains, southeast Indian and southeast Pacific basins(Sallée et al., 2008; Kim and Orsi, 2014).

Ansorge et al. (2009) presented historical data (modified from Pakhomov and Chown, 2003) from over 30 crossings of the SAF in the upstream region between 1959 and 1999, showing a possible southward shift in the position of the SAF (between 28°-37°E), but claimed that the result was not conclusive. In the same paper, subsurface observations between 1972 and 1994 in the upstream region of the islands are also presented (modified from Gille, 2002) and seem to confirm a southward migration of the SAF. However, this result was based on only six observations of subsurface temperature and salinity made upstream of the archipelago. There are still not enough in-situ data to assess a long-term southward shift in the position of the SAF in the vicinity of PEIs. Based on these results, Allan et al. (2013) has suggested that this southward shift of the ACC and in particular its frontal systems corresponds in time to climate changes reported at the PEIs. The southward migration of the SAF, by favouring a through-flow regime (Pakhomov et al., 2000), seems to have contributed to a long-term decline in the frequency of phytoplankton blooms in the inter-island region (Ansorge et al., 1999; Perissinotto et al., 2000).

Another important offshore feature in the region is the strong mesoscale activity. The islands lie directly downstream of a spot of enhanced eddy production, where the ACC interacts with the SWIR, a prominent topographic feature. Many investigations have shown that the ecosystem of the PEIs benefit substantially from the mesoscale features created at the SWIR (Ansorge et al., 1999; Froneman et al., 1999; Ansorge and Lutjeharms, 2002; Ansorge and Lutjeharms, 2003; Ansorge et al., 2004; Nel et al., 2001; Durgadoo et al., 2010).

These large scale physical processes strongly shape the PEIs ecosystems but others processes, at local scale, have also an influence on oceanographic conditions of the islands (le Roux and McGeoch, 2008; Smith, 2002; Allan et al., 2013).
The aim of this chapter is to address the different forcings driving the oceanic variability at the PEIs. The question tackled here is: what are the impacts of offshore and local processes on the circulation observed at the islands?
In the first place, we suggest studying the temporal variability of the offshore dynamics such as the frontal positions and the mesoscale activity in the vicinity of the archipelago. Secondly, we focus on the more local variability by analysing in-situ data (moorings and oceanographic cruise data) in order to evaluate the importance of coastal processes such as tides and local winds.

3.2 Offshore Processes

3.2.1 Position and variation of the Polar and Subantarctic Fronts

In Figure 3.1 we show the root mean square of the Sea Level Anomaly, with the mean positions of the SAF and the PF. The positions of the fronts (see Table 2.1) are determined by following a method similar to the one described by Sokolov and Rintoul (2007), adapted here to the specificities of our region of interest. The aim of the methodology is to associate fronts with sea surface height contours coinciding with zones of large sea surface gradients as shown by section 2.4.
The frontal locations observed in this study are consistent with positions illustrated in other studies for the region of the PEIs (Durgadoo et al., 2010; Ansorge et al., 2009; Swart et al., 2008). At 30°E, both fronts are deflected southwards when they reach the fracture at the SWIR. Downstream, the SAF goes slightly northwards following the eastern flank of the SWIR and then is diverted north-westwards between Del Caño Rise and the Crozet Plateau, before turning back and continuing eastwards. On the other hand, after going through the ABFZ, the PF does not seem constrained by bottom topography. It goes eastwards with a slight meandering.

Now we have described the mean state of the frontal positions and the sea surface dynamics in the studied region, the second step is to examine the temporal evolution of the latitudinal frontal positions during the period 1993-2017, in order to assess the southward shift mentioned by Ansorge et al. (2009). Time series of the positions of the SAF and the PF averaged between 35° and 40°E, in the vicinity of the PEIs are displayed in Figure 3.2 a. The frontal positions are inferred from elevation of the sea surface thus we make sure to remove an uniform global mean sea level rise of 3.4 cm per decade, accounted for by ocean thermal expansion and land-ice melt to avoid any trend caused by sea level rise (Cazenave and Llovel, 2010). The times series exhibit a marked interannual variability in

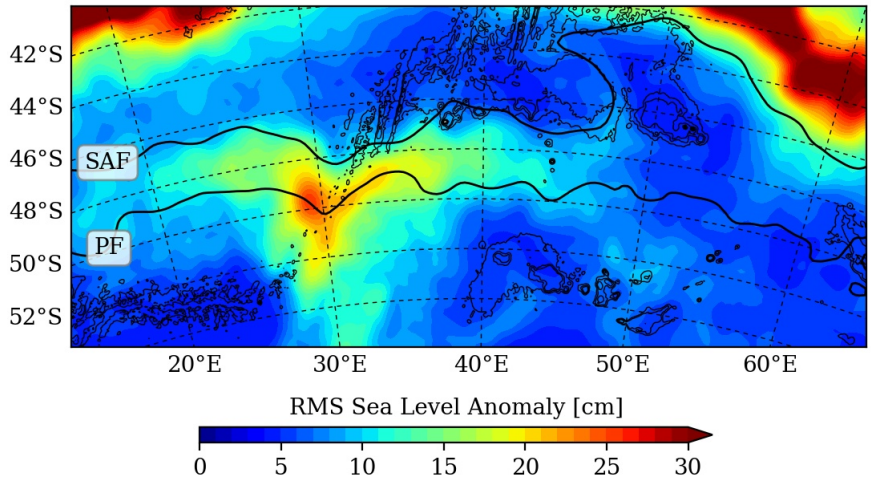

Figure 3.1: *The root mean square of Sea Level Anomaly averaged over the 1993-2017 period (Aviso). Bathymetric contours (1000 m, 2000 m, 3000 m) are overlaid in black (ETOPO2). The two black lines represents the mean positions of the SAF and the PF, found by using the method explained in section 2.4.*

the frontal positions, as well as intra-annual variability (monthly time scale). Indeed, the locations of both fronts vary from one year to another as well as from one month to another, allowing the SAF to switch from a position north of the islands to a position south of the islands, within the same year. For example, in 1995, the SAF is originally south of the PEIs and then moves northwards and ends up being south of the islands again. The PF shows a similar behaviour, moving north and south at the same time as the SAF but with a different spatial amplitude. This very high variability of the fronts in the region is consistent with the root mean square of the sea level anomaly shown on Figure 3.1. Moreover, at lower frequency, Figure 3.2 a highlights a multi-decadal southward trend in the SAF and PF locations. These long-term variations are significant at 95% confidence level in both SAF and PF cases. In 24 years, the SAF and PF have shifted of 0.3° and 0.2° southwards respectively.

In order to study in more detail the variability of the positions of the fronts, the signals are decomposed into different frequency. At first, the mean and the trend of the times series are removed and the seasonal cycle is computed. As we can see on Figure 3.2 b the seasonal cycle is weak and represents only 2% and 1% of the total variance of the SAF and PF variations respectively.

Then, we apply a low-pass filter, based on Lanczos method, to extract the periods longer than 5 years. In Figure 3.2 c, we show the low frequency part of the signal and it displays an interesting pattern that reminds the decadal variations of the Southern Annular Oscillation index (Figure 1.6), especially for the SAF time series, which will be discussed later. This part of the signal explains about 11% of the total variance of the SAF and a bit more for the PF (18%).

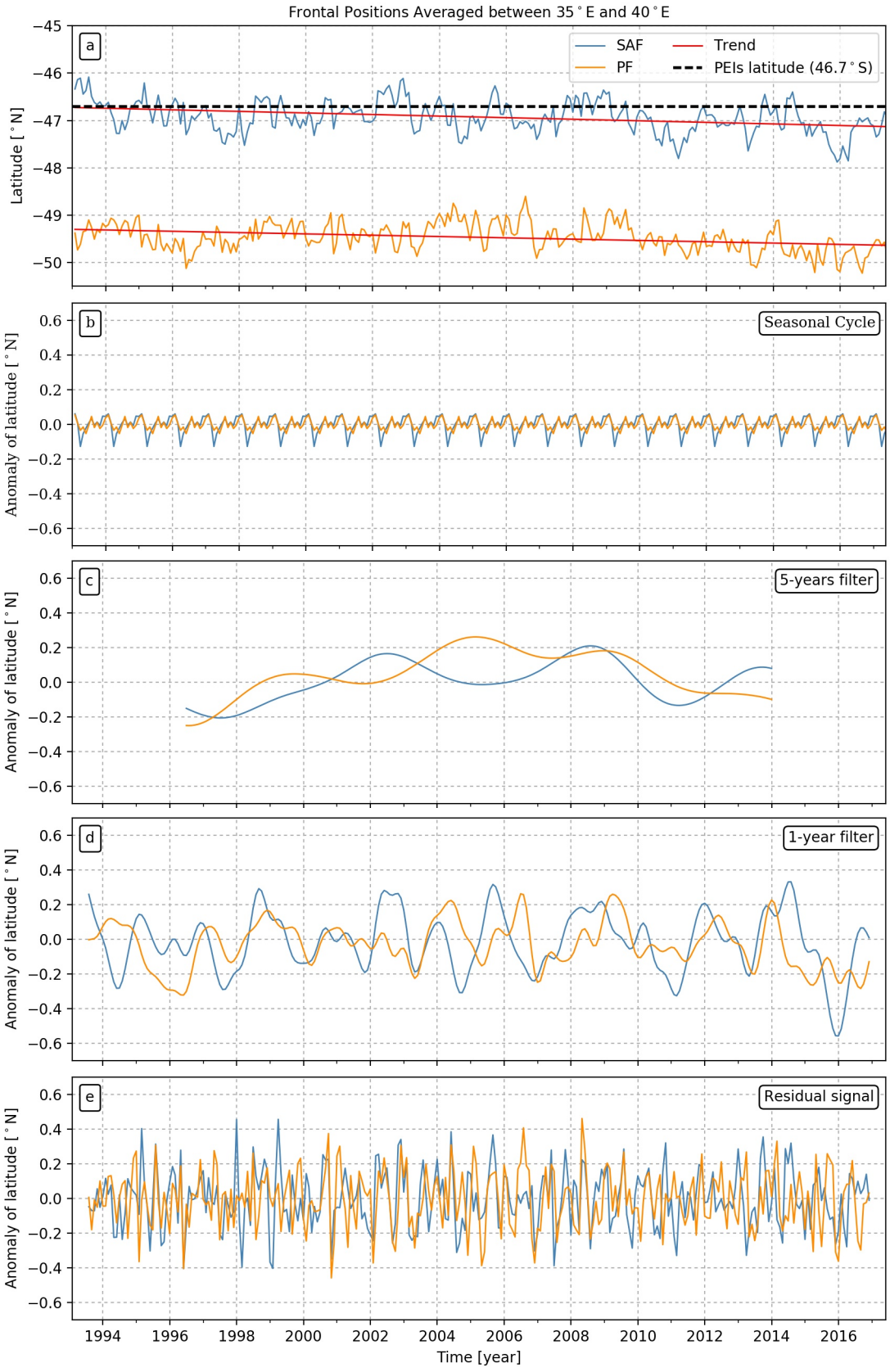

Figure 3.2: *(a) Time series (for the period January 1993-April 2017) of monthly latitudinal position of the (blue) SAF and (orange) PF, averaged between 35° E and 40° E. The red lines are the trends of the frontal positions (significant at 95% confidence level). The dashed line is the islands latitude. (b) Seasonal cycle of the positions of the fronts. (c) 5-year low pass filter. (d) 1-year low pass filter. (e) Residual signal after removing the mean, the trend, the seasonal cycle, time-scales longer than 5 years and than 1 year from the original signal (a).*

After filtering out the periods longer than 5 years, another low-pass filter (still based on Lanczos) is applied to extract the part of the signal with periods between 5 and 1 year (Figure 3.2 d). There is still a strong interannual varibility in the frontal positions which accounts for 25% and 20% of the total variance of the positions of the SAF and the PF. Finally, Figure 3.2 e illustrates the residual time series of the positions of the SAF and the PF which are the remaining parts of the initial signals after removing the mean, the trend, the seasonal cycle and the periods longer than 1 year. It displays a high intra-annual variability explaining about 24% of the total variance of the SAF and 32% of the PF variance. Analysing the SAF and PF signals by quantifying the variances associated to different part of these signals has highlighted the fact that the variability in frontal positions is mostly interranual and intra-annual.

If we come back to Figure 3.2 a, two periods can be distinguished: 1998-2004 and 2010-2015. During the first period, Figure 3.2 a displays a SAF fluctuating around the PEIs latitude but globally staying at the latitude of the islands. However, between the period 1998-2004 and the period 2010-2015, the SAF and the PF seem to have migrated southwards which, in a global context, have been shown to be consistent(Gille, 2008; Morrow et al., 2008; Sprintall, 2008). In Figure 3.3, we illustrates the positions of the SAF and the PF averaged over these two different periods and shows that the SAF and the PF have migrated southwards. The SAF lies in closer proximity to the islands at the 2010-2015 period. It is well known that the position of the SAF, separating subantarctic waters to the north from colder Antarctic waters to the south, has an important influence on hydrographic and biologic conditions of the islands: the closer it is, the stronger is the current between the two islands. In this case, eddies found in the inter-island region are fewer (Ansorge et al., 1999; Perissinotto et al., 2000).

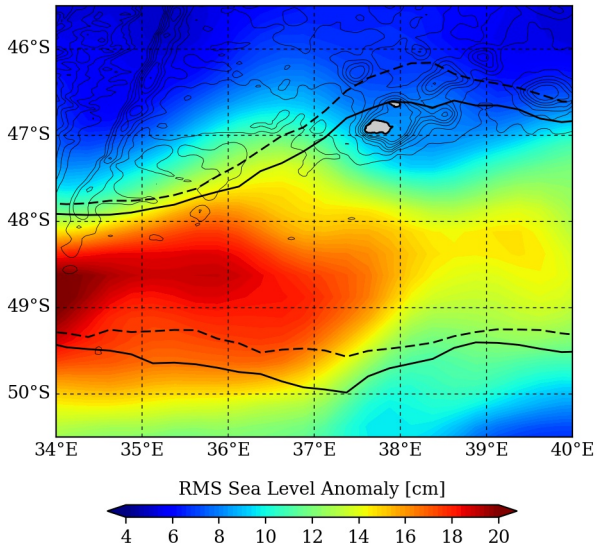

Figure 3.3: *Positions of the SAF and PF averaged over (dashed line) 1998-2004 and (solid line) 2010-2015, overlaid to the root mean square of sea level anomaly. The fronts have shifted southwards between the two periods. Bathymetric contours are plotted in grey.*

This result from altimetry is consistent with previous global observations made in the Southern Ocean and supports the hypothesis of a SAF southward migration in the region of the PEIs. Since 2009, the SAF has remained, in general, south of the islands, except for two brief excursions in 2013 and one in 2014.

Link with large-scale pattern

Previously, we have brought up the fact that the low frequency part of the SAF signal follows similar variations as the SAM index (Figure 3.2 c).
To investigate this similarity, a 5-years Lanczos filter is applied to monthly SAM index data over the period 1993-2017 and the residual signal is compared to the low frequency part of the SAF signal. Locally, Figure 3.4 a shows that an increase in SAM index corresponds to a SAF moving towards high latitude (southwards) and vice-versa. Note that the correlation between the low frequency parts of the SAF and SAM is weak (0.61) but remained significant. This result is in agreement with what has been observed in the Southern Ocean: SAM index moving toward an increasingly positive phase resulting in a strengthening of the circumpolar westerly winds causing a poleward shift of the ACC (Thompson and Solomon, 2002; Gille, 2008; Morrow et al., 2008; Sprintall, 2008). The interannual signals (Figure 3.4 b) show also similar fluctuations but with some discrepancies sometimes with the SAF going north whereas the SAM index is increasing towards positive phase. In this case, the correlation between the two signals is very low, about 0.2.

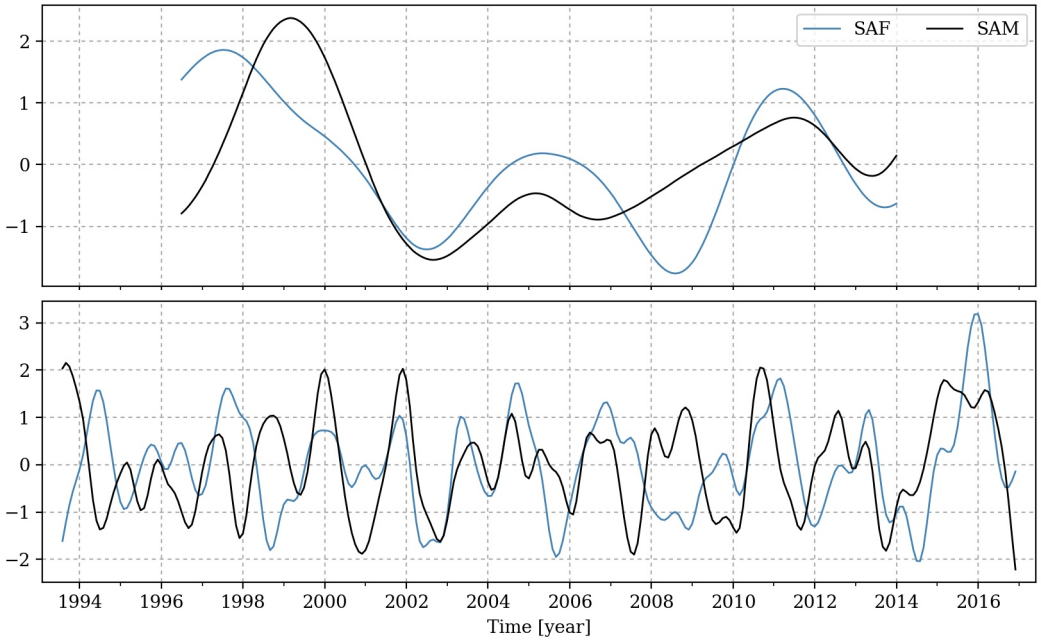

Figure 3.4: *Time series of monthly (blue) negative latitudinal position of the SAF and (black) SAM index after filtering out (a) the periods shorter than 5 years and (b) the periods shorter than 5 years and longer than 1 year. The data have been normalised.*

It is well known that fronts are preferable foraging areas for many predators because of an enhancement of local primary production (Bost et al., 1997; Jonker and Bester, 1998; Nel et al., 2001). Bost et al. (2015) have shown that large-scale climatic anomalies in the Southern Hemisphere affect the foraging behaviour and population dynamics of some predators, especially the king penguins, by shifting the foraging zone southwards. In this section, we have highlighted a link between the SAF position and SAM index at low frequency at the islands. A consequence of an increase in positive SAM index is a poleward shift of the ACC, which leads to a shift of the main food source further south. Consequently, the foraging distances are increased which likely could impact the top predator population demography of the PEIs.

3.2.2 Eddy Generation at the South West Indian Ridge

In this section, we focus on the mesoscale eddy activity, another important feature of the region.

As seen in Figure 3.1, the SWIR exerts a strong topographic control over the pathway of the ACC. Upstream the ridge, the ACC can be related to a laminar flow, with parallel streamlines which are homogeneously distributed (see figure 1.11: the streamlines are the grey lines). At the ridge, the current is deflected southwards. After the ridge, the flow is disturbed and becomes more turbulent. Some of the streamlines follow the bathymetry on the eastern flank of the ridge and then are deflected northwards at 48°E between the Del Caño Rise and the Crozet Plateau. A "hotspot" of high mesoscale acitivity is found at the SWIR, roughly centred at 50°S-30°E, corresponding to the position of the Andrew Bain Fracture Zone. This location coincides to the area where the ridge starts to interact with the flow.

Mesoscale processes have been shown to influence the ecosystems on the islands. As a first descriptive approach, we compute the geostrophic surface Eddy Kinetic Energy (EKE) in the region from altimetry data. It is estimated from surface geostrophic currents as :

$$EKE = \frac{u_g'^2 + v_g'^2}{2}$$

where u_g' and v_g' are the zonal and meridional surface geostrophic velocity fluctuations calculated as :

$$u_g' = -\frac{g}{f}\frac{\partial \eta'}{\partial y}$$

$$v_g' = \frac{g}{f}\frac{\partial \eta'}{\partial x}$$

where g is the gravitational acceleration, f is the Coriolis parameter and η' is the elevation anomaly of the sea surface.

The spatio-temporal variability of the EKE of the PEIs region is investigated using 25

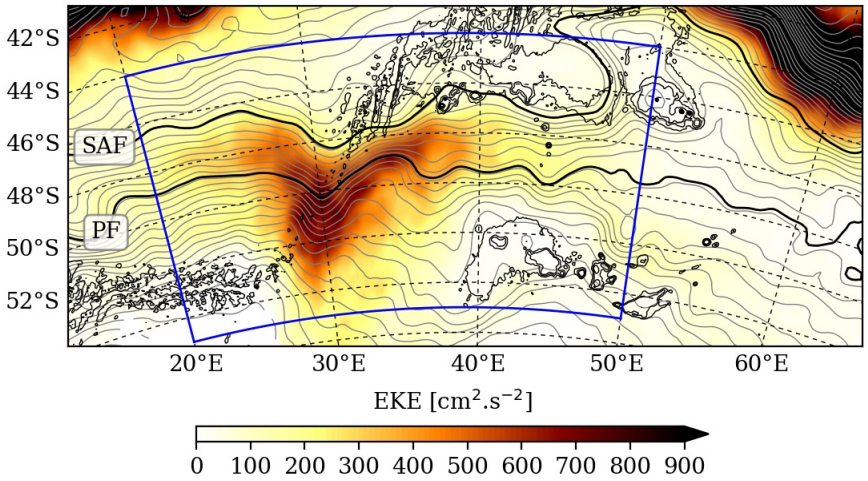

Figure 3.5: *EKE averaged over the 1993-2017 period and derived from altimetry (Aviso). The blue frame is the area where EKE is averaged to get Figure 3.6. The two thick black lines are the SAF the PF. Bathymetric contours (1000 m, 2000 m, 3000 m) are overlaid in black (ETOPO2).*

years of satellite data. In Figure 3.5, we show a region of enhanced EKE, slightly upstream the PEIs. EKE displays a "horse-shoe" pattern (similarly displayed by the RMS sea level anomaly on Figure 3.1), spreading on both sides of the SWIR. The core of EKE is centred at the ABFZ at 50°S-30°E. This "hotspot" shows EKE values reaching 700 $cm^2.s^{-2}$, which is high compared to the rest of the ACC displaying values between 200 and 400 $cm^2.s^{-2}$, except at some spots similar to the one we describe here. High EKE values observed on north-west and north-east corners of Figure 3.5 are associated to the Agulhas current and the Agulhas Return Current, which are not investigated here and presumably do not influence the dynamics of our study area. As this peculiar EKE pattern has been widely described, in the following we focus on the temporal variability of EKE. The time series of EKE averaged in the box 20°-50°E/44°-55°S is shown on Figure 3.6 a. First, we notice large interannual and intra-annual variabilities. Interestingly, if we look at the 2009-2015 period, when EKE is particularly low in the region, the SAF and PF are situated south of their mean position (Figure 3.2 a). If we look at the low frequency modulation, the EKE time series exhibit a negative trend. A decrease of 9 $cm^2.s^{-2}$ is observed over the 25 years, a trend that is significant at 95% confidence level.

As it has been undertaken for the frontal positions time series, the EKE signal is decomposed in several signals. Following exactly the same method, the mean and the trend are removed and Lanczos filters are used to remove step by step some parts of the EKE signal. As previously, the seasonal cycle is unsubstantial (Figure 3.6 b), representing scarcely 1% of the variance of the signal. In Figure 3.6 c, we illustrate the part of the signal with periods longer than 5 years and explains about 14% of the total variance. Then, periods longer than 5 years are filtered out and Figure 3.6 d displays the part of EKE signal whose periods are longer than 1 year. Similarly to frontal positions signals, we still notice a significant interannual variability, explaining 32% of the total variance.

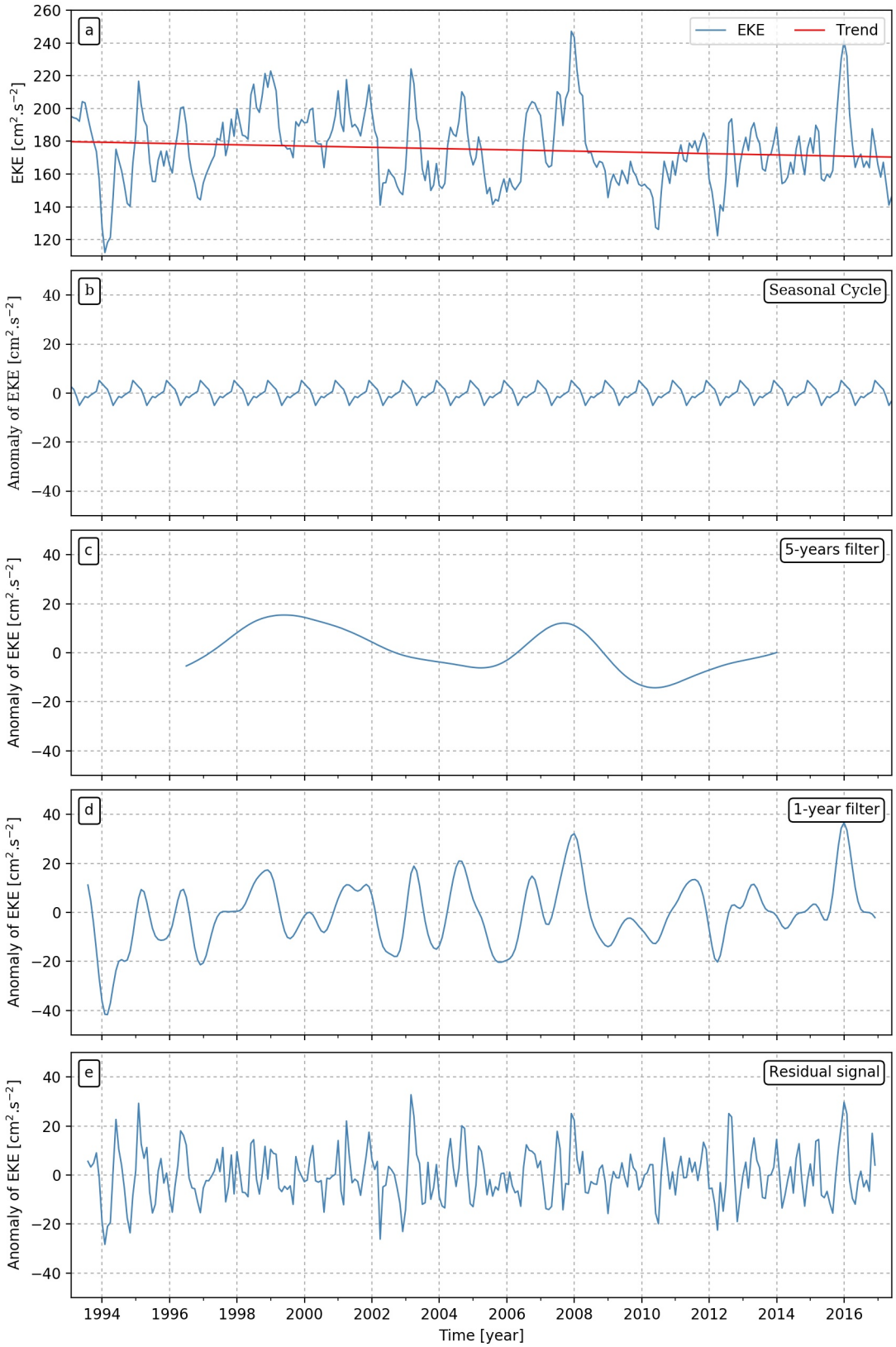

Figure 3.6: *(a) Time series (for the period January 1993-April 2017) of monthly EKE, averaged within the blue frame shown on Figure 3.5. The red line are the trend of EKE (significant at 95% confidence level). (b) Seasonal cycle of EKE. (c) 5-year low pass filter. (d) 1-year low pass filter. (e) Residual signal after removing the mean, the trend, the seasonal cycle, time-scales longer than 5 years and than 1 year from the raw signal (a).*

The residual signal (Figure 3.6 e), after filtering out periods longer than 1 year, highlight a large intra-annual variability, accounting for 21% of the total variance of EKE. The decomposition of this signal shows the presence of an important interannual and intra-annual variability of EKE in the region.

Summary of Section 3.2: Offshore processes

Offshore processes, such as the position on the frontal systems and the mesoscale activity, are important drivers of the physical dynamics around the islands and shape their ecosystem. In this section, based on altimetry, we have mainly studied the temporal variability of these drivers:

- We show that the SAF and the PF exhibit high interannual (20% and 25% of the total variance) and intra-annual (24% and 32% of the total variance) variability in their position in the PEIs region.
- Both SAF and PF reveal a multi-decadal southward trend in their position which is consistent with global observations made on frontal systems of the ACC.
- The SAF presents similar time variations as SAM index at low and interannual frequencies. At high frequency, the SAF variations is mainly dominated by the mesoscale eddy signature, while at low frequency, we see the response of the SAF to the large-scale wind pattern which is modulated by the SAM.
- The mesoscale activity shows also large interannual (32% of the total variance) and intra-annual (21% of the total variance) variability.
- A negative trend of EKE has been also observed in the region revealing a reduction of 9 $cm^2.s^{-2}$ over 25 years.

3.3 Local Processes

3.3.1 Evidence of mesoscale activity and SAF impacts on the PEIs

Ocean temperature at the islands

In the previous section, we have studied the offshore processes influencing the islands. Here, we focus on local dynamics using data from two moorings which have been deployed in the inter-island region in 2014 (see Figure 2.1 for their location). The moorings record hourly temperature and current velocity through the water column. The sub-surface floats provide temperature readings approximately 5 m above the sea floor (at 169 m and 318 m). In Figure 3.7 a, we illustrate the temperature recorded over two years by the two moorings, from April 2014 to April 2016. Due to the short period in which data has been collected and also that the probes are at the sea floor, the seasonal signal is not clearly defined. The time series reveal a high temperature variability (between 2.5°C and 6.3°C) and shows that the two moorings temperature follow similar fluctuations. Between December 2014 and January 2015, the temperature drops from 4°C to 2.8°C for Mooring 1 and from 3.7°C to 2.5°C for Mooring 2 before increasing substantially in April-May 2015. A "hot event" is seen, as well, around April 2016. These three noteworthy events are well recorded by both moorings (dashed circles on Figure 3.7 a). Nonetheless, the difference between the two time series changes over time. For instance, from August 2014 to January 2015, the two temperatures have similar fluctuations, while from February 2015 to September 2015, they show bigger discrepancies. This may be explained by the fact that the temperatures are recorded at different depths and could be a signature of changes in vertical stratification.

In parallel, on Figure 3.7 b, we present a Hovmöller diagram of sea level anomalies obtained from Aviso satellite data for the corresponding moorings record time period. It illustrates the anomalies at 37.87°E (longitude of the PEIs) as a function of time and latitude and shows the propagation of the anomalies in the vicinity of the PEIs. Past investigations have provided confidence that changes in SLA actually means changes in ocean properties (Ansorge and Lutjeharms, 2002). Then, SLA can be associated with mesoscale features (cyclone with negative SLA and anticyclone with positive SLA), describing the propagation of SLA comes down to describe the propagation of eddies. The eddies come from the southwest, travel northeastwards and drift past the islands (Figure 3.5). The three arrows on Figure 3.7 b point out the three events highlighted on Figure 3.7 a by dashed circles. They show that the two warm events concur with anticyclones (positive anomalies) and that the cold event corresponds to a cyclone (negative anomalies) passing in the vicinity of the PEIs.

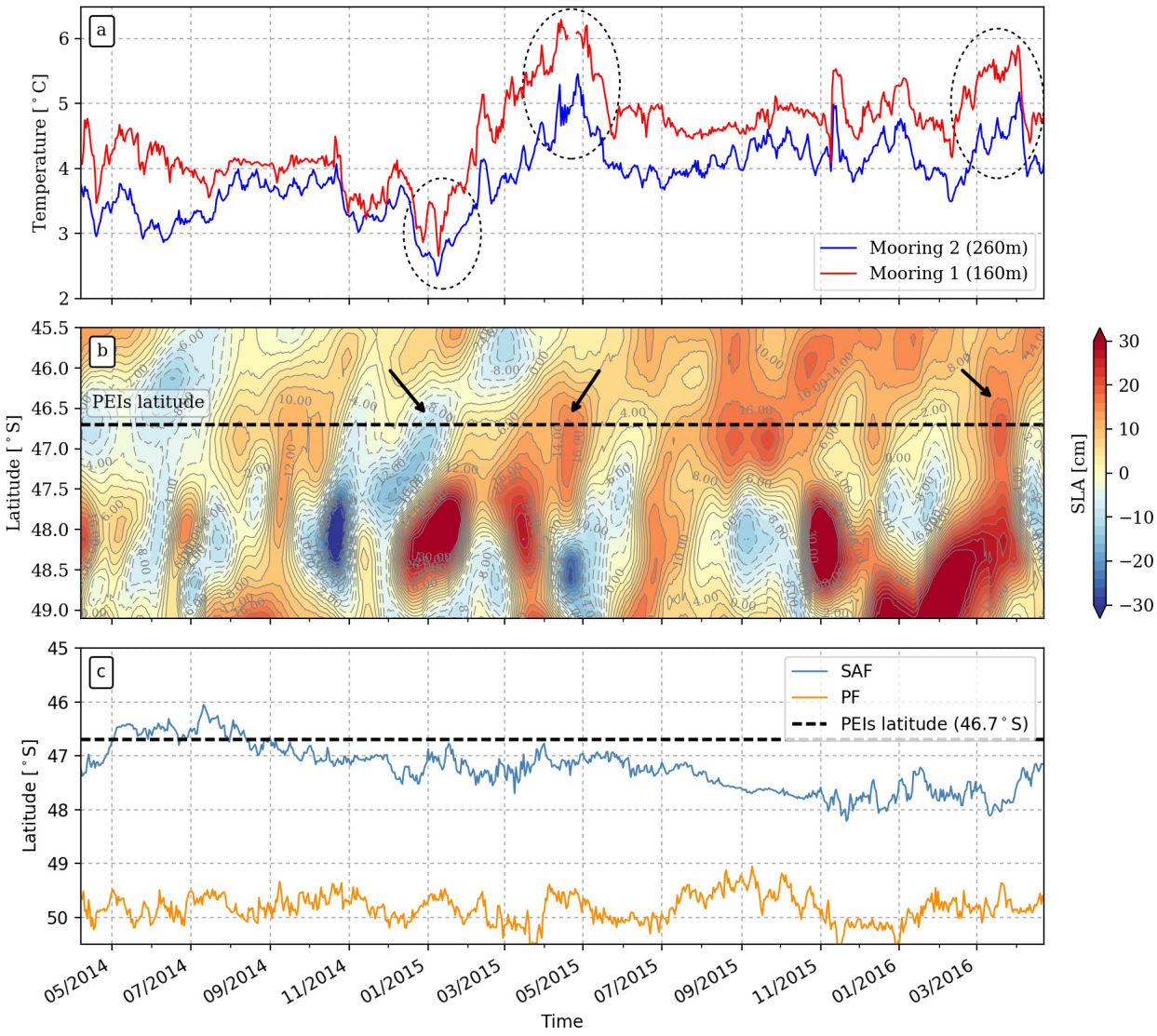

Figure 3.7: *(a) Time Ser3es of the temperature recorded by the two moorings at 160 m and 260 m, from April 2014 to April 2016. (b) Hovmöller diagram of Sea Level Anomaly from Aviso at 37.875° E. The three arrows indicate the anomalies corresponding to the three events circled on (a). (c) Positions of the SAF and PF in the vicinity of the islands (averaged between 35°-40° E). The black line on (b) and (c) shows the latitude of the archipelago 46.7° S.*

This suggests that the large-scale mesoscale activity described above (section 3.2.2) has a direct impact on the hydrodynamics at the islands, at least on the local temperature. Nonetheless, the resolution of altimetry data (1/4°) does not allow us to study the small scale processes which impact the moorings individually.

Another interesting thing highlighted by the mooring time series is that, at large time scale, we can differentiate three events:

- April 2014 - November 2014: cold and stable temperatures.
- November 2014 - June 2015: important temperatures fluctuations.
- June 2015 - April 2016: higher and stable temperatures.

In order to investigate this phenomenon, we plot the time series of the positions of the SAF and the PF for the moorings time period (Figure 3.7 c). For the first period, which is marked by cold temperature, we note that the SAF is mostly north of the islands, bringing cold water from the south in the surroundings of the archipelago. From November 2014 to June 2015, the SAF switches from a position north of the islands to a position south of the islands, staying in the close vicinity of them. During this period, the moorings temperatures experience high fluctuations caused by some mesoscale features passing through the PEIs. From June 2015 to April 2016, the SAF continues migrating southwards bringing subantarctic waters, warmer than the Antarctic waters lying south of the SAF, in the region of the islands. That is why we observe higher temperatures in the moorings data during this period.

Mixed Layer Depth

Besides the two moorings data, CTD transects have been performed in 2013, 2014 and 2015 during South African oceanographic cruises (see Chapter 2 for more details).
In Figure 3.8 a,b,c, we show the averaged profiles of temperature, salinity and density of the east-west transect (stations carried out during the transects are represented by stars on Figure 3.8 d,e,f) crossing the inter-island region for the three years. To determine the Mixed Layer Depth, the criterion selected is a threshold value of density from a near-surface value at 10 m depth (de Boyer Montégut et al., 2004): $\Delta\sigma_\theta = 0.03 kg.m^{-3}$. The maps of the anomalies of the sea surface (from Aviso satellite data) associated to the profiles and averaged over the transect time period, are shown as well. In 2013 (Figure 3.8 a,d) and 2015 (Figure 3.8 c,f), a negative anomaly is recorded passing south of the islands. The mixed layer is then 60 m deep and around 75 m deep respectively. In 2014, it is shallower than in 2013 and 2015. This might be caused by the presence of a cyclonic eddy (negative anomaly on Figure 3.8 e) passing close to the islands and upwelling the isopycnals between the two islands. Hence, in-situ data from CTD transects confirms that hydrodynamics of the PEIs are affected by mesoscale features that pass in their vicinity.

Mean current at the islands

As mentioned before, the moorings also record hourly current velocity between April 2014 and April 2016. The ADCPs record velocities over the water column above the mooring system. Mooring 1 has a workable dataset from 150 m to a minimum depth of 20 m above the surface while Mooring 2 has a workable dataset from 250 m extending to 30 m.
The depth-averaged flow, displayed on Figure 3.9 c, turns out to be weak (slower than 4 $cm.s^{-1}$) and points at different direction for each mooring. It is important to note that the bathymetry is not well known between the two islands, even though we use the SRTM30

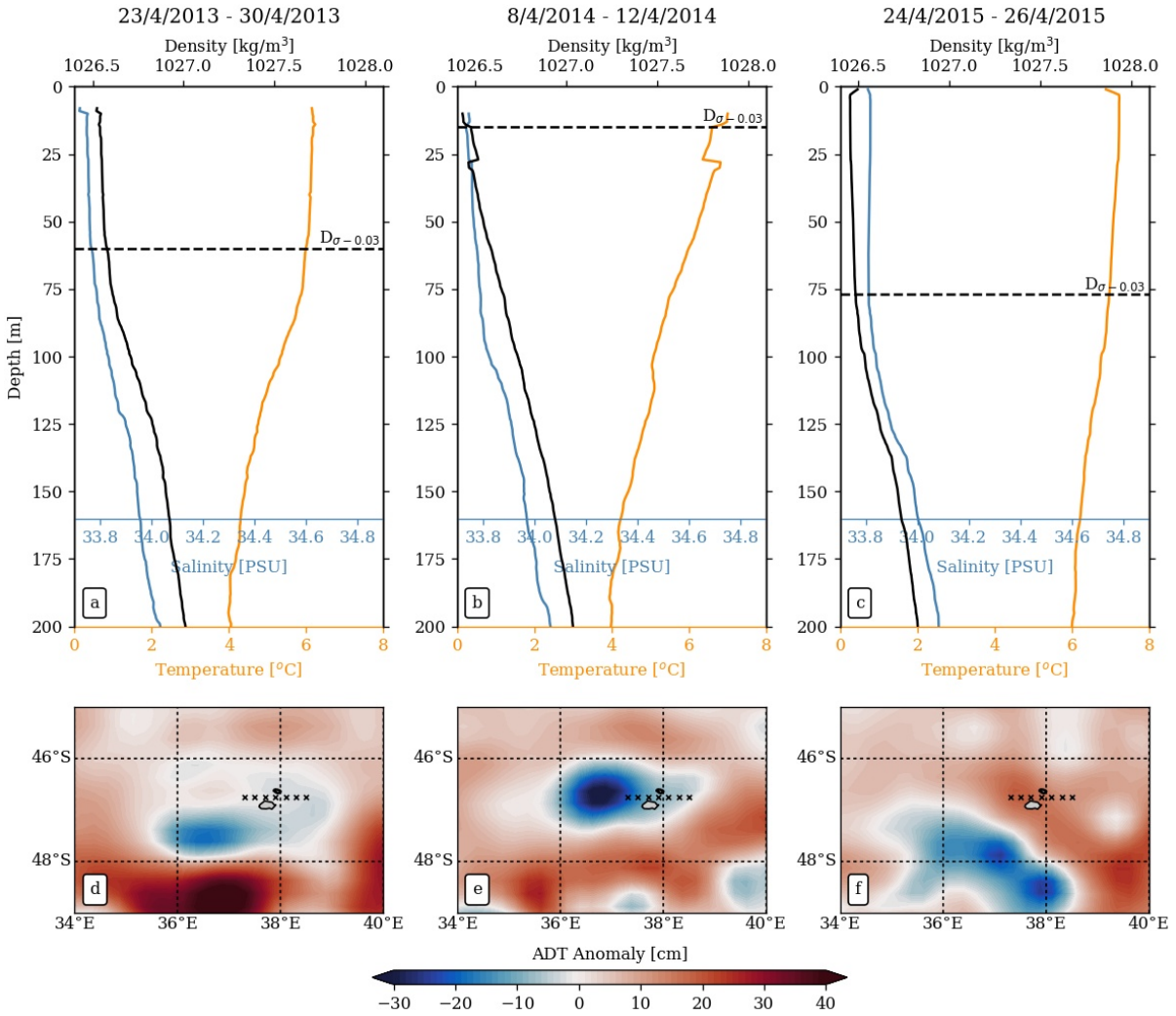

Figure 3.8: *(a,b,c) Temperature (orange), salinity (blue) and density (black) averaged profiles from the CTD transect represented by the black stars on figures d, e and f. The three bottom plots (d,e,f) are the maps of sea surface anomaly associated to the profiles. The anomaly is averaged over the transect time period. The black dashed line shows the Mixed Layer Depth $D_{\sigma-0.03}$ where the density has increased by 0.03 kg.m^{-3} as compared to the density at the reference depth at 10 m (de Boyer Montégut et al., 2004).*

bathymetry which has a resolution of 30 seconds (roughly 1 km). That is why there are inconsistencies between the real depth of the moorings. The bathymetry suggests that Mooring 2 is supposed to be located at a place where the ocean floor is deeper than Mooring 1, which is not the case on Figure 3.9 c.

If we look at the vertical mean profiles of the zonal and meridional velocity components (Figure 3.9 a,b), we note that the profiles are quite different, although the two devices are not very far from each other. Mooring 2, which is the deepest one, shows an eastward zonal velocity (positive value) in the first 150 m whereas the zonal velocity of Mooring 1 is going westwards (Figure 3.9 a). Zonal velocity of Mooring 2 reaches a maximum of about 5 cm.s^{-1} at 125 m before decreasing and turning westwards at 200 m depth. The meridional velocities are also different (Figure 3.9 b). In the top 50 m, Mooring 1 and Mooring 2 meridional velocities are in opposite directions, going northwards and southwards respectively. The meridional velocity of Mooring 2 is maximum near the

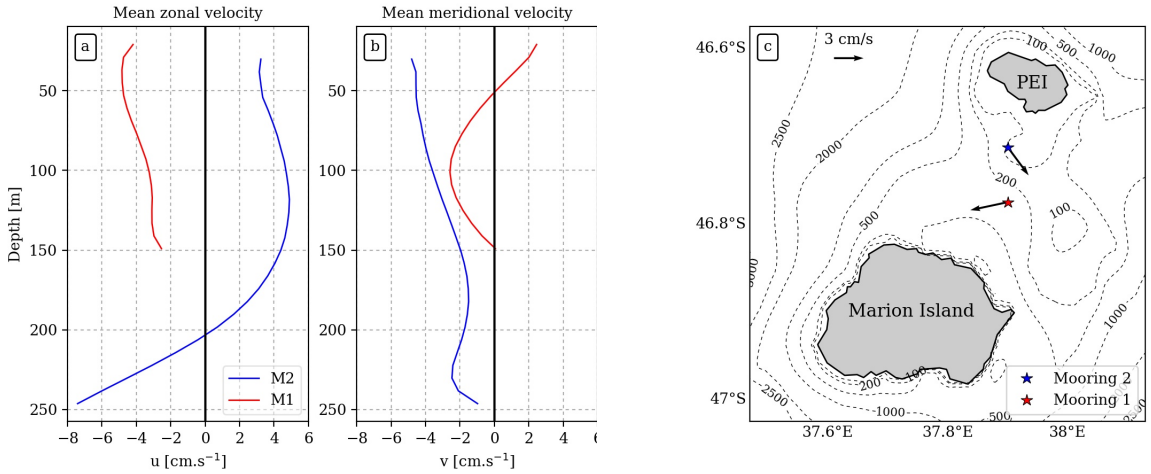

Figure 3.9: *Time averaged (a) zonal and (b) meridional velocity of (red) Mooring 1 and (blue) Mooring 2. The arrows on the figure (c) represent the current averaged over the mooring depth. The bathymetry is from SRTM30.*

surface and decreases until 175 m and then increases slightly before decreasing again at 230 m. Mooring 1 shows a southward flow located between 50 m and 150 m with a maximum of 2.5 cm.s^{-1} at 100 m. Considering that the standard deviations (calculated at each depth) go from 10 cm.s^{-1} to up to 20 cm.s^{-1}, longer time series are required to assess the significance of the mean currents.

3.3.2 Importance of tides at the islands

A large signal dominating the main current time series appears to be a tidal signal which has not been properly described in this region yet. In order to investigate this hypothesis, we first perform a harmonic analysis on both moorings velocity components (u and v) to describe the tidal signal. In the following, because the results of the harmonic analysis are very similar for the zonal and meridional velocity components, we choose to show only the results of the study performed on the zonal components. Secondly, we apply a filter to the data to remove the tidal signal and analyse the residual current at the moorings.

Extraction of tidal currents: Harmonic analysis

At first, the raw currents are averaged over the the mooring column, 300 m and 250 m respectively. Then the harmonic tidal components are extracted using the Python harmonic analysis tool t_tide [1].

Since we study a depth averaged current, it is important to specify that we focus on the quasi-barotropic part of the tide. Indeed, because the moorings are subsurface, they do not record velocity over the entire water column. Figure 3.10 a,c illustrates the results from the harmonics analysis performed on the depth averaged zonal speed. The top panels show the major tidal components and the bottom panels are the power spectra density

[1] `https://github.com/moflaher/ttide_py`

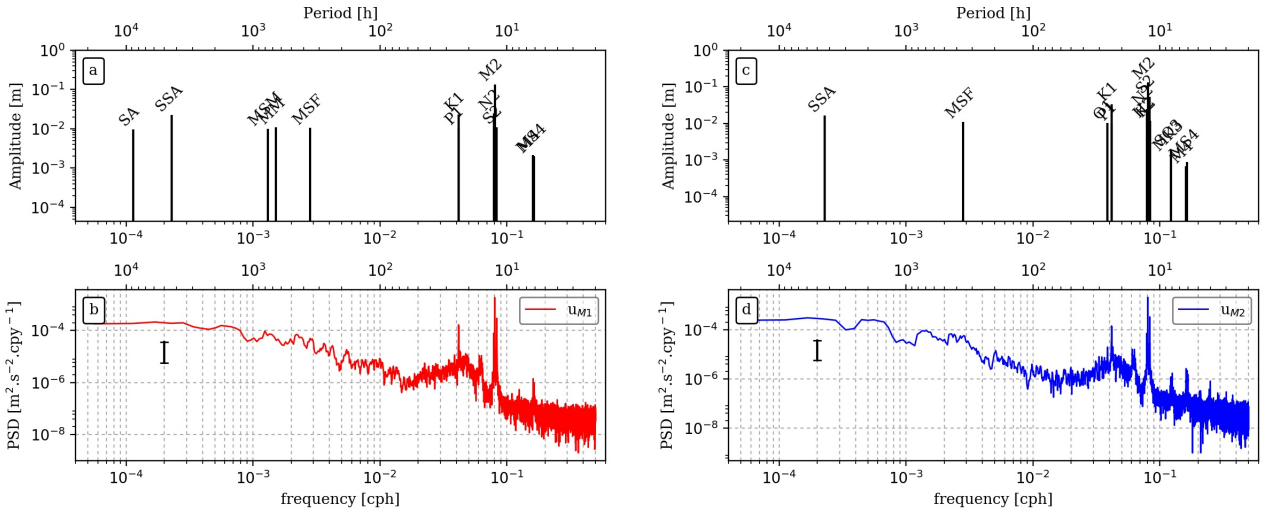

Figure 3.10: *(a) and (c) represent the tidal constituents (SA, SSA, K1, M2, MSF ...) with 95% CI estimated for Mooring 1 and Mooring 2 respectively. (b) and (d) are the Power Spectral Density (PSD on the y-axis) of quasi-barotropic zonal current from Mooring 1 and Mooring 2. The black vertical bars show the 95% uncertainty level.*

computed for the zonal velocity from the moorings. In parallel, a spectral analysis is carried out using multitaper method with three windows.

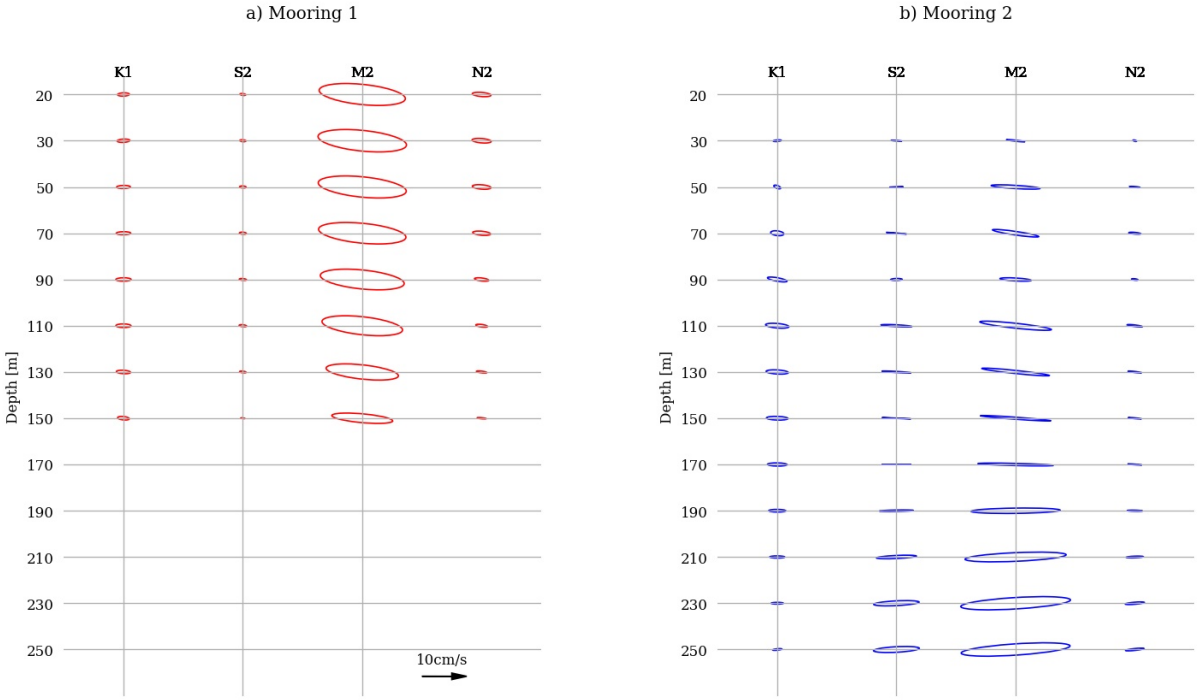

Figure 3.11: *Tidal ellipses of K1, S2, M2 and N2 constituents at different depths for (a) Mooring 1 and (b) Mooring 2.*

The spectral analysis (Figure 3.10 b,d) shows four significant peaks which are the dominating periods of variability: 23.9h, 12h, 12.42h and 12.66h. If we compare the two spectra with their respective harmonics analysis, they correspond to the following high amplitude tidal constituents: the diurnal K1 tidal constituent, and the semi-diurnal S2, M2 and N2 constituents. There are also secondary peaks at about 6h period on both

spectra, corresponding to the M4 and MS4 tidal constituents. Figure 3.10 d displays other peaks at about 8h period associated to the SO3 and MK3 tidal consituents. The Figure 3.10 a,c shows also some high amplitude-low frequency constituents (SA, SSA, MSF...) which do not seem to impact the current variability (no peak on the spectra corresponds to these harmonics). This result highlights that the variability of the current recorded between the islands is strongly influenced by the quasi-barotropic tide and that the latter affects similarly the two moorings. So far, we have focused on the barotropic tidal current because we have studied depth averaged current. This component of the tide is generated by the astronomical forcing and is depth independent.

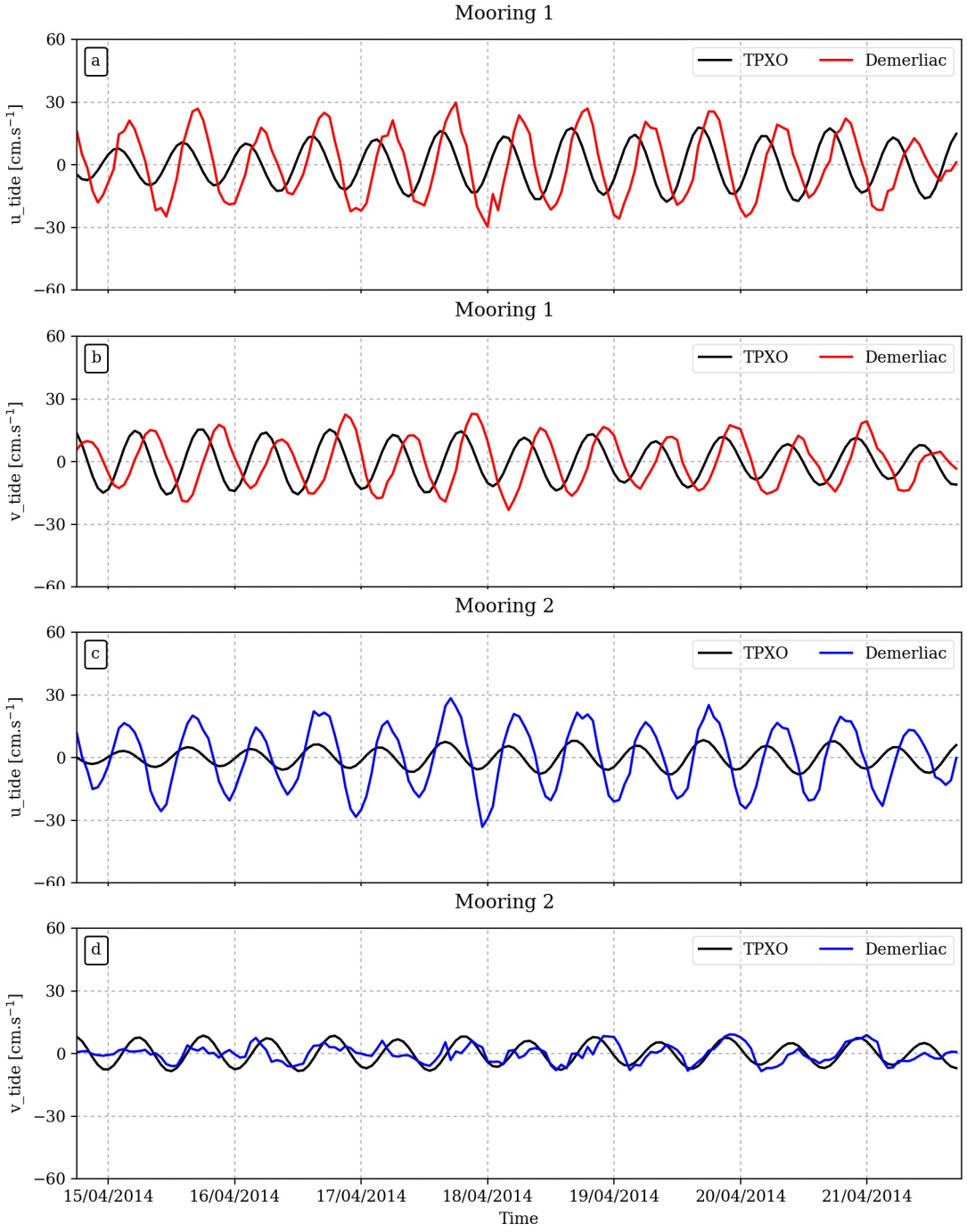

Figure 3.12: *(a,c)Zonal and (b,d) meridional tidal component from (black) TPXO, (red) Mooring 1 and (blue) Mooring 2.*

The baroclinic tides depends on depth and could be described as internal waves propagating at tidal frequencies. Figure 3.11 shows tidal ellipses for the principal tidal constituents of the current which have been discussed (K1, S2, M2, N2) and reveals that the magnitude of tidal ellipses varies with depth. It is particularly obvious for the M2 component. Mooring 1 shows a M2 ellipse decreasing with the depth whereas Mooring 2 shows a M2 ellipse increasing with the depth. Unfortunately, because the record depth range of Mooring 1 is limited, we can not know if M2 increases again from a certain depth. In Figure 3.11 b, S2 ellipse seems to increase with the depth as well.
Hence we conclude that not only the circulation at the moorings is affected by tide, but the baroclinic tide has different impacts on the two moorings. This could explain, at least partially, why the current meters recorded different velocities at the two moorings, as mentioned above. We complete this study of tides by comparing the tide recorded by the mooring to a global model ocean tide TPXO. This later best-fits, in a least-squares sense, the Laplace Tidal Equations and along track averaged data from TOPEX/Poseidon and Jason (on TOPEX/POSEIDON tracks since 2002) obtained with OTIS (OSU Tidal Inversion Software). The methods used to compute the model are described in details by Egbert et al. (1994) and further by Egbert et al. (2002). To compute the tides from the moorings quasi-barotropic velocities, we choose a Demerliac filter which comes from the vacumm library developed by ACTIMAR/IFREMER[2]. The Demerliac filter is based on 72 hours of data. It means that we need at least 3 days of observations which is our case (2 years of hourly data). It gives the filtered signal and the tide extracted from the raw signal. Figure 3.12 presents tides velocity components from the moorings and from TPXO over one week. TPXO underestimates and shifts the tides except for the meridional component at Mooring 2 location. Thus, these moorings constitute the first account of tidal currents at the PEIs, as global products such as TPXO do not fully resolve such small scale islands.

Residual velocities after tidal filtering

In this section, we use the the residual moorings velocities obtained after filtering out the tides with a Demerliac filter. Note that because the tidal signal is complex, it is important to remove it at every depths if we want to complete a proper tidal filtering. Figure 3.13 a shows the spectrum of integrated speed magnitude($\sqrt{u^2+v^2}$) before applying the Demerliac filter. Similarly to Figure 3.10 b,d, the spectrum presents several sharp peaks which correspond to the typical tide frequencies. There is also a peak of variability at around 0.003 cycle per hour which corresponds to a period of 14.6 days approximately. Considering the uncertainty in power spectra density estimate (vertical black bar), this spectral peak is not significant.

[2] `www.ifremer.fr/vacumm/library/tide.filters.html#module-vacumm.tide.filters`

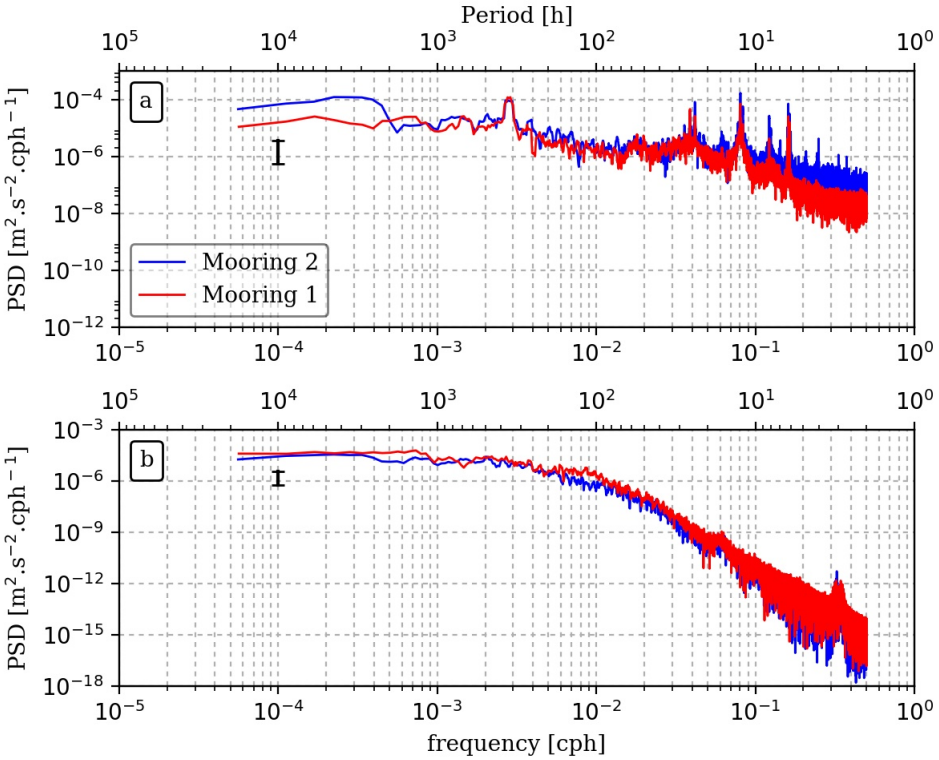

Figure 3.13: *Power Spectra Density (PSD) of quasi-barotropic speed (a) before Demerliac filter and (b) after demerliac filter. The black vertical bars show the 95% uncertainty level.*

After filtering out the tides with the Demerliac method, all these peaks have vanished which supports the fact that this low frequency variability peak is also linked to the tides. Interestingly, the filtering reveals a change of slope at 100 hour period (approximately 4 days) which suggests that this is a predominant time scale of variability.
Figure 3.14 a,b,c,d shows the zonal and meridional components of the residual velocities. If we relate this figure to Figure 3.7 b and focus on the events pointed out by arrows, we can see a possible signature of eddies moving from south west to north east and passing through the archipelago (dashed circles on Figure 3.14 a,c).

The first event (January 2015), according to Figure 3.7 b, corresponds to a cyclonic eddy passing in the vicinity of the islands. The archipelago sees, at first, positive zonal velocity and then negative zonal velocity, specific to a cyclone. For the second (April-May 2015) and third (April 2016) events, the PEIs are first rather hit by negative zonal velocity and then positive velocity, which could be the signature of anticyclones, passing in a northward direction (as confirmed by altimetry in Figure 3.7 b). Another important spike in zonal velocity is observed in September 2014 (green dashed circle on Figure 3.14 a,c), which has not been highlighted before. If we look at Figure 3.7 b at this date, a strong cyclonic eddy is recorded south of the islands, propagating towards them. Even though this eddy is still quite far of the archipelago, it seem to already affect the inter-islands velocity. The potential signature of mesoscale features we have just described is only visible in the zonal velocity component. The quasi-barotropic meridional velocity is weak (Figure 3.14 b) as well as the sub-surface meridional component of Mooring 1.

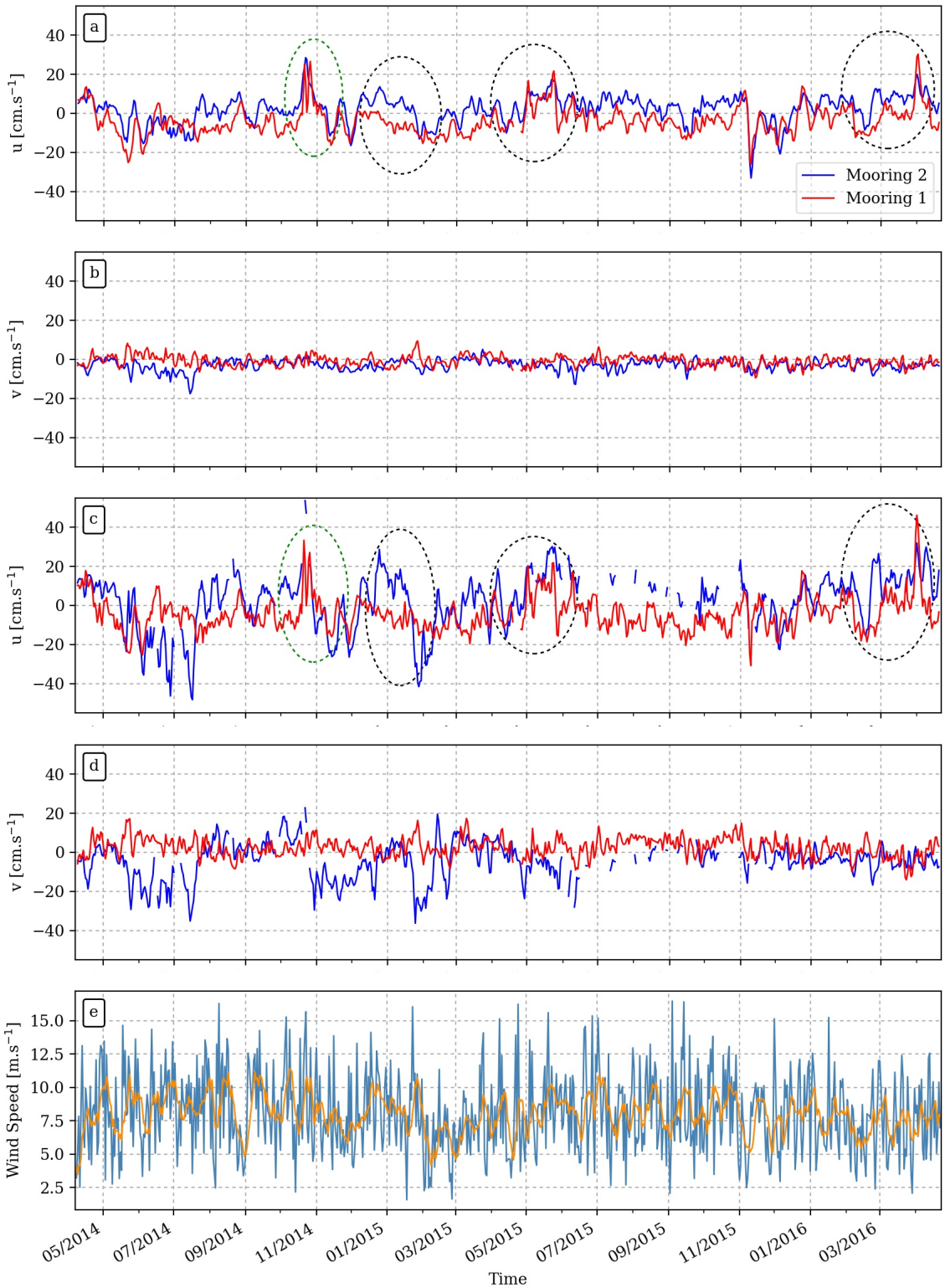

Figure 3.14: *Quasi-barotropic (a) zonal and (b) meridional residual component obtained by applying a Demerliac filter to (red) Mooring 1 and (blue) Mooring 2 data. Sub-surface (c) zonal and (d) meridional residual component. All velocity component are daily averaged. (e) Wind speed recorded at Marion Island: (blue) daily and (orange) rolling mean over one week.*

This suggests that the presence of the islands and the topography appears to lead to a signature of eddies mainly in terms of zonal velocities.
Finally, a time series of the wind recorded at Marion island[3] is computed in order to highlight a potential link between the specific events we have just mentioned and wind (Figure 3.14 e). No specific storm is evidenced with this time series, hence no connection can be established between spikes in the inter-islands currents and local winds.

Summary of Section 3.3: Local Processes

In this section, we have highlighted three important processes:

- The impact of mesoscale eddies originated upstream has on the temperature, the mixed layer and the velocities between the two islands.
- The SAF has been shown to influence inter-islands temperature: when it lies to the north, Antarctic cold waters dominate around the islands, when it shifts south of the islands, warmer waters dominate.
- Tides play an important role in the variability of the currents in the inter-islands region. They show a strong signal in the inter-islands area, which has not been documented yet.

3.4 Conclusion

The aim of this chapter has been to address PEIs both offshore and local ocean dynamics, using two moorings, CTD and altimetry data.
The positions of the SAF and the PF have been found to be highly variable at interannual and monthly time scales, moving together but with different latitudinal amplitudes. In a same year, the SAF can be observed north and south of the islands which implies different hydrodynamic conditions at the islands (Ansorge and Lutjeharms, 2002). Furthermore, the SAF and PF locations reveal a significant long-term (multidecadal) southward trend which contrasts with recent studies which agree on the long-term stability of the meridional position of the ACC fronts at global scale (Graham et al., 2012; Gille, 2014; Shao et al., 2015; Chapman, 2017). Nonetheless, Sallée et al. (2008) and Kim and Orsi (2014) have shown trends in frontal position in particular locations that significant correlation between the SAM and the positions of the fronts in the Indian and southeast Pacific Basins exist. The long-term variability of the fronts in the Southern Ocean is not very

[3]Wind data come from the South African Weather Service

clear and shows different behaviour depending on the location. Although the shift of the front of the ACC remains controversial, the result presented in this thesis is not in disagreement with the studies cited previously because this study has been performed at a very local scale.

Since 2009, satellite observations have shown that the SAF has remained mainly south of the islands which could have consequences on their hydrodynamics.

In parallel, EKE has shown also a strong interannual and intra-annual variability in our region of interest and a negative trend as well. This last result diverges from many recent studies which have shown an increase in EKE in response to the strengthening of the westerly winds in the Southern Ocean (Meredith and Hogg, 2006; Hogg et al., 2015; Patara et al., 2016). Note that these studies have been performed at the Southern Ocean scale while ours focuses on a small region of the Southern Ocean. The archipelago's environment is clearly impacted by the mesoscale features produced upstream and passing by the islands. Indeed, unusual increase (respectively decrease) of the inter-island temperature has been observed, when an anticyclonic (respectively cyclonic) eddy is moving close to the PEIs. The mixed layer around the islands is also affected by these mesoscale features. We also highlighted the influence of the position of the SAF on the inter-islands temperature. Waters are warmer when the SAF is south of the islands which likely affects the biological environment. Thus, the multidecadal southward trend mentioned earlier could have significant consequences on the ecosystems of the islands. At local scales, tides are important features of variability of the circulation between the two islands. It has been shown that while the barotropic tide has comparable impacts on the two moorings, the baroclinic component of the tide has different effects on them.

Because of the relatively coarse resolution ($\frac{1}{4}^\circ$) of altimetry data and the sparsity of observations in the region of the PEIs, we can not conclude yet on any direct link between EKE and the frontal positions. Therefore, a model is used to carry on the research. In the next two chapters, we first characterise the mesoscale features of the model and then investigate on the potential impact of long-term SAF variations on mesoscale activity at the islands.

4 What are the processes at play in eddies formation at the South West Indian Ridge?

Contents

4.1 Introduction

The PEIs region is characterized by an enhanced presence of eddies, not because of the interaction of the current with the islands themselves , as it has been inferred previously (Perissinotto et al., 2000; Pakhomov et al., 2000; Ansorge and Lutjeharms, 2000) but because they lie downstream of the SWIR, a region of high mesoscale variability (Ansorge and Lutjeharms, 2003). The eddies originate from the ridge, roughly at 50°S-30°E, corresponding to the ABFZ. Both cyclonic and anticyclonic eddies move through the ABFZ and then most of them go northeastwards, following the eastern flank of the ridge, while others seem unaffected by the bathymetry. Craneguy and Park (1999) have suggested that eddies behaviour is dependant on bottom velocities: if bottom velocities exceed a certain value, the topographic control prevails over the β effect and forces the eddies to advect along the SWIR. On the other hand, when bottom velocities are weak, the topographic control is not strong enough against the β effect and allows formation of meanders. Then, some eddies can move more freely eastwards without being constrain by the bathymetry. Although eddies can follow different tracks, their propagation appears to be restricted to the channel separating the Conrad Rise from the Del Caño Rise forming an eddy corridor (Ansorge and Lutjeharms, 2003; Ansorge and Lutjeharms, 2005). Moreover, Ansorge et al. (2014a) depicted the southern extension of the EKE pattern (see Figure 3.5) as a southward eddy corridor acting as a conduit of warm core eddies, as first highlighted by Gouretski and Danilov (1994).

Based on hydrographic data collected during research cruises, the characteristics of the mesoscale features have been widely studied in this area. Ansorge and Lutjeharms (2003), using data from the *Marion Island Oceanographic Survey II* (MIOS-II) undertaken in April-May 1997, described the water masses properties carried by some eddies that passed the islands. They found that the water masses indicated that cyclonic eddies came from south or originated close to the PF whereas anticyclonic eddies came from the subantarctic region. Durgadoo et al. (2010) provide a review of eddies characteristics resulting from the *Dynamics of Eddy Impact on Marion's ECosystem* (DEIMEC) programme, carried out between 2002 and 2005, and aimed to understand and characterize these eddies. The DEIMEC programme led to four surveys, undertaken each time in autumn (April-May). They observed three intense well-defined eddies per year in the vicinity of PEIs. Observations have shown that these eddies reach depths of at least 1000 m, have a diameter of 100-300 km, advection speeds of the order of a few kilometres per day and longevities of 7-11 months. Additionally to the programs aforementioned, more surveys have been carried out. Unfortunately, despite all samplings, the space and time coverage remains very limited. Hence, it is necessary to use a model to get a better understanding. Durgadoo et al. (2010) used the Ocean Circulation and Climate Advanced Modelling $\frac{1}{12}^{\circ}$ model (OCCAM) to investigate the decay of cold eddies at the SWIR. From 10 years of

OCCAM model outputs, they managed to track 20 cold eddies. They found that after reaching their peak intensity, eddies dissipate within approximately 3 months. The decay of eddies is generally associated to a decrease in their SSH and rotation speed and also to a change in their water properties (temperature, salt).
The goal of this chapter is to investigate on the processes at play in the eddy formation at the ridge. We use a 10-years simulation from an idealised configuration of the model CROCO with a $\frac{1}{12}^\circ$ resolution nesting (described in Chapter 2). At first, we study the mean EKE obtained with the model and describe the eddies properties. Subsequently, energy conversion terms are computed in order to study the nature of the instabilities responsible of the eddy generation. Finally, we explore the potential origin of the energy required to generate the mesoscale features.

4.2 Eddy Kinetic Energy in the model

As mentioned before the PEIs are a region of high mesoscale variability whose features are generated at the ABFZ. In this section, we present the EKE generated by a 10-years simulation. We use the CROCO model with a nesting at $\frac{1}{12}^\circ$ resolution. We remind here that the experiment is made in an idealised context. The model is forced with annual mean fields which implies neither seasonal or interannual variability.
Figure 4.1 shows a map of EKE averaged over the last 8 years of this simulation. Compared to EKE from Aviso (see Figure 3.5), the model produces less EKE than observed and the peculiar "horseshoe" pattern observed from satellite is not fully represented by the model. Two cores of high energy (500-600 $cm^2.s^{-2}$) are seen on each side of the south part of the ridge.

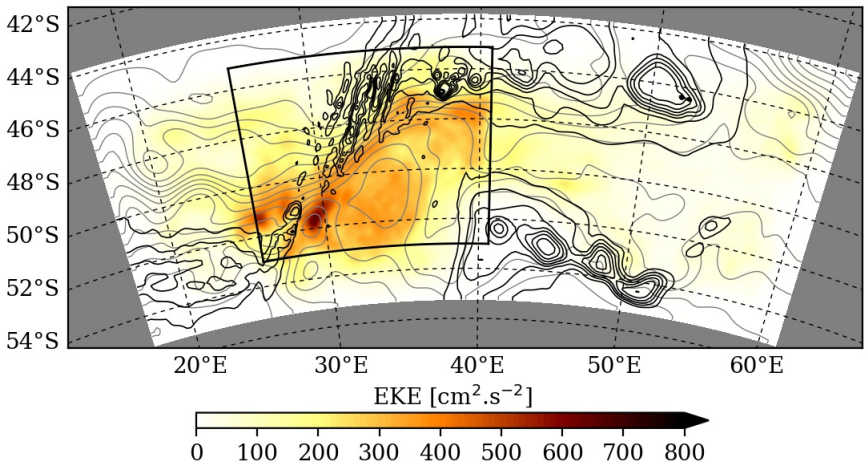

Figure 4.1: *Mean surface EKE of the last 8 years of the CROCO simulation. The grey lines are the streamlines and the black lines represent the bathymetry in the model. The black frame defines the child box.*

Nonetheless, the mean circulation is well reproduced by the model. Indeed, upstream the ridge, ACC structure is zonal while after the fracture zone the streamlines meander

and flow along the bathymetry (grey lines on Figure 4.1). That means that the model recreates the strong control exerted by the bottom topography on the circulation in this region of the ACC. Moreover, the eastern part of the EKE pattern is also represented with eddies following the eastern flank of the ridge and reaching the islands, which is the scope of this work.
Therefore, the simplified configuration we set up fulfils our purposes. It reproduces the key processes we interested in, namely the generation of eddies at the ridge and their interaction with the Prince Edward Islands.

4.3 Description of the eddies

In this section, the eddies are tracked in the model and their generation site and trajectory are compared with satellite data. Then, the physical properties of the mesoscale features are studied as well as their vertical structure.

4.3.1 Eddy detection and tracking method

To detect and track eddies generated in the region, an automated eddy tracking scheme is used (Halo et al., 2014). The algorithm detects the geostrophic eddies from sea surface height, based on geometric criteria and and physical properties of the flow. It combines the largest closed contours in SSH and the negative values of Okubo-Weiss parameter (W, Okubo, 1970; Weiss, 1991), to identify and track the mesoscale features. The Okubo-Weiss parameter allows to distinguish strain-dominated area (W>0) from the vorticity-dominated one (W<0). It is defined as:

$$W = s_n^2 + s_s^2 - \omega^2$$

where the normal strain component s_n, the shear strain component s_s and the vorticity ω are expressed as follow:

$$s_n = \frac{\partial u}{\partial x} - \frac{\partial v}{\partial y}, \quad s_s = \frac{\partial v}{\partial x} + \frac{\partial u}{\partial y}, \quad \omega = \frac{\partial v}{\partial x} - \frac{\partial u}{\partial y}$$

Eddies are regions of negative W parameter, where the vorticity outweighs the strain-component.
Combined with the Okubo-Weiss parameter , geometric criteria are used to select the eddies. The interval between SSH contours must be specified and should be around the precision of altimetry. We set it at 2 cm. Also, in order to prevent taking an ocean gyre as a giant eddy, a maximum eddy radius is chosen at 300 km.
Once the eddy has been detected, it can be tracked from one time step to the next by finding the closest eddy in term of distance, radius and vorticity (Penven et al., 2005).

4.3.2 Eddy generation and trajectory

The aforementioned scheme is used in order to study eddy characteristics and track them in the model and Aviso. Eddies are tracked for the last 8 years of the 10-years simulation. To be consistent with the model outputs, eddies are tracked for 8 years as well, over the 2007-2014 period, in Aviso. Only eddies with lifespans exceeding 30 days and a radius superior to 30 km are considered. They represent 13% and 17% of the total number of eddies tracked in Aviso and CROCO respectively.

In Figure 4.2, we show the occurence of eddies in Aviso and CROCO computed within each 0.5°×0.5° grid box. In Aviso as well as in the model, increased eddy activity occurs right downstream the fracture zone, between the SWIR and the Conrad Rise.

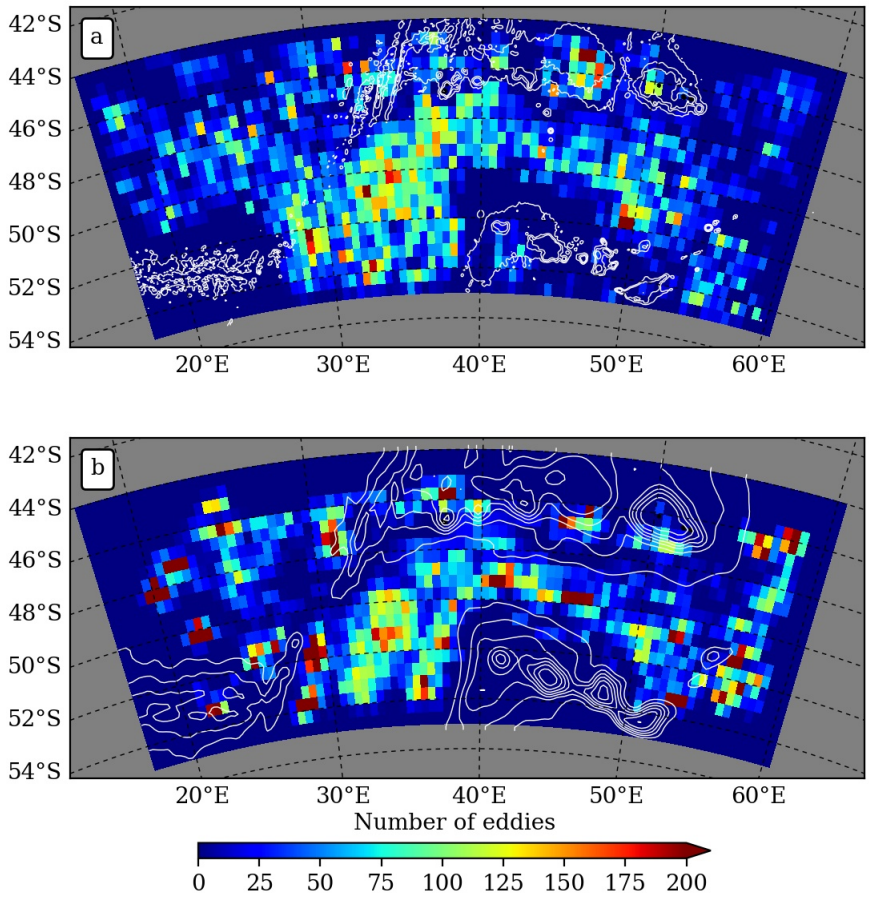

Figure 4.2: *Occurence of tracked eddies with longevity exceeding 30 days and a radius superior at 30 km, in a 0.5°×0.5° square box grid size for (a) Aviso and (b) CROCO.*

It extends from 54°S, along the eastern flank of the SWIR, until 45°S approximately. This is the result of the generation of both cyclones and anticyclones, which propagate along the bathymetry until 40°E (Figure 4.3). East of 40°E, a corridor of high concentration of eddies is observed (Figure 4.2), restricted to the deep channel separating the Conrad Rise from the Del Caño Rise and the Crozet Plateau. In this case, it is also a contribution of both cyclones and anticyclones (Figure 4.3).

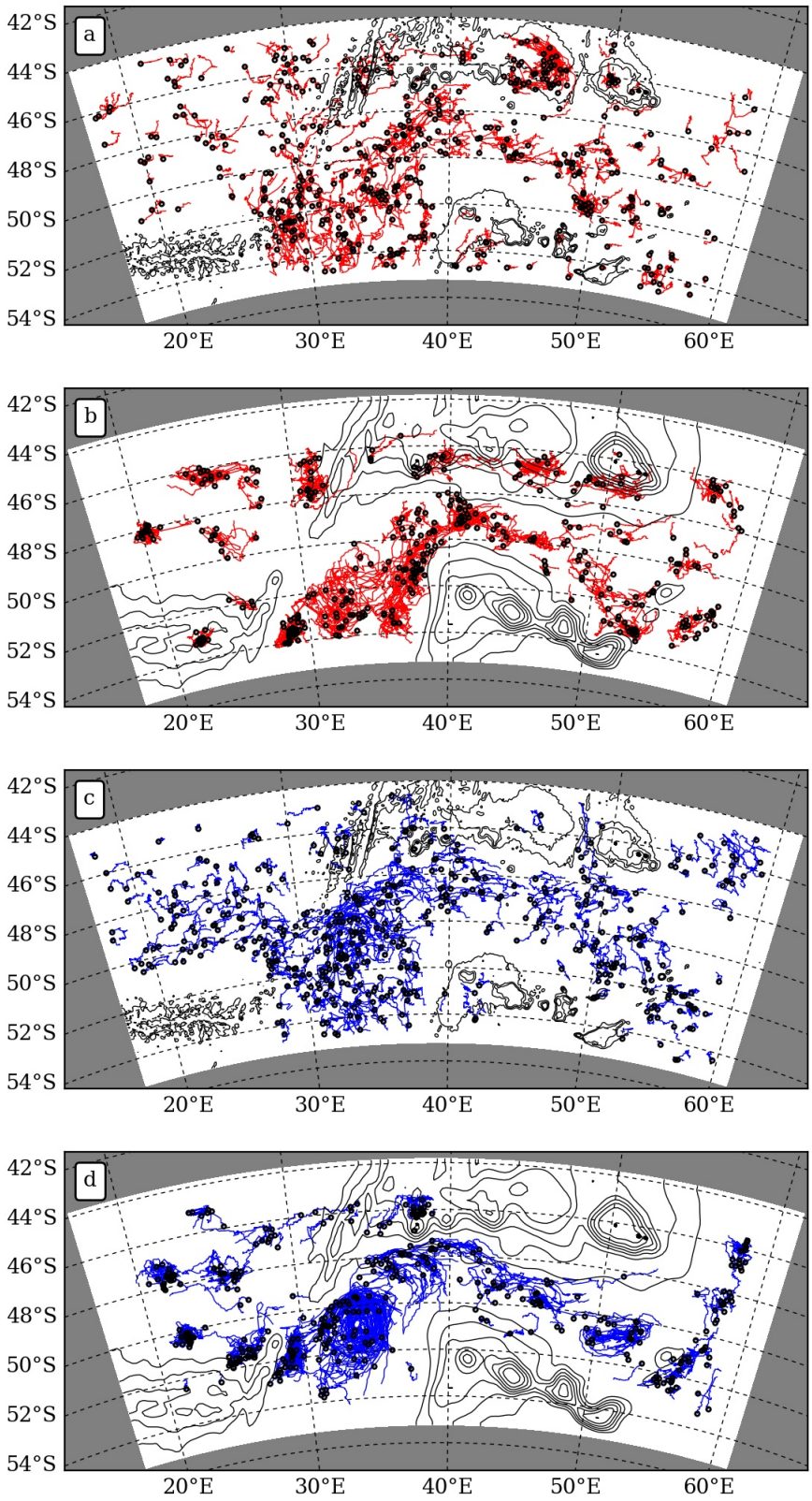

Figure 4.3: *The generation sites, represented as black dots, and trajectories of (red) anti-cyclonic and (blue) cyclonic eddies in (a,c) Aviso and (b,d) in the model. Only eddies with a lifespan exceeding 30 days and a radius superior at 30 km are considered.*

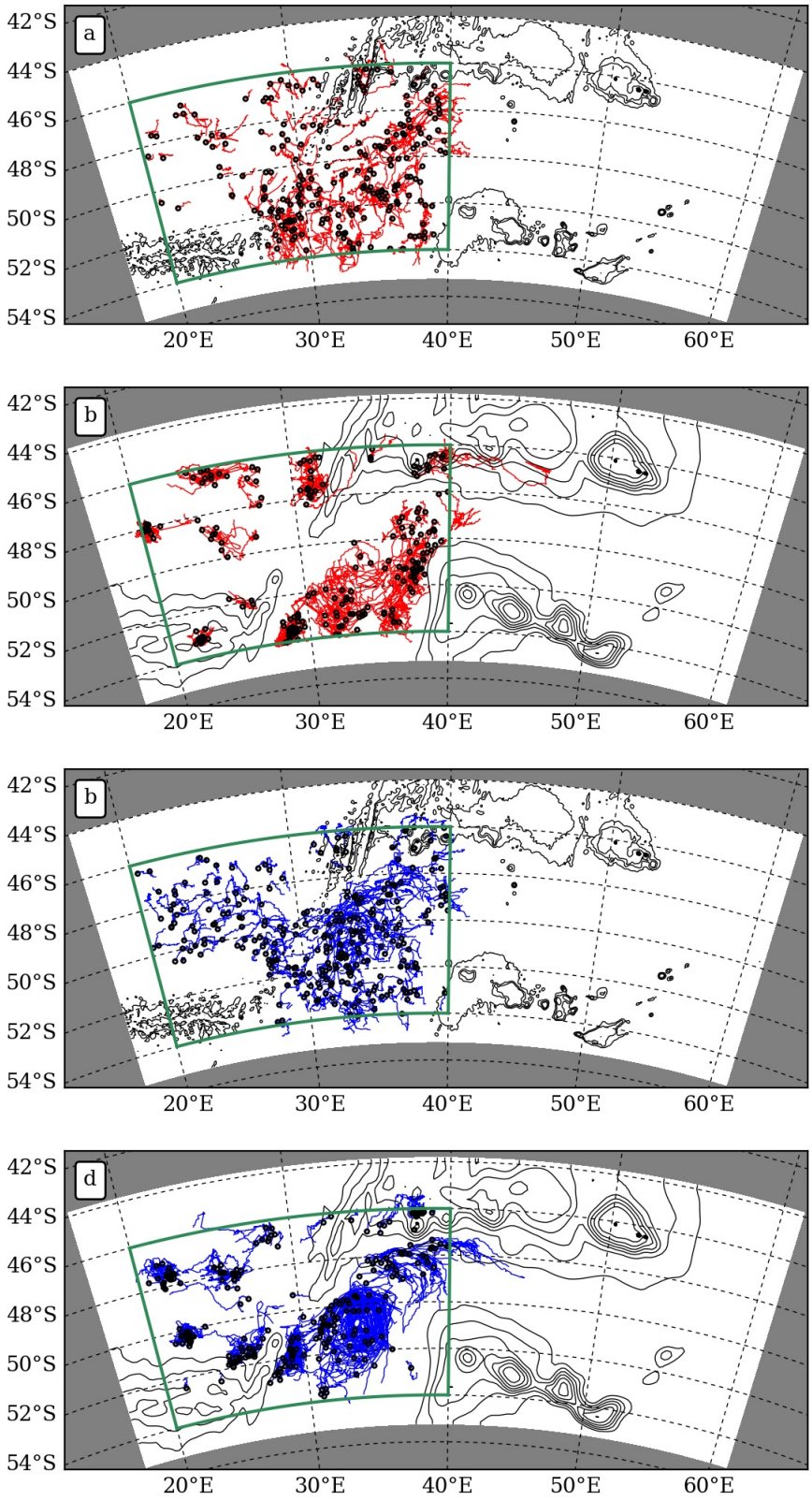

Figure 4.4: *The generation sites, represented as black dots, and trajectories of (red) anti-cyclonic and (blue) cyclonic eddies in (a,c) Aviso and (b,d) in the model. Only eddies generated in the green frame with a lifespan exceeding 30 days and a radius superior at 30 km are considered.*

Upstream the ridge (west of 30°E) eddy activity is also present. In Aviso, it seems that cyclonic eddies are the main contributors to this activity (Figure 4.3 a,c) whereas in the model, both cyclones and anticyclones contribute to it (Figure 4.3 b,d). Moreover, we observe additional areas of high eddy occurrence such as above the Del Caño Rise in Aviso (Figure 4.2 a), caused by anticyclones generation (Figure 4.3 a). CROCO displays a band of enhanced mesoscale activity at 46°S-47°S, extanding from 30°E to the Crozet Plateau at 50°E (Figure 4.2 b). It can be mainly attributed to anticyclonic eddies generation and their propagation (Figure 4.3 b). We note that some eddies are going counter-current, both in the model and altimetry. We discuss this at the end of this section.

In spite of some discrepancies, CROCO and Aviso agree quite well on the eddy generation locations and trajectories. They show a common preferential area of formation between the ABFZ and the Conrad Rise. The eastward eddy corridor (region immediately downstream of the SWIR and extending to the PEIs vicinity) clearly visible in Aviso and highlighted previously by Ansorge and Lutjeharms (2003) and Ansorge and Lutjeharms (2005), is well represented in the model. Still, the pathways of anticyclonic and cyclonic eddies in the model are less isotropic than in the observations, presumably due to a reduced turbulence in the model (cf Figure 4.1). Also there is no eddy formation at the location of the main current in the model, where streamlines are close to each other upstream the SWIR, which is presumably due to the fact that intense transports (which may be overestimated in the model) prevent the development of instabilities (Capet et al., 2002).

The mesoscale features impacting the islands are known to be generated at the SWIR. Therefore, in the subsequent analyses, we focus on eddies generated within the box showed on Figure 4.4 (20°E-40°E and 54°S-46°S).

Rossby Wave Speed

As aforementioned, we observe some eddies going westwards, which is quite unusual in this part of the ocean (see figure 4b in Chelton et al., 2011). Indeed, as the ACC flows eastwards, most of the eddies are transported eastwards. It is well known that eddy drift is controlled by several processes as Rossby wave activity, advection by the mean currents or eddy interactions (Carton, 2001) for instance. Here, we investigate this phenomenon by computing, in the case of the long-wave approximation, the phase velocity of Rossby waves for the first baroclinic mode in the presence of a zonal current:

$$c = u - \frac{\beta c_e^2}{f^2}$$

where c is the zonal phase speed of the Rossby wave, u is the zonal mean flow, β is the Beta parameter, c_e is the first mode gravity wave speed and f the Coriolis parameter. The first ocean dynamic vertical mode is calculated at each grid point given a profile of

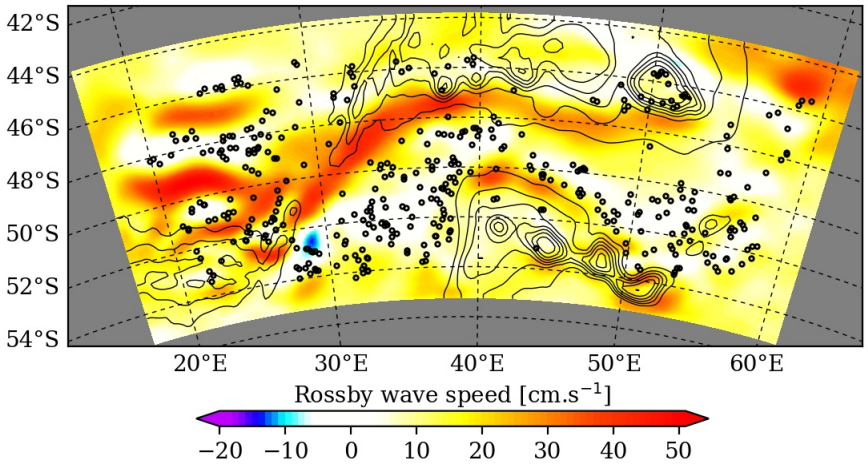

Figure 4.5: *Phase speed of Rossby waves for the first baroclinic mode. The generation sites of the eddies (cyclones and anticyclones) are represented as black dots.*

Brunt-Väisälä frequencies.

Figure 4.5 illustrates the generation sites of the eddies travelling westwards, overlaid to the Rossby wave speed in the model. The eddy generation location concurs with areas where the Rossby waves are stationary or fast enough so that eddies propagate westwards, against the ACC. This analysis highlights the fact that zonal speed is not homogeneous in this region on the ocean and this affects eddy propagation and pathways.

4.3.3 Eddy characteristics

We perform a statistical analysis on 393 eddies (202 cyclones and 191 anticyclones) from CROCO and 466 eddies (229 cyclones and 237 anticyclones) from Aviso. All the eddies are generated in the box shown on Figure 4.4, with lifespans longer than 30 days and a radius superior at 30 km. Afterwards, we present the vertical structure of a cyclonic eddy and its counterpart, in terms of temperature, salinity and meridional speed.

Eddy diameter and Amplitude

The averaged diameter of both cyclonic and anticyclonic eddies are very similar in Aviso and CROCO (see Table 4.1), although eddies from the model are slightly bigger. More than 60% and 80% of the eddies in the model and in the altimetry data respectively, have a diameter in the range 80-110 km. Less than 10% exceed 110 km in Aviso. In-situ observations that provide informations about eddies in the region of the PEIs are summarized by Durgadoo et al. (2010). They found a typical diameter in the order of 100 km. Durgadoo et al. (2011) based their analysis on a model[1] and found a cold eddy of 110 km diameter. Our results are in agreement with the observations and the modelling study performed by Durgadoo et al. (2011).

[1]The Ocean Circulation and Climate Advanced Modelling 1/12°model

Concerning the eddy amplitude, Table 4.1 shows an averaged amplitude similar for both type of eddies in either of the datasets. Moreover, the altimetry histogram (Figure 4.6 c) and the model histogram (Figure 4.6 d) present the same distribution of eddy amplitudes. The majority of Aviso eddies (more than 60%) have their amplitude spreading from 6 to 12 cm. In the model, more than 50% and 60% of anticyclone and cyclone amplitudes are in the 6-12 cm range.

Eastward Propagation Speed

The mean propagation speed of cyclones and anticyclones in the model is 7.2 km.day^{-1} and 6.8 km.day^{-1} respectively. In Aviso, the eddies travel slower (see Table 4.1). Figure 4.6 e shows that more than 90% of the eddies tracked in Aviso travel at a speed in the range 2-6 km.day^{-1}. In the model, the majority of eddies (more than 80% of the cyclones and anticyclones) have their speed ranging from 4 to 10 km.day^{-1} (Figure 4.6 e). Durgadoo et al. (2010) found the speeds to be of the order of few kilometres per day and the simulation presented by Durgadoo et al. (2011) generated eddies of advection speeds of 5$\pm$2 km.day^{-1}.

Lifespan

Eddies in the model last longer, about 10 days more in average, than the ones tracked by altimetry (Table 4.1). Cyclonic and anticyclonic eddies have equivalent averaged longevity in the two datasets. In Figure 4.7 a,b, we highlight that the 6-8 weeks (1-2 months) lifetimes are the most frequent in both Aviso and CROCO. Durgadoo et al. (2010) mention longevities of 7-11 months (30-47 weeks) which are definitely longer than the averaged lifespans obtained by altimetry and the model. In Figure 4.7 a,b, we show that eddies exceeding 20 weeks are rare. Less than 3% of anticyclones and cyclones in the model have lifespans superior at 30 weeks and less than 2% of the eddies (cyclones and anticyclones) exceed 30 weeks. Besides, Durgadoo et al. (2011) analysed 20 cold eddies in their model and found that 65% of then lasted on average of 4 months which is twice as big as the lifespan we found in altimetry data and the model. This discrepancy between our results and observations can be explained by the fact that Durgadoo et al. (2010) based is analysis on 2 warm and 2 cold eddies only whereas in our study we consider more than 200 eddies. In the same way, Durgadoo et al. (2011) studied only 20 cyclonic eddies.

Propagation Distance

The averaged eastward distance travelled by the eddies in CROCO is almost twice as big as the one in Aviso (Table 4.1). More than 70% of the eddies in the altimeter data travel over a distance in the range 100-300 km (Figure 4.7 c). In Figure 4.7 d, we show that, in

the model, more than 70% of the eddies travel between 100 and 700 km. Less than 10% of the mesoscale features, in either of the datasets, propagate beyond 1000 km.

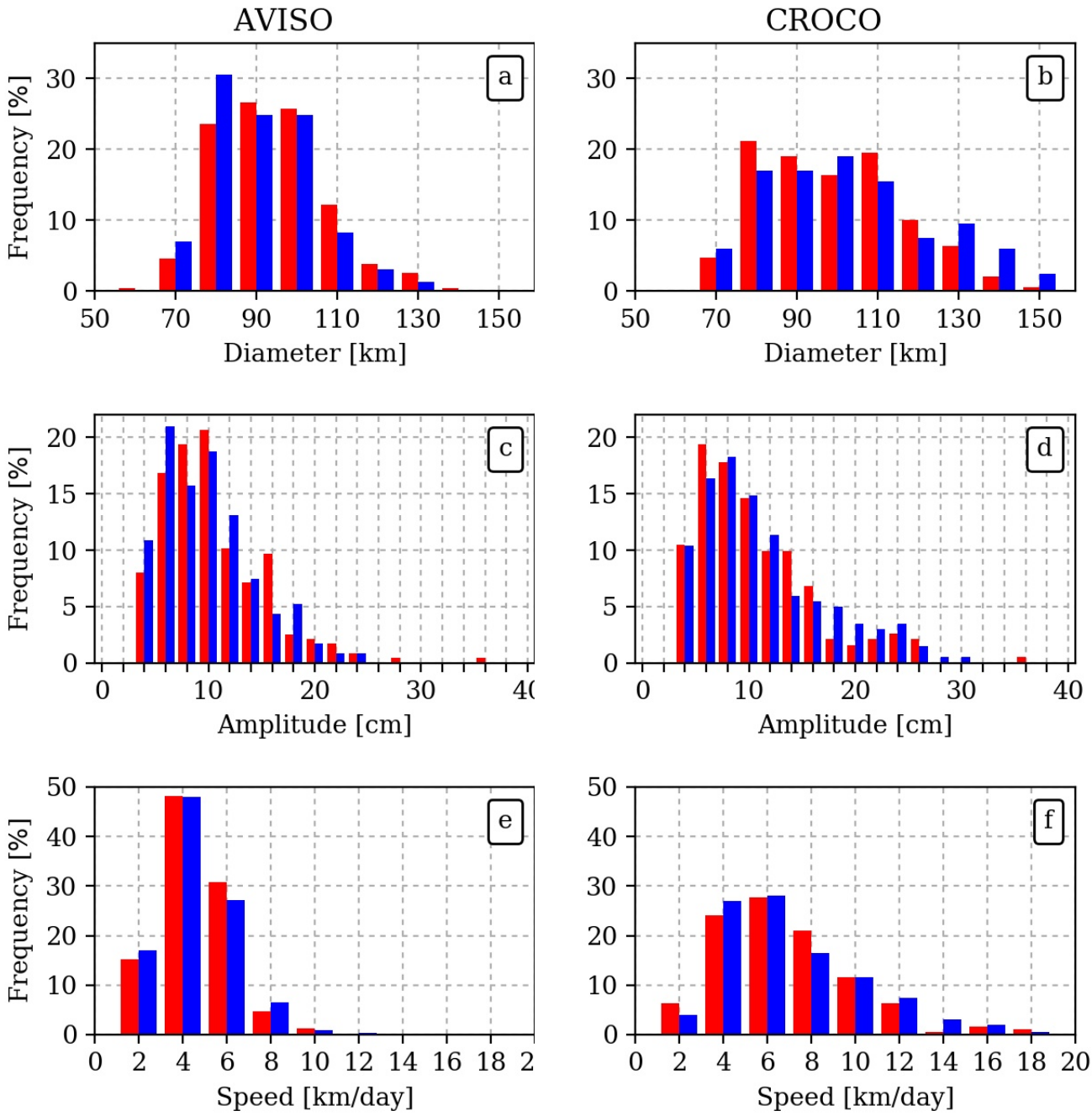

Figure 4.6: *Histogram of (a,b) eddy diameter, (c,d) eddy amplitude and (e,f) speed. The left panels are the histograms of eddies tracked in Aviso and the right panels are the ones for eddies in the model. In all panels, blue is for cyclones and red is for anticyclones.*

Eddy surface kinetic energy

In Table 4.1, we show that the model produces, in average, less energetic eddies than the features tracked altimeter. In the model as well as in Aviso, surface energy of cyclonic and anticyclonic eddies is very similar. CROCO shows that about 40% of the eddies have an energy of about 200 $cm^2.s^{-2}$ and 70% of the eddy energy does not exceed 500 $cm^2.s^{-2}$ (Figure 4.7 f).

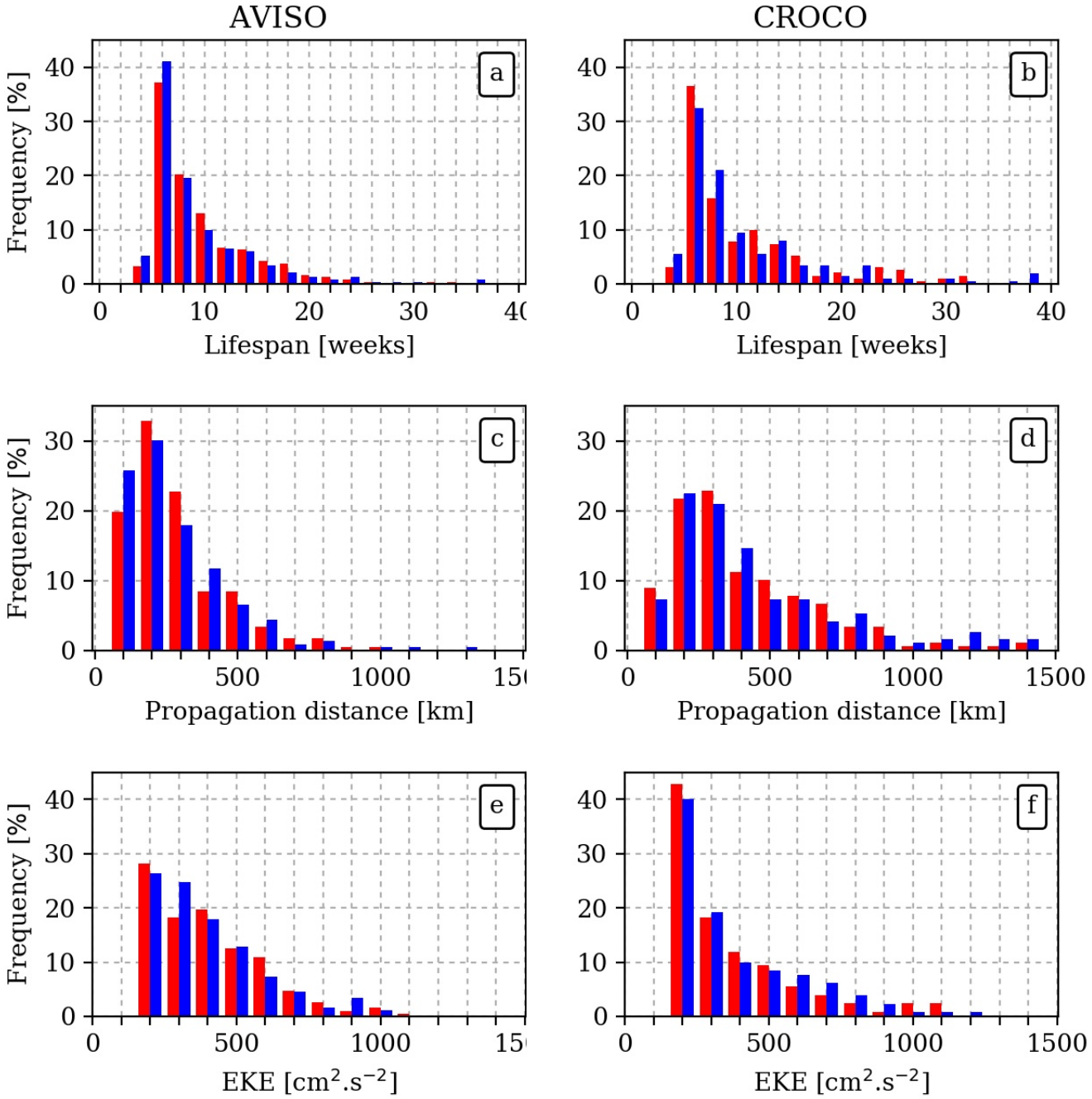

Figure 4.7: *Histogram of (a,b) eddy lifespan, (c,d) propagation distance and (e,f) Eddy Kinetic Energy. The left panels are the histograms of eddies tracked in Aviso and the right panels are the ones for eddies in the model. In all panels, blue is for cyclones and red is for anticyclones.*

	N/year	Lifetime [day]	Amplitude [cm]	Diameter [km]	Propagation speed [km.day^{-1}]	EKE [cm^2.s^{-2}]	Distance [km]
Aviso							
Cyclones	28 ± 6	61 ± 36	10 ± 4.4	91 ± 12	4.6 ± 1.6	325 ± 208	279 ± 182
Anticyclones	29 ± 8	63 ± 34	10.5 ± 4.7	94 ± 13	4.5 ± 1.5	351 ± 227	282 ± 167
CROCO							
Cyclones	25 ± 6	76 ± 43	11 ± 5	103 ± 21.1	7.2 ± 3.4	287 ± 143	548 ± 296
Anticyclones	24 ± 3	73 ± 50	10 ± 5	100 ± 18.5	6.8 ± 2.9	293 ± 169	503 ± 227

Table 4.1: *Mean properties of the eddies generated in the area shown on Figure 4.4 (green frame) and tracked in Aviso and in the model. The eddies are tracked over the 8 last years of the simulation and from 2007 to 2014 in Aviso. N/year is the number of eddies per year and EKE is the Eddy Kinetic Energy integrated over the eddy area.*

4.3.4 Vertical Structure

Vertical temperature, salinity and velocity

In order to illustrate the vertical structure of eddies produced by the model, two vertical sections of a cold and warm eddy, typical of the region, are shown on Figure 4.8 and Figure 4.9. These figures display the vertical temperature, salinity and meridional velocity. The cyclonic eddy, shown on Figure 4.8, is centered at 50°S-35.5°E. It has a diameter of approximately 130 km which is quite big considering the eddy diameter distribution plotted on Figure 4.6 b. There is a temperature minimum core (<1.6°C) isolated from the surface by a strong thermocline, lying between 100 m and 200 m. The eddy is clearly demarcated by the 2°C isotherm until 1000 m. In the upper layer, a maximum of 4.6°C is observed. A similar eddy has been observed and described by Swart et al. (2008). The cyclonic signature in salinity (Figure 4.8 b) is visible from 300 m, where the isohalines start upwelling, making the eddy more saline than its surrounding environment. The saline signature of the eddy extends until about 1000 m. Meridional velocity presents the typical dipolar structure with a surface velocity at the edge of 0.4 m.s^{-1} (Figure 4.8 c). Southward velocity decreases to 0.2 m.s^{-1} by 2500 m. Northward velocity displays a value of 0.25 m.s^{-1} at 2500 m. These sections show the deep signature of the cyclonic eddy in the region.

In Figure 4.9, vertical sections of temperature, salinity and meridional velocity across an anticyclonic eddy, centered at 50°S-31°E, are illustrated. This eddy presents a diameter of about 250 km which is similar to the warm eddy described by Ansorge and Lutjeharms (2005). Figure 4.9 a gives the temperature and shows the characteristic deepening of the isotherms in the core of the eddies. In the top 800 m, temperatures range from 2.4°C up to 4.4°C. It is slightly colder than the one observed by Ansorge and Lutjeharms (2005). Beneath 300 m, the anticyclonic

eddy marked its presence by downwelling the isohalines with salinity ranging from 34.3 to

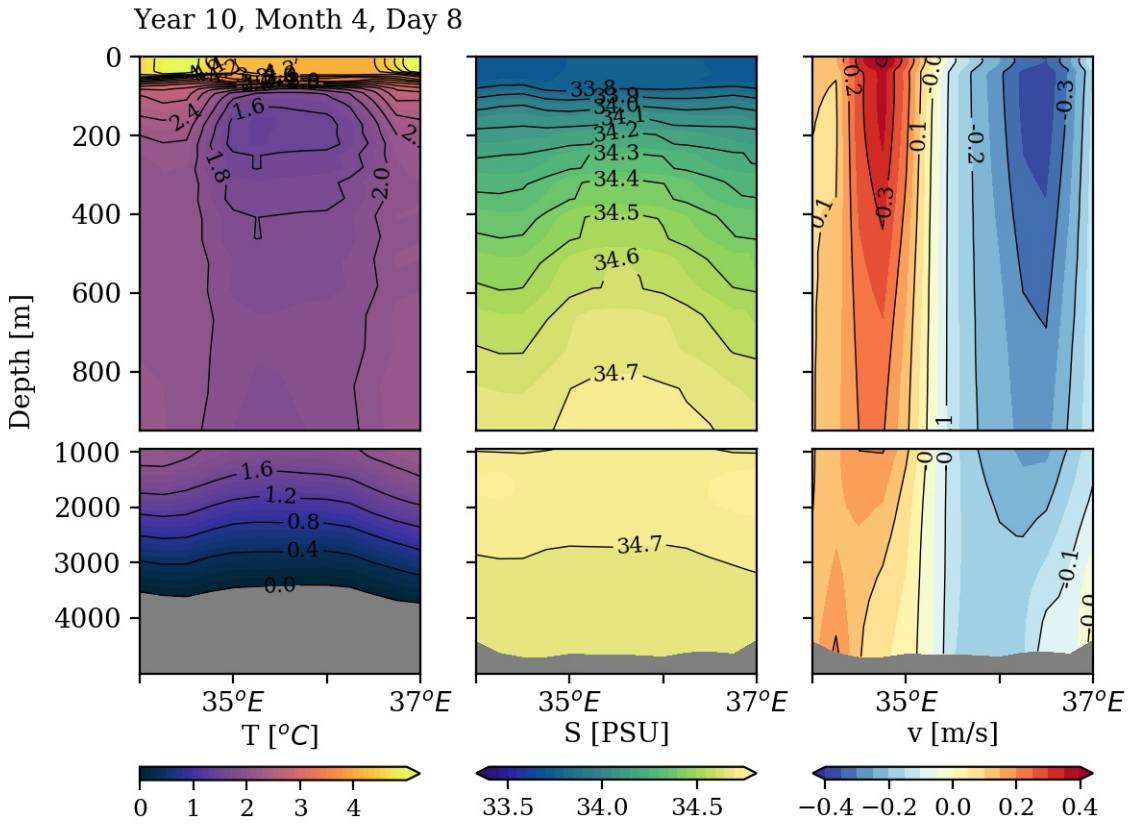

Figure 4.8: *Full depth zonal sections along 50°S through a cyclonic eddy. It shows the eddy vertical structure in term of (a) temperature (b) salinity and (c) meridional velocity.*

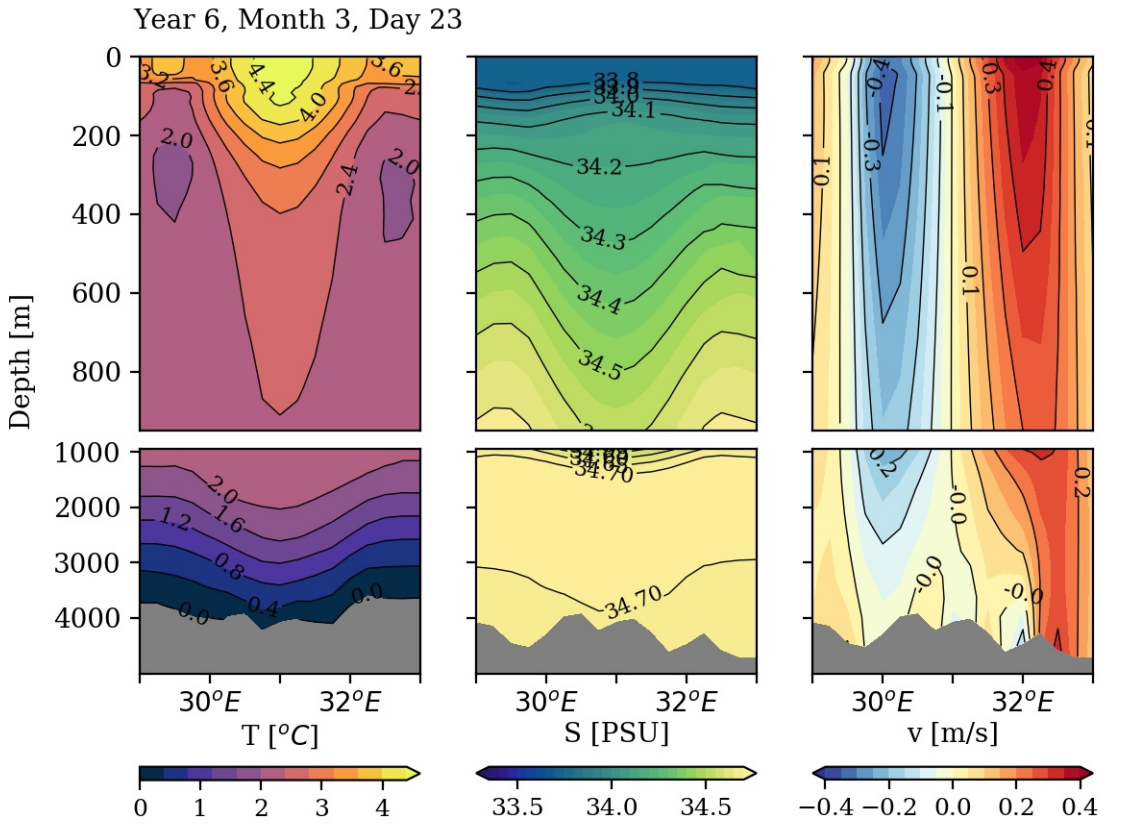

Figure 4.9: *Snapshot of a full depth zonal sections along 50°S through an anticyclonic eddy. It shows the eddy vertical structure in term of (a) temperature (b) salinity and (c) meridional velocity.*

34.6. As it has been observed for the cyclonic section, meridional velocity sections shows a strong eddy signal (Figure 4.9 c). Maximum northward velocities of 0.35 m.s^{-1} are found at the surface and decrease to 0.25 m.s^{-1} by 2000 m. Southward velocity ranges from 0.4 m.s^{-1} near by the surface to 0.05 m.s^{-1} at the bottom.
These two sections highlight the clear deep vertical signature characteristic of the eddies originated in this region.

Eddy Available Potential Energy

To go further on the study of the vertical structure of the eddies, we investigate on Eddy Available Potential Energy (EAPE). EAPE is used to measure the energy stored in isopycnal displacement and thus is a good proxy to estimate the mesoscale turbulence intensity in the ocean interior (Roullet et al., 2014). It is defined as follows:

$$EAPE = -\frac{g}{2\rho_0}\overline{\zeta'\rho'}$$

where ζ' is the vertical isopycnal displacement, ρ' the density anomaly associated with the displacement, and the bar refers to long-term time averaging. It is important to highlight that EAPE contains the mesoscale and submesoscale turbulence but also the energy induced by internal waves.

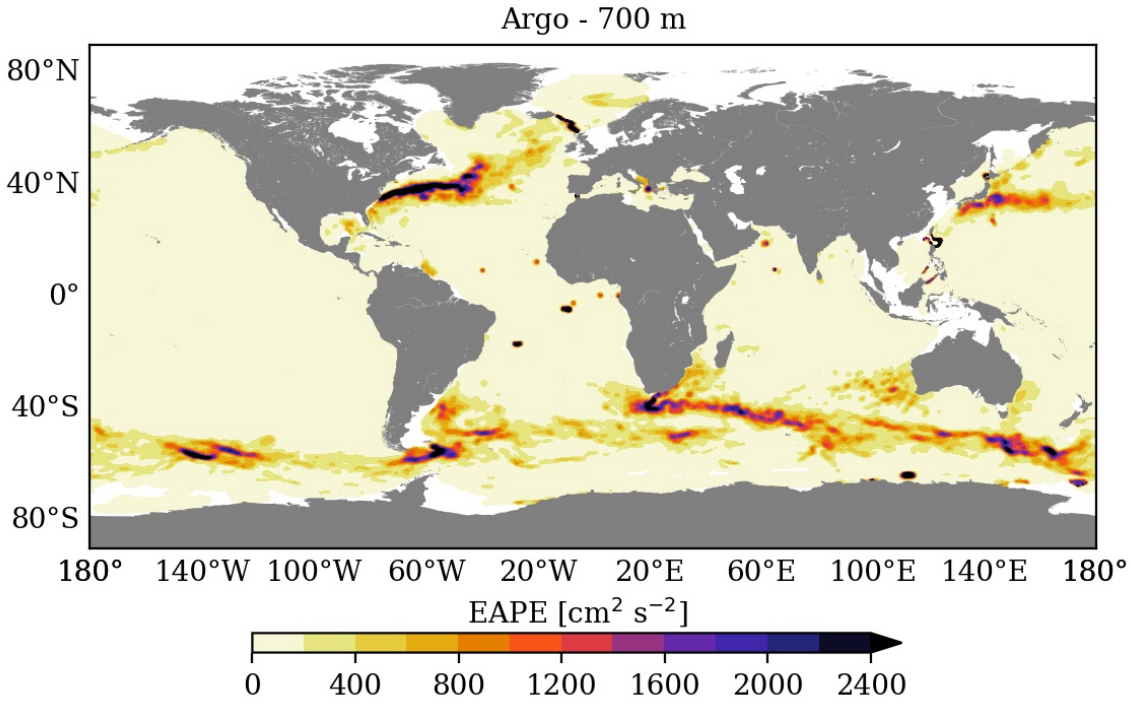

Figure 4.10: *EAPE at 700 m derived from Argo floats (data set described in Roullet et al., 2014).*

In Figure 4.10, we present a global map of EAPE at 700 m, derived from Argo floats (data set described in Roullet et al., 2014). It reveals that intense eddy activity occurs mainly in the western boundary currents and in the Southern Ocean. At 30°E-50°S, the ABFZ, a

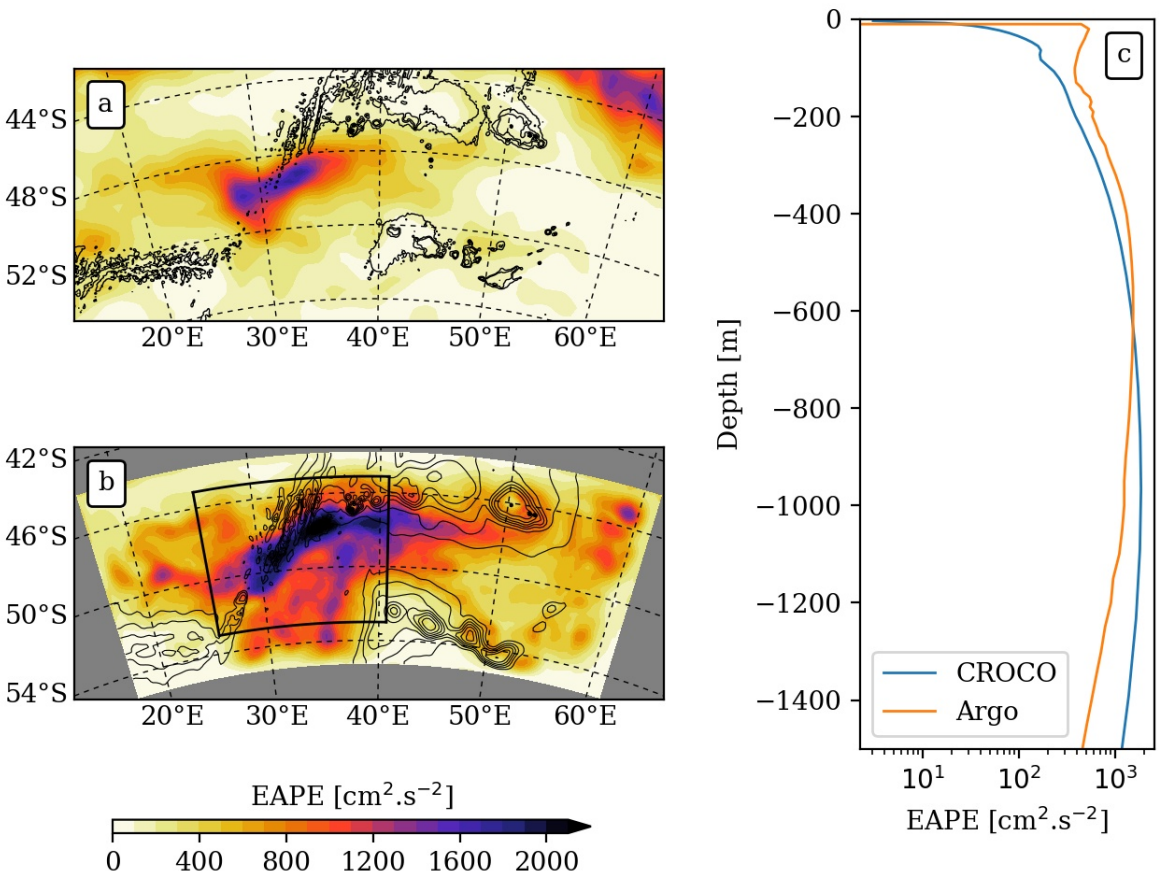

Figure 4.11: *EAPE at 700 m in (a) Argo and (b) CROCO. (c) is the EAPE profil at the location 30°E - 50°S*

local maximum in EAPE is observed. In Figure 4.11 a we show a zoom of this region and it displays EAPE at 700m for Argo data. EAPE signal is well collocated with the strong signal of EKE derived from Aviso sea level anomalies (see Chapter 3) and reproduces the same peculiar "horseshoe" pattern. This suggests that mesoscale eddies observed in Aviso (at the surface) have a deep reaching influence in this region, as diagnosed in the model. EAPE reaches values of 1500 $cm^2.s^{-2}$.

Applying the same technique as in Roullet et al., 2014, we compute EAPE in the model for the last 8 years of simulation. In Figure 4.11 c, we show EAPE profile at 30°E-50°S in the model and Argo. The EAPE maximum in Argo is reached at 700 m whereas in CROCO, the maximum is deeper, around 900 m. According to Roullet et al., 2014, this maximum suggests a local energy source and is the signature of baroclinic instabilities. Figure 4.11 b shows a map of EAPE at 700 m produced by the model. A zone of high EAPE is observed along the eastern flank of the SWIR (from 30°E to 45°E) where the values of energy exceeds 2000 $cm^2.s^{-2}$. The model produces larger EAPE than seen from Argo data (Figure 4.11 a). Furthermore, contrary to Argo-derived EAPE which diplays a similar pattern to EKE from Aviso, EAPE and EKE from CROCO model present different patterns (see Figure 4.1). Because EAPE contains the mesoscale turbulence and the turbulence induced by internal waves as well, the pattern bias between EKE and

EAPE in the model could be related to the fact EAPE is not efficiently converted to EKE and then our model might also contain internal wave activity.

4.4 Mechanisms of eddy formation

In this section, we investigate the nature of mechanisms at play in eddy formation, producing the EKE pattern seen in our simulation (refer to Figure 4.1). We begin with a description of the energy conversion terms (KmKe and PeKe specifically) and then we analyse these mean terms for our region.

4.4.1 Energy conversion terms

Volume-integrated potential and kinetic energy budgets provide informations about the source of instabilities responsible for energy transfers between the mean flow and the mesoscale features. We focus on two specific energy conversion terms which we compute following Marchesiello et al. (2003):

$$KmKe = -\left[\overline{u'u'}\frac{\partial \overline{u}}{\partial x} + \overline{u'v'}\left(\frac{\partial \overline{u}}{\partial y} + \frac{\partial \overline{v}}{\partial x}\right) + \overline{v'v'}\frac{\partial \overline{v}}{\partial y}\right]$$

$$PeKe = -\frac{g}{\rho_0}(\overline{w'\rho'})$$

where (u',v',w') and ($\overline{u}$,$\overline{v}$,$\overline{v}$) are the turbulent and mean velocity components respectively, x and y are the zonal and meridional directions, g is the acceleration due to gravity, ρ' is fluctuation of seawater density and ρ_0 is the reference seawater density.
KmKe describes the energy conversion from the kinetic energy of the mean flow to eddy kinetic energy produced by barotropic instability arising from vertical and horizontal shears. In case this conversion term is positive, the mean kinetic energy of the flow is converted to eddy kinetic energy. The energy transfer from eddy potential energy to eddy kinetic energy, referred as PeKe, is a signature of baroclinic instabilities through buoyancy forcing. By flattening out the isopycnals, baroclinic instabilities decrease the potential energy. PeKe is positive when eddy potential energy is converted into eddy kinetic energy. As we said before we will focus on KmKe and PeKe but it is worth mentioning that other conversion terms exist such as PmPe or FeKe which describe the conversion of energy from the mean potential to eddy potential and the wind work input into the oceanic perturbations respectively.

4.4.2 Barotropic or baroclinic instabilities ?

The mean (averaged over the 8 last years of the simulation), depth integrated (over 2000 m) PeKe and KmKe for the model are illustrated in Figure 4.12. The depth interval

chosen for integration was determined based on the vertical structure of eddies in the model (see Figure 4.8 and Figure 4.9). Figure 4.12 displays an overview of the role played locally by barotropic and baroclinic instabilities in the eddy generation in our model.

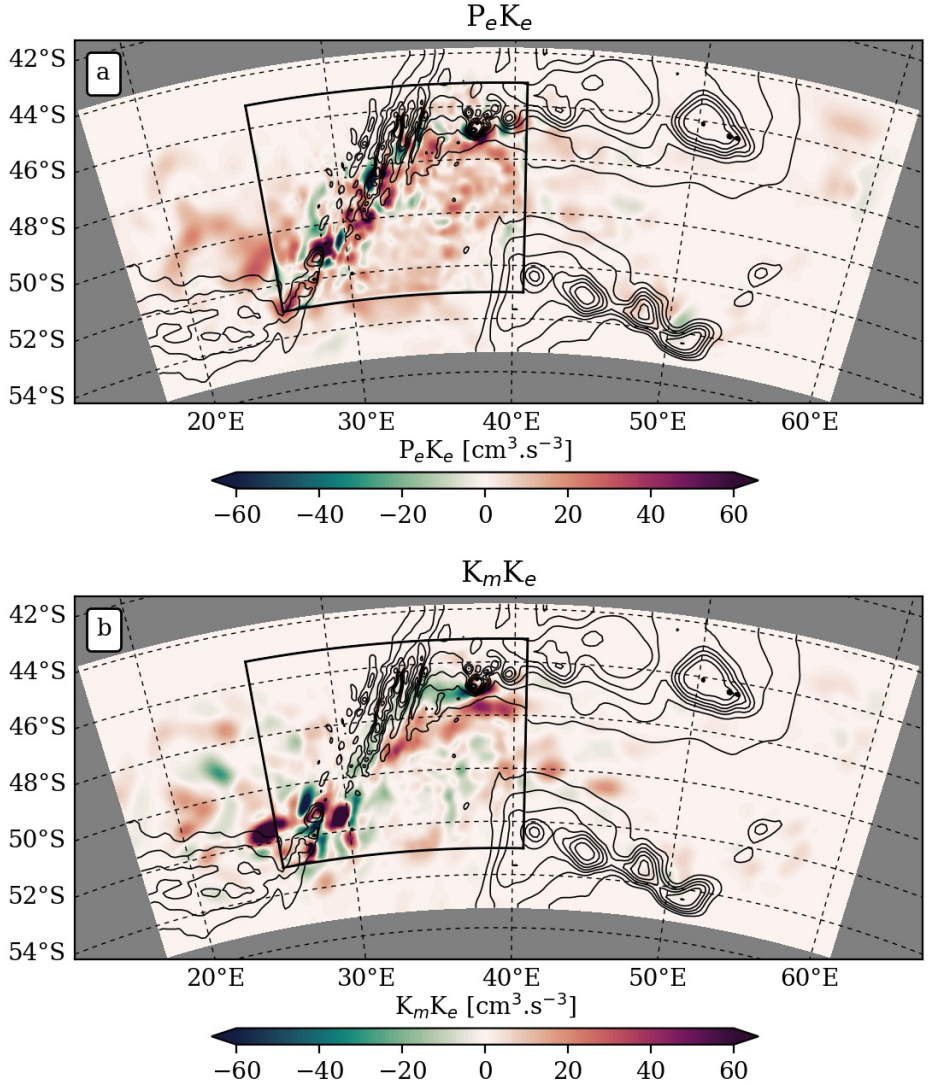

Figure 4.12: *(a) Baroclinic (PeKe) and (b) barotropic (KmKe)conversion term averaged for the last 8 years of our simulation. These terms are vertically integrated over 2000m.*

Upstream the ridge, PeKe is dominant compared to KmKe which means that eddy activity occurs, mostly due to baroclinic instability. Closer to the ridge, around 52°S, a larger KmKe is observed due to the shear created by the interaction between topography and current. Around the southern tip of the SWIR, the KmKe signal is more patchy and displays positive and negative values. Downstream the ridge, along its eastern flank, positive values of PeKe dominate which suggests that eddies are generated by baroclinic instability at this location. However, there are also some negative PeKe spots revealing eddy dissipation. Between 32°E and 40°E, south to the islands, a clear band of positive KmKe is observed showing that the eddies generated in this region are the product of shear processes. Interestingly, right upstream the PEIs, at 35°E-47°S, KmKe shows negative values, indicating that eddies dissipate by supplying their kinetic energy to the mean flow.

This energy conversion analysis reveals that EKE activity is the result of a combination of baroclinic and barotropic instabilities.

4.5 Eddies interaction with the islands

In the studied region, bathymetry strongly controls the circulation and by interacting with the ACC creates mesoscale eddies. These effects of the topography is well reproduced in the model (see Figure 4.1). In this section, we want to investigate on some potential impacts of a different bathymetry on circulation and mainly on mesoscale features. In the previous numerical experiment, we use a topography from GEBCO1 for both the parent and the child grids, with weaker filtering in the case of the child grid. In the new experiment, the parent bathymetry is simply interpolated on the child grid. Basically, the new experiment (hereafter PEIs_bathy) is ran 10 years with exactly the same parameters than the previous one (hereafter PEIs_ref) except for the child bathymetry. Figure 4.13 displays both child grid bathymetries used in each experiment. Figure 4.13 a clearly highlights a better resolution of the bottom topography in the PEIs_ref simulation whereas in PEIs_bathy, the bathymetry is smoother.

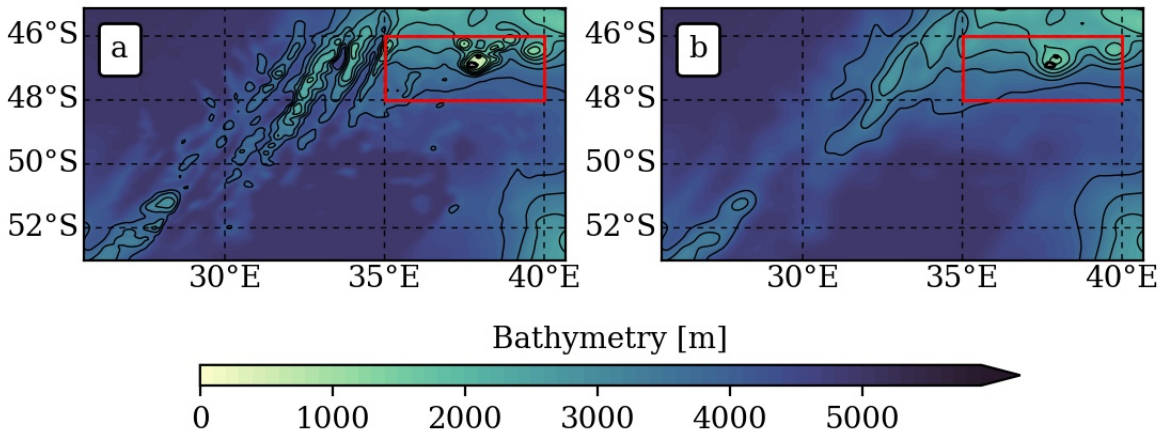

Figure 4.13: Child's bathymetry in (a) PEI_nest simulation and (b) PEI_bathy simultaion. The red frame is the area where variables in Figure 4.15 and Figure 4.14 are averaged.

To investigate the potential change that a different bathymetry could have on the model, spectra of surface EKE and integrated speed amplitudes are computed within the area delimited by the red frame on Figure 4.13. At low frequency (< 2 cpy), EKE from the PEIs_ref simulation has more variance than the new simulation (Figure 4.14). Nonetheless, at higher frequency (> 40 cpy), PEIs_bathy shows more variance. A similar thing is observed for speed magnitude spectra on Figure 4.15: at frequencies > 40 cpy, PEIs_bathy displays more variance than PEIs_ref. This may suggests that a well solved bathymetry might isolate the islands from some offshore processes.

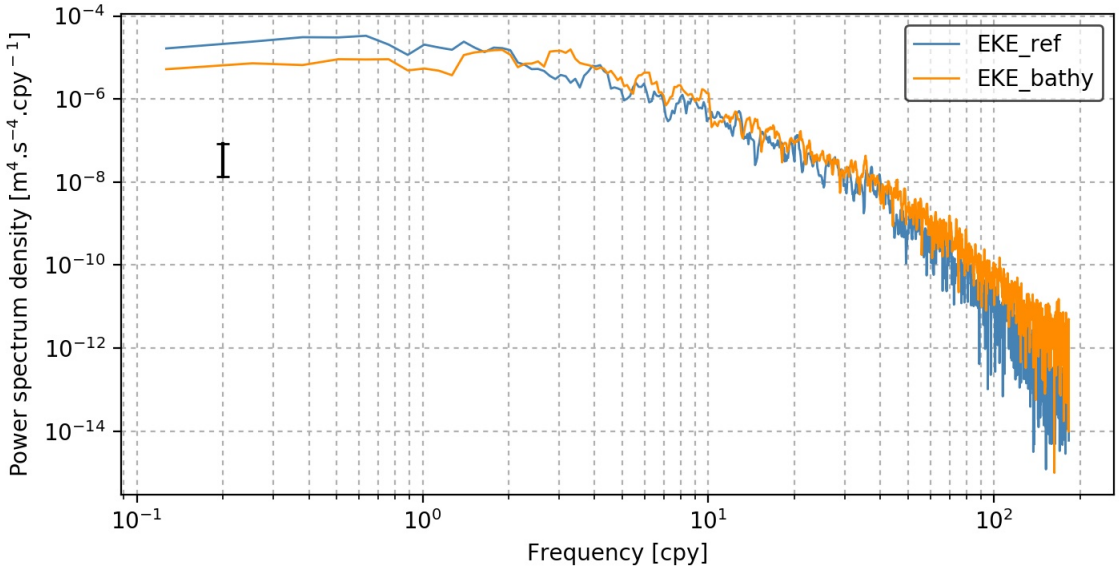

Figure 4.14: *Power spectra density of surface EKE averaged in the red box shown on Figure 4.13: (blue) PEIs_ref simulation and (orange) PEI_bathy simulation. Black vertical bar shows the 95 % uncertainty level.*

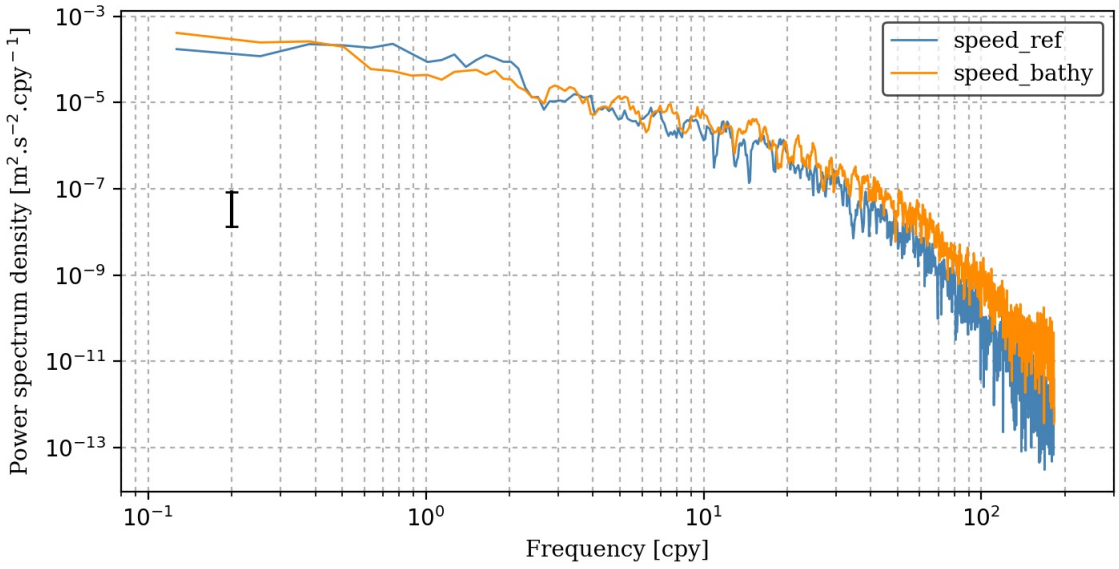

Figure 4.15: *Power spectra density of depth integrated speed amplitude averaged in the red box shown on Figure 4.13: (blue) PEIs_ref simulation and (orange) PEI_bathy simulation. Black vertical bar shows the 95 % uncertainty level.*

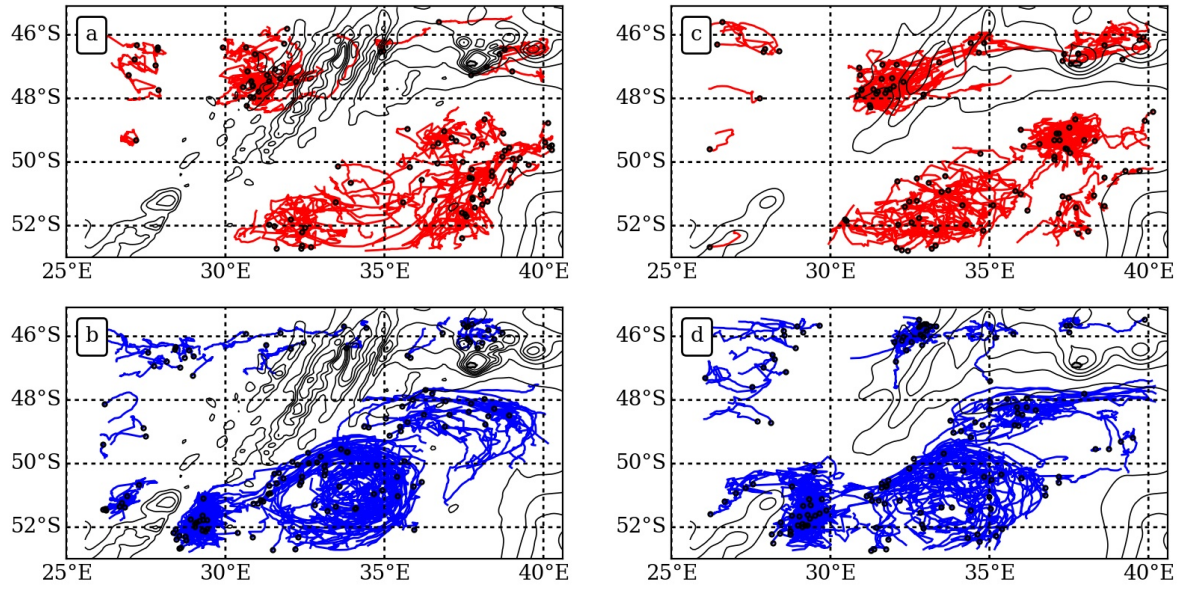

Figure 4.16: *The generation sites, represented as black dots, and trajectories of eddies in (a,b) PEIs_ref and (c,d) PEIs_bathy. Only eddies with a lifespan exceeding 30 days and a radius superior at 30 km are considered. Anticyclone trajectories are in red and cyclone trajectories are in blue.*

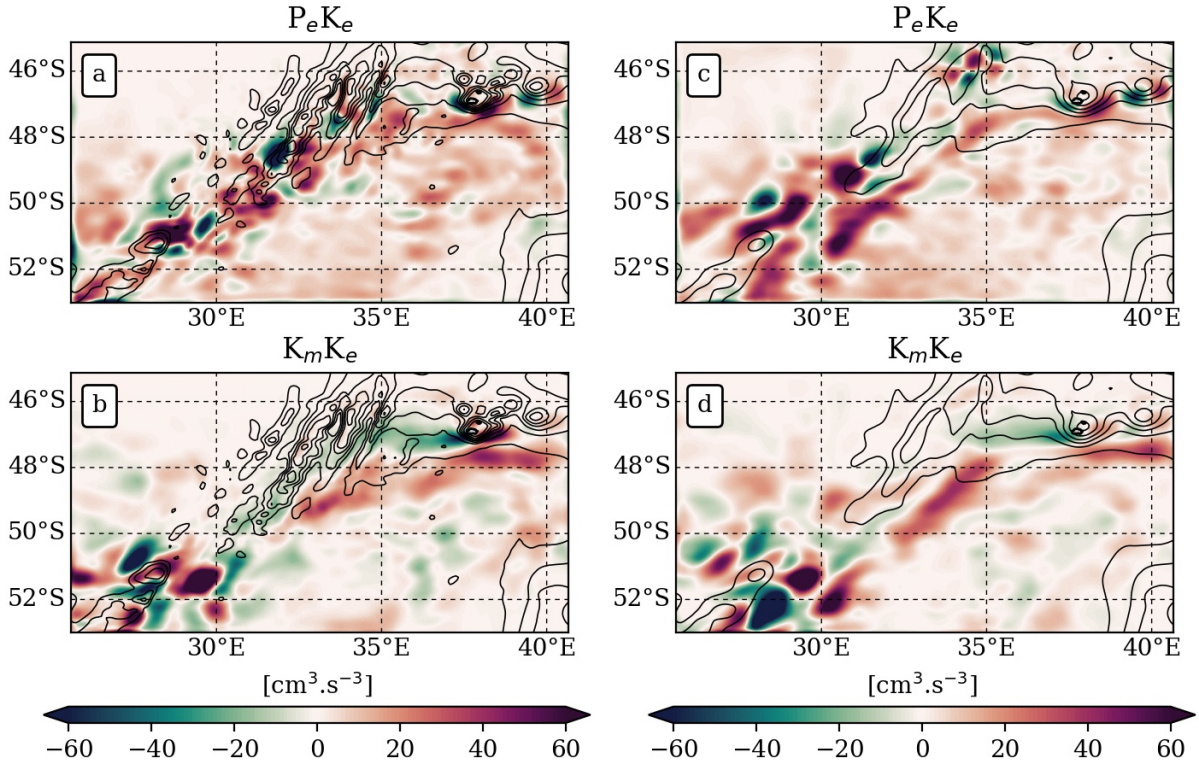

Figure 4.17: *(a,c) Baroclinic (PeKe) and (b,d) barotropic (KmKe)conversion terms averaged for the last 8 years of the (left panels) PEIs_ref simulation and (right panels) PEIs_bathy simulation. These terms are vertically integrated over 2000m.*

By plotting the eddy trajectories in the nested configuration in both numerical experiments, we point out that some anticyclones generated at the ridge (at 47°-48°S) reach the islands in the new simulation which is not the case in the previous one (Figure 4.16 a,c). Moreover, close to the PEIs, more anticyclonic eddies are observed in PEIs_bathy than in PEIs_ref. However, we see less anticyclones north of the islands in the new simulation but a higher concentration at 32.5°E-46°S (Figure 4.16 b,d). It seems that a smoother bathymetry allows anticyclonic eddies originated at the ridge to travel further than in presence of a well resolved bathymetry. In the case of cyclones, no real changes seem to affect the islands.
If we compare the conversion terms of the two numerical experiments, we do not notice much change. We globally observe the same patterns of PeKe and KmKe with a zone of eddy dissipation right upstream the islands. It suggests that a smoother bathymetry does not significantly affect the nature of eddy generation.

4.6 Conclusion

The aim of this chapter is to study the mesoscale eddies properties and the nature of the mechanisms at play in their formation. To do so, we used an idealised 10-years simulation from CROCO model.
In the first place, we compared satellite and model-derived surface EKE and circulation. The eastern part of the "horseshoe" EKE pattern is reproduced by the model, with eddies following the eastern flank of the ridge until the islands. Furthermore, the mean circulation of the ACC is reproduced by the model as well. The currents are strongly constrained by the bathymetry and flow along the ridge.
Secondly, we studied the trajectories and the generation sites of the eddies which turned out to be equivalent for altimetry and the model. A main area of eddy formation between the ABFZ and the Conrad Rise is present in both cases, generating cyclonic and anticyclonic eddies. Moreover, the eastward eddy corridor, described in the literature (Ansorge and Lutjeharms, 2003; Ansorge and Lutjeharms, 2005) is highlighted here. This corridor is the region immediately downstream of the SWIR and extending to the PEIs vicinity, where eddies propagate.
A statistical analysis was performed on different parameters of the eddies (amplitude, diameter, lifespan, propagation speed, distance of propagation and surface EKE) in order to get the main characteristics of the eddies produced in the studied region. From this analysis, we only considered eddies generated in the 20°E-40°E/54°S-46°S box, with lifespan longer than 30 days and radius exceeding 30 km. Cyclones and anticyclones appear to have very similar properties. They showed diameter around 100 km, amplitude of 10-11 cm and a lifespan of about 74 days. In addition, cross sections through two eddies (a cyclone and an anticyclone) were studied to examine their vertical structure in terms

of temperature, salinity and velocity. The mesoscale features turn out to have a deep signature, especially regarding their velocity. To go further and investigate on the source of energy necessary to this high mesoscale activity, EAPE is studied using Roullet et al., 2014 dataset. The model reveals a maximum of energy at 800 m depth which suggests the presence of a local energy source at this depth and confirms the deep reaching characteristic of the eddies.

We focused on the nature of instabilities responsible of this intense mesoscale activity. Two energy conversion terms are examined: KmKe and PeKe. Upstream the ridge and along the eastern flank of the SWIR, PeKe is dominant indicating that baroclinic instability is the main source of eddies generation. Then, closer to the ridge, shear becomes more important producing some EKE from kinetic energy of the mean flow. South the islands, a band of positive KmKe (32°E-40°E) is observed, showing that eddies are the result of barotropic instability. An interesting zone of eddies dissipation (negative values of KmKe) is highlighted, right upstream the PEIs. The model showed that the mesoscale activity in the region of the PEIs is the result of a combination of barotropic and baroclinic instabilities.

At the end of this chapter, we investigated on the impact of a smoother bathymetry on mesoscale activity. A new numerical experiment is computed by interpolating the parent topography on the child grid. With a smoother bathymetry in the nested grid, more variance of surface EKE and integrated speeds are observed at low frequency in the vicinity of the islands. This result suggests that a well solved bathymetry in the model potentially avoid some offshore processes to reach and interact with the island's environment.

5 Simulation of a southward SAF shift and its impact on the Islands

Contents

5.1 Introduction

As aforementioned, the PEIs lie between the SAF and the PF, two important frontal systems of the ACC. These features have been shown to have a direct influence on both physical and biological processes (Graham, 2014). In the PEIs region, the SAF and the PF expose a high latitudinal variability which determines the hydrographic and biological conditions at the archipelago. Two situations, referring to two different positions of the SAF have been described:

- **The SAF lies far north of the PEIs**: the flow between the islands is low enough to allow eddies to be trapped in the inter-island zone (Perissinotto and Duncombe Rae, 1990; Pakhomov et al., 2000; Ansorge and Lutjeharms, 2002). In this situation of water retention, nutrient inputs via runoff from the islands lead to a phenomenon called the "island mass effect" which produces blooms between and downstream of the islands (Boden, 1988; Perissinotto and Duncombe Rae, 1990). In this case, Antarctic species dominate in the region.

- **The SAF lies in closer proximity to the PEIs**: a flow-through system is established between the islands (Pakhomov et al., 2000), preventing the presence of eddies in the area (Ansorge et al., 1999; Perissinotto et al., 2000). Then, the surrounding waters are rich in both subantarctic and subtropical species.

As a consequence, the position of the fronts, especially the SAF, is an important driver of the hydrodynamics of the PEIs region.
Over the last decades, a poleward shift of the ACC (and consequently of its frontal systems) by 1° latitude has been observed, caused by an increase of the westerly wind in the Southern Ocean (Gille, 2008; Morrow et al., 2008; Sprintall, 2008). Ansorge et al. (2009) have shown that this large scale shift also affects the region of the PEIs by highlighting a southward shift of the SAF by about 1° latitude. This southward migration of the SAF, by favouring a through-flow regime, seems to have contributed to a long-term decline in the frequency of phytoplankton blooms in the inter-island region (Pakhomov and Chown, 2003; Allan et al., 2013), and may have strong consequences on higher trophic levels (McQuaid and Froneman, 2008; Allan et al., 2013). The impacts that a southward migration of the ACC would have on the ecosystems of these islands over the next century are difficult to predict (Ansorge et al., 2012).
In the previous chapters, we have showed that the conditions at the islands are highly influenced by the eddies generated at the SWIR by baroclinic and barotropic instabilities. Thus, the objective of this chapter is to investigate on the potential impacts of a shift in the location of the fronts on the eddy production at the SWIR, hence on the islands. Thanks to assumptions made to simplify the configuration, we are able to represent latitudinal migrations of the ACC fronts, by simply shifting the initial and boundary

conditions of our configuration. Four scenarios are performed to explore the sensitivity of our results, presented in the previous chapter, to the latitude of the SAF and the PF, and conjecture on the impact of a southward shift of the SAF onto hydrodynamic conditions around the PEIs.
We start by studying the position of the SAF at the islands and the eddy statistics in the different sensitivity experiments. Then, we analyse the different energy terms involved in eddy generation at the SWIR.

5.2 Design of the sensitivity experiments

In our configuration, initial conditions and conditions applied along lateral open-boundaries are derived from GLORYS (see Chapter 2). In order to simulate a migration of the frontal systems in the model, we simply shift initial and boundary conditions by a given latitude from the original conditions. The surface forcing is not shifted. We decide to perform four experiments: 1° and 2° southward shifts and 1° and 2° northward shifts. It is worth to remind that such a simple design of sensitivity experiments is possible thanks to all assumptions made to simplify the model configuration. Figure 5.1 illustrates the method to simulate a shift of 2°S in the region of PEIs for the temperature (same method is applied to salinity and velocity).

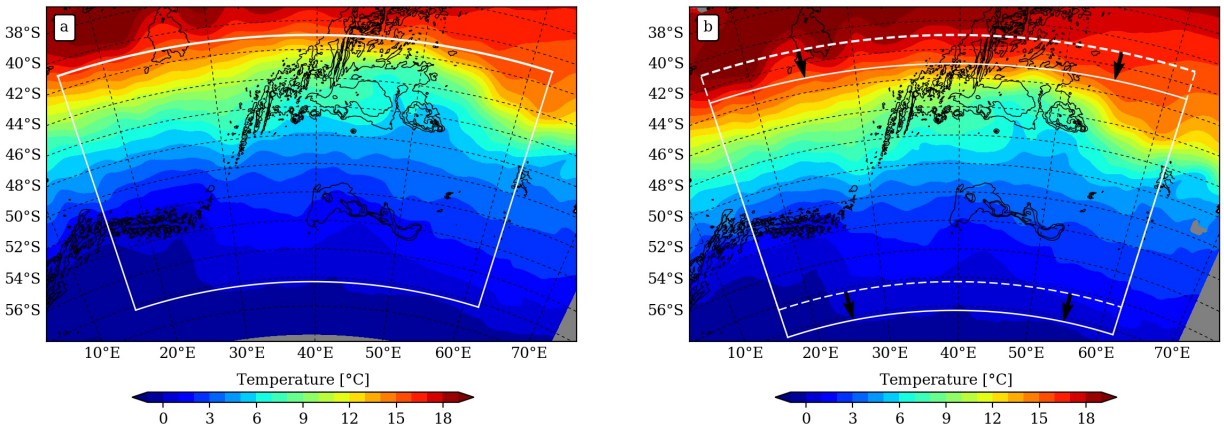

Figure 5.1: *Surface temperature (°C) from GLORYS used to create the initial and boundary conditions in the case of (a) no shift and (b) 2° southward shift (the dashed frame represents the new temperature). Bathymetric contours (-3000 m, -2000 m, -1000 m) from GEBCO1 are overlaid in black.*

The white frame on Figure 5.1 a displays GLORYS temperature used to derive initial and boundary conditions of the simulation we studied previously in Chapter 4. The white dashed frame on Figure 5.1 b represents the new GLORYS temperature obtained after a shift of, in this case, 2° southwards. The data within the dashed frame are interpolated on the grid of CROCO model to give initial and boundary conditions input files. To be consistent with the simulation we have studied in the previous chapter, a nested configuration is necessary and the shifting method is applied to initial conditions

in the nested configuration as well. Figure 5.2 shows the initial conditions obtained from GLORYS temperature in the case of no shift (simulation analysed in Chapter 4) and the case of a 2° southward shift.

From the new initial and boundary conditions, the four experiments are run over 10 years as it has been done previously.

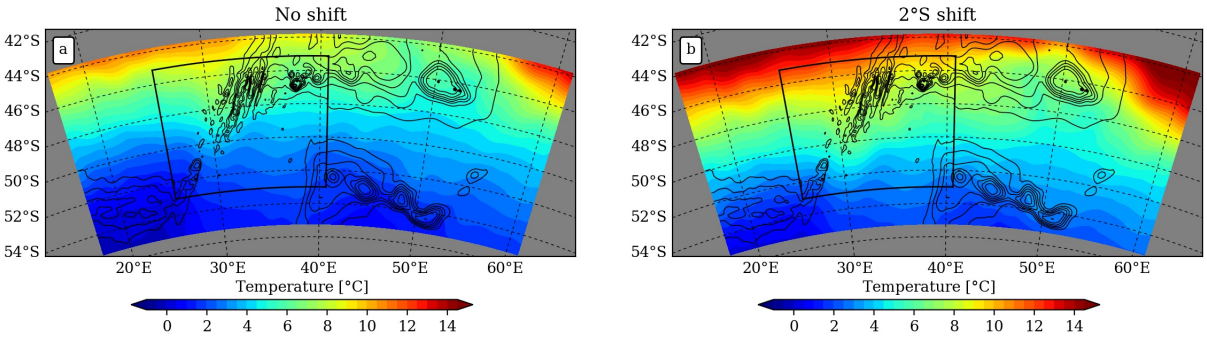

Figure 5.2: *Initial temperature in the case of (a) no shift and (b) 2° southward shift. The black frame represents the nested configuration.*

5.3 Effect of a large scale front shift on the mean circulation

In this section, we study the impact of the shift of initial and boundary conditions on the mean position of the SAF, specifically at the islands, and the mean circulation in the region.

At first, we determine a SSH criteria relative to the SAF and the PF. We follow the method described in Chapter 2 and previously applied on altimetry data to detect the fronts. We found a value of 60 cm and 1 m for the SAF and the PF respectively.

Time series of the position of the SAF at the islands (averaged between 35° and 40°E) are computed and shown on Figure 5.3.

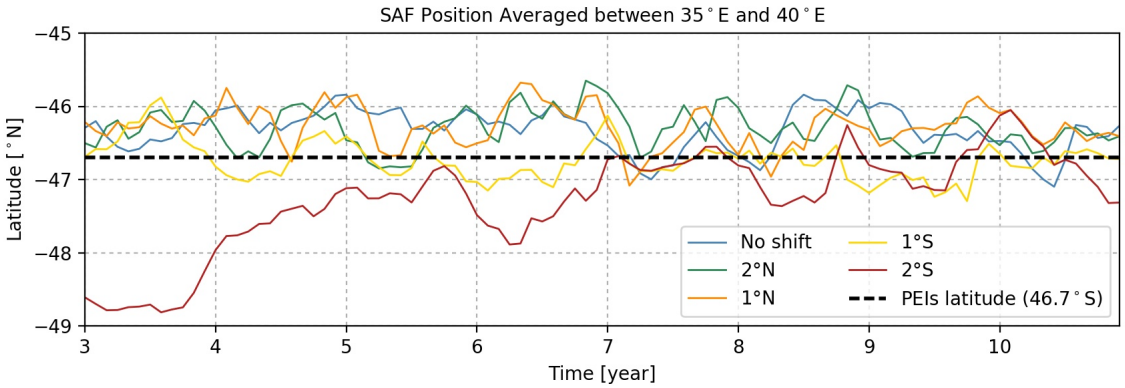

Figure 5.3: *Time series of the position of the SAF for the four experiments.*

We notice that for the 2°S experiment, the SAF only stabilises after 6 years of integration. Hence, in the following of this chapter, we consider only the last four years of the simula-

tions. Times series show a lot of variability in the position of the SAF due to the presence of eddies in the region. From year 7 to year 10, the southward shift scenarios present a SAF globally south of the islands with some excursions to the north of the archipelago. In the case of a northward shift, the SAF stays north of the islands most of the time, except for rare exceptions.

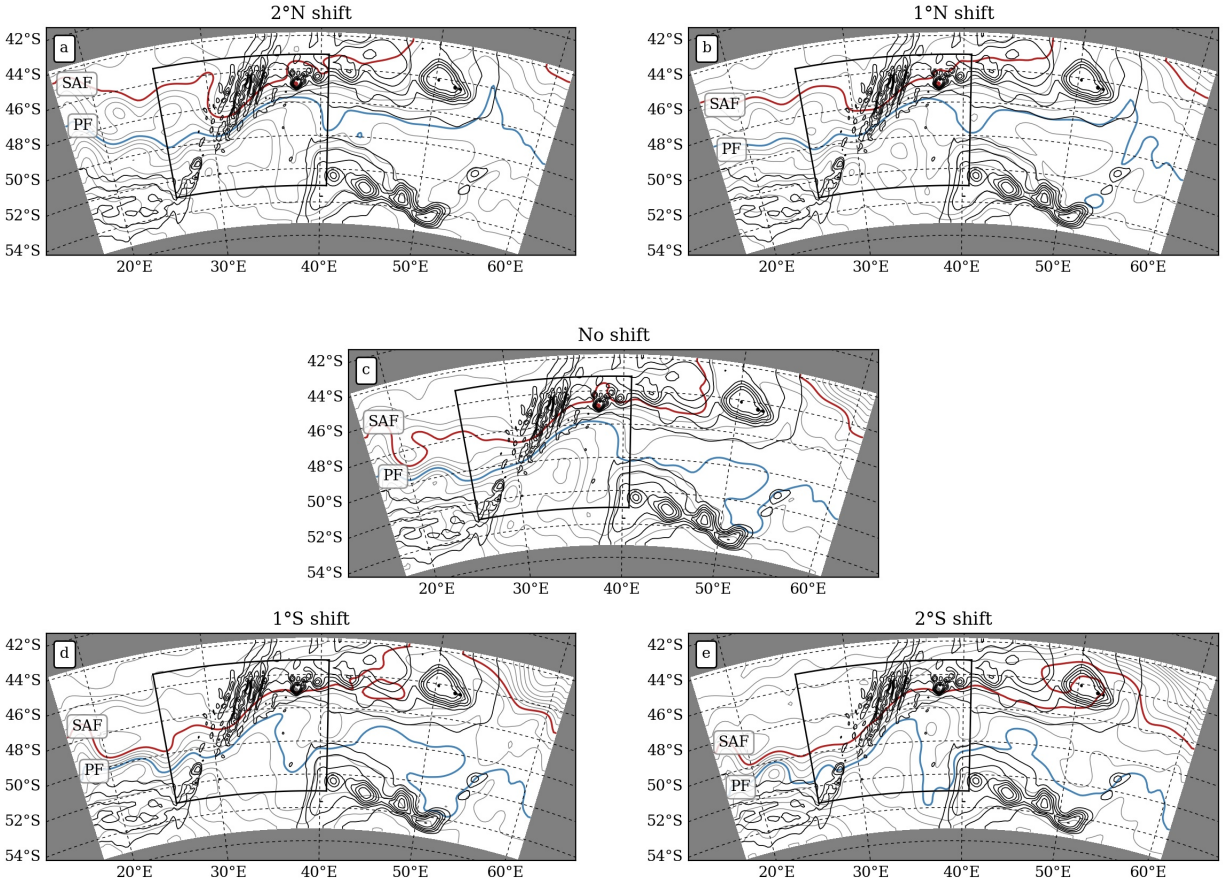

Figure 5.4: *Mean position of the (red) SAF and (blue) PF in each scenario. The positions are averaged over the last four years of the simulations. The streamlines and the bathymetry are overlaid in grey and black respectively.*

The mean positions of the SAF and PF are displayed on Figure 5.4. We clearly see the shift of the frontal systems at the western boundary. Regardless of the shift of the SAF upstream the ridge, the position of the front at the ridge is globally the same in any case. In the northward shift experiments, around 30°E, the SAF is forced to go southwards in order to follow the ridge. This is a consequence of the strong influence of the bathymetry in the region. In the case of a southward shift, at 36°E, the PF takes suddenly a turn southwards. This behaviour is also observed in the other scenarios but the deflection is done more east and it is weaker. It might be the result of the fact that by shifting the PF southwards, the latter is moved away from the

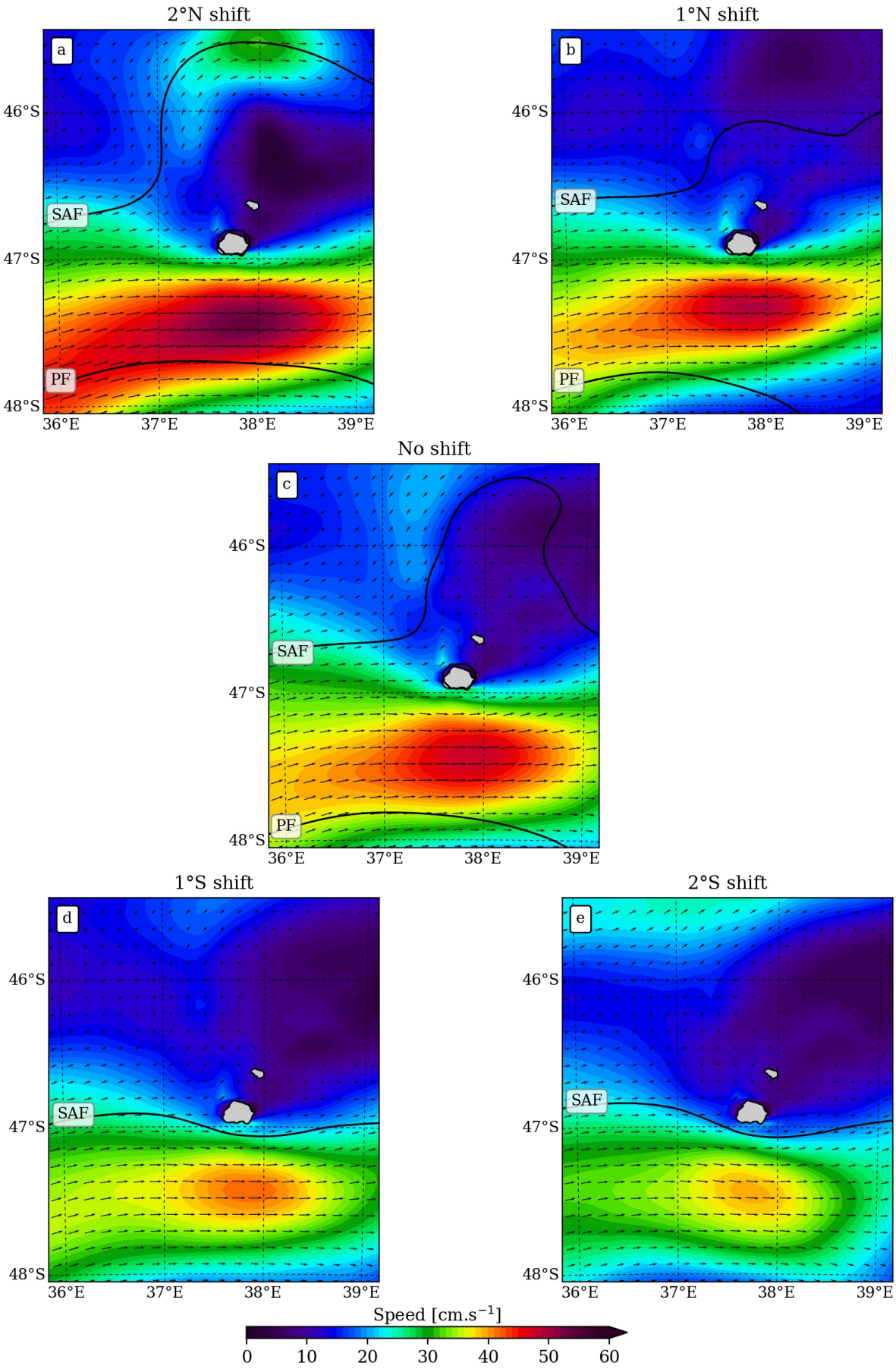

Figure 5.5: *Mean surface velocity (direction and amplitude) in each scenario. The mean positions of the SAF and PF are overlaid in black. The arrows are plotted every two grid points.*

SWIR and gets a bit closer to the Conrad Rise. Then, the PF feels more the influence of the Conrad Rise which forces the PF to deflect southwards.
In spite of important large scale changes, the topographic constraint is too strong that variations in the frontal positions are weak at the islands (in agreement with Graham et al., 2012). Moreover, regarding the 2°N and the 1°N experiments, in the western part of the domain, the streamlines are more homogeneously distributed along the latitudes and are not constrained into jets like in the others. The fact that the setting is idealised might has leaded to a problem in the SAF adjustment at large scale upstream the ridge. Figure 5.5 shows the mean surface velocities and the frontal positions in the four scenarios. A band of high zonal velocities extends south of the PEIs, between the SAF and the PF, with maximum values in the 2°N shift experiment. Interestingly, these high velocities, positioned south of the islands do not follow the SSH contours (SAF). Barotropic velocities (not shown here) present the same direction as surface velocities which reveals a strong signature of barotropic velocities on surface velocities. This suggests that at this location, the β effect is strong and the flow preferably follows the contours f/h instead of the SSH contours.
In the literature, when the SAF is far to the north of the PEIs, the flow rate of the ACC around the islands is slow, while when the SAF lies farther south and close to the islands, the region around the PEIs experiences much higher flow rates, resulting in a flow-through system. Figure 5.5 d,e display a SAF close to the archipelago but does not highlight any high velocity between the islands. Notice that an slight increase in velocity can be observed right upstream the islands on Figure 5.5 b,c. Unfortunately, there are too few grid points between the islands to be able to conclude on any significant change in speed at this location.

Summary of Section 5.3: Impact of a front shift on mean circulation

- The simulation of a frontal systems migration has confirmed the strong control of the topography on frontal positions in the region of the PEIs.
- The mean circulation is better represented upstream the ridge, when the fronts are moved northwards: streamlines are more homogeneously distributed.
- The configurations do not allow us to confirm a set up of a flow-through system between the islands when the SAF is close to the archipelago.

5.4 Impact of a large scale front shift on the eddies

5.4.1 Eddy Generation

In the previous chapters, we have seen that eddies generated at the ridge by baroclinic and barotropic instabilities, influence the hydrodynamic conditions at the PEIs. In order to illustrate the impact of a potential shift on eddy production, the number of eddies per year is computed in the vicinity of the islands. In Figure 5.6, we highlight that if the frontal systems are shifted polewards, the number of eddies per year tends to decrease which implies less support in nutrients for the fauna living on the PEIs.

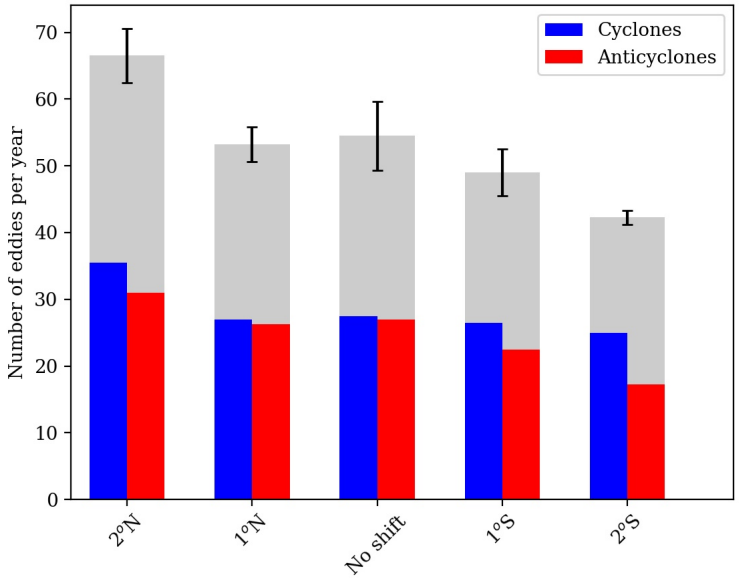

Figure 5.6: *Number of eddies per year in the four configurations. Grey is for the total number of eddies (cyclones and anticyclones) per year. The black bars represent the standard deviation.*

5.4.2 How EKE changes by shifting the fronts?

Similarly to what it has been made in the previous chapter, EKE is is plotted for each scenario (Figure 5.7). When the frontal systems are shifted northwards, the simulations show an increase of EKE, especially along the eastern flank of the SWIR (between 30°E and 40°E). However, the spots of high EKE localised on each side of the southern tip of the ridge (26°E-51°S and 30°E-51°S) tend to disappear when the fronts shift northwards. It is certainly due to the fact that the PF, by migrating equatorwards, does not interact with the southernmost part of the ridge anymore. Upstream the ridge, we observe an increase in EKE production. When the fronts are shifted southwards, the SAF lie south of the islands and, except at 28°E-50°S, we no longer observe EKE upstream the ridge. If the fronts migrate 2° polewards, Figure 5.7 e highlights a serious decrease in EKE in the region of the islands. This last result supports what we have shown previously: a decrease in eddies at the islands. Interestingly, the 1°N

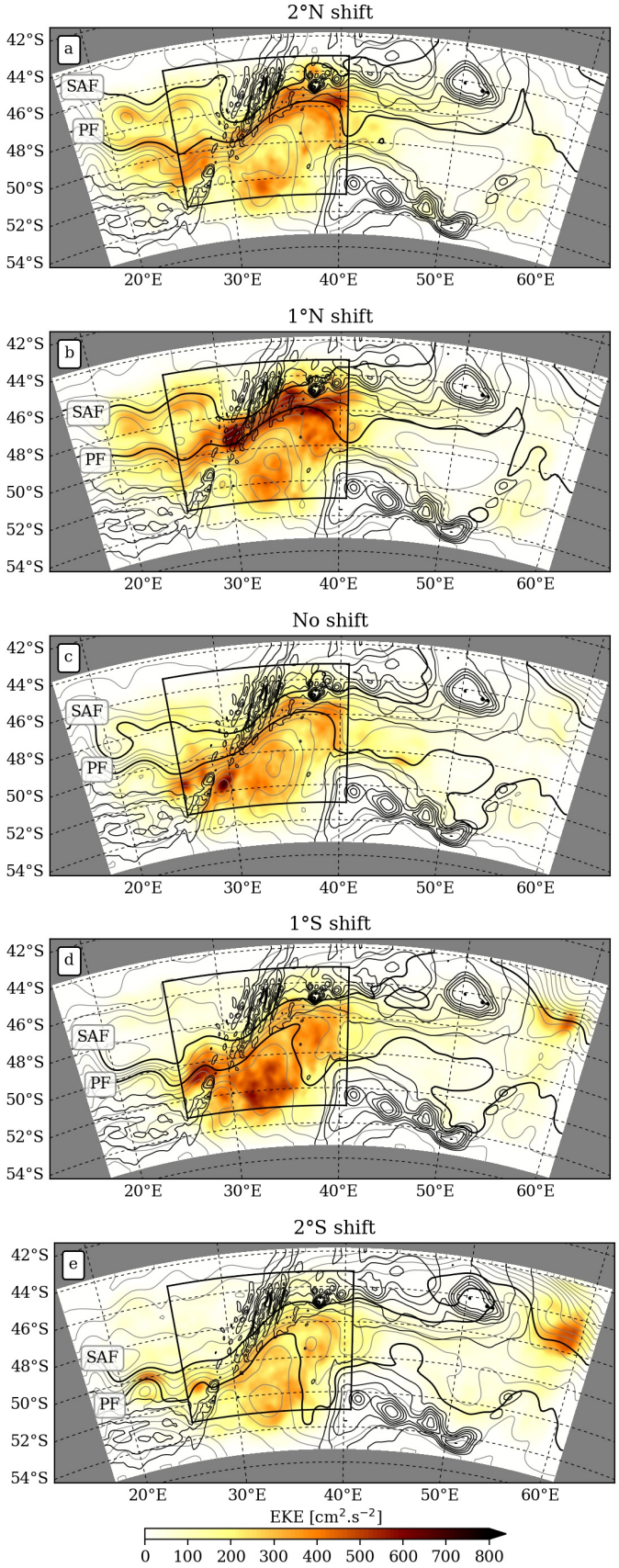

Figure 5.7: *Mean surface EKE of the last 4 years of the CROCO simulations. The grey lines are the streamlines and the two thick black lines represent the SAF and the PF. The black frame defines the child box.*

configuration seems more "realistic" than the one with no shift. Indeed, the EKE "horse-shoe" pattern described earlier in Chapter 3 and specific to the region is better represented in Figure 5.7 b than in c. As it has been mentioned previously, it is probably due to the idealisation of the configuration and its adjustment. In addition, the power density spectra of EKE are computed in the vicinity of the archipelago (box 35°E-40°E/46°S-48°S). Figure 5.8 shows parallel spectra but reveals less energetic spectra when the fronts are shifted southwards. These spectra show that, in each experiment, the same processes are in play in the vicinity of the islands but that these processes are less intense when the fronts migrate southwards. In other words, the eddies are the processes responsible of the EKE in the region and when the fronts shift southwards, the number of eddies in the PEIs area decreases.

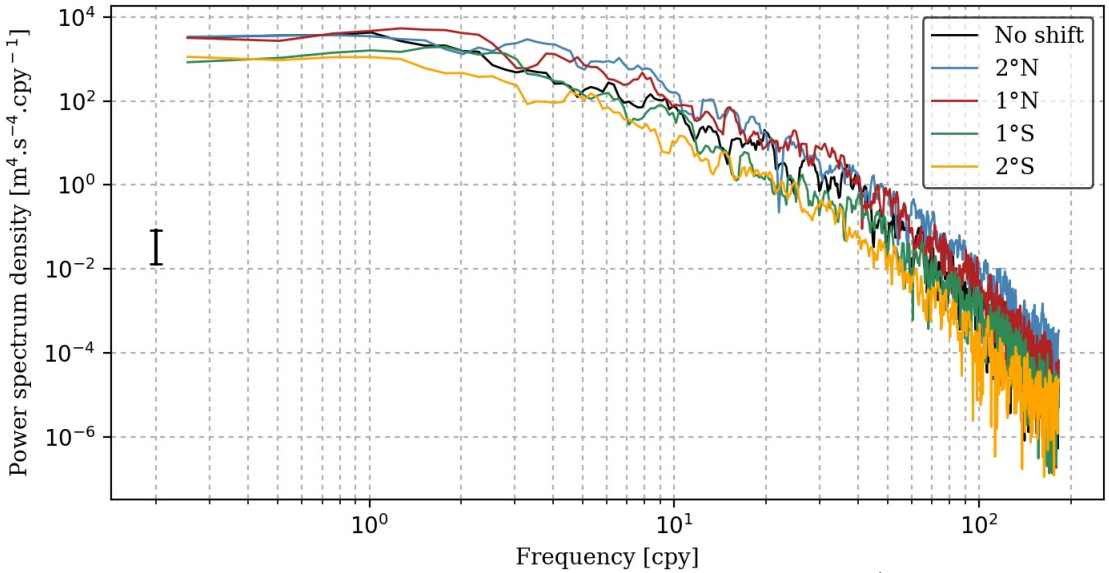

Figure 5.8: *Power density spectrum of EKE averaged in the box 35°E-40°E/46°S-48°S, over the last four years of simulations.*

5.4.3 Eddy Available Potential Energy

In the same way than in the previous chapter, we explore the distribution of EAPE for the four experiments. EAPE at 800 m is shown on Figure 5.9 and we see that the maximum of EAPE is always confined between the PF and the SAF and spreads along the eastern flank of the SWIR. The 1° northward shift presents a big pattern of high EAPE, spreading from the ABFZ until beyond 40°E whereas the 2° northward shift scenario shows a smaller pattern of high EAPE. When the fronts are moved 1° southwards, an important spot of EAPE is displayed at the fracture zone and then the pattern extends along the ridge until 40°E. In the case of a 2° southward migration, the maximum EAPE pattern becomes smaller and it is centered at 35°E. Furthermore, when the SAF is south of the PEIs (Figure 5.9 d,e), a spot of high EAPE

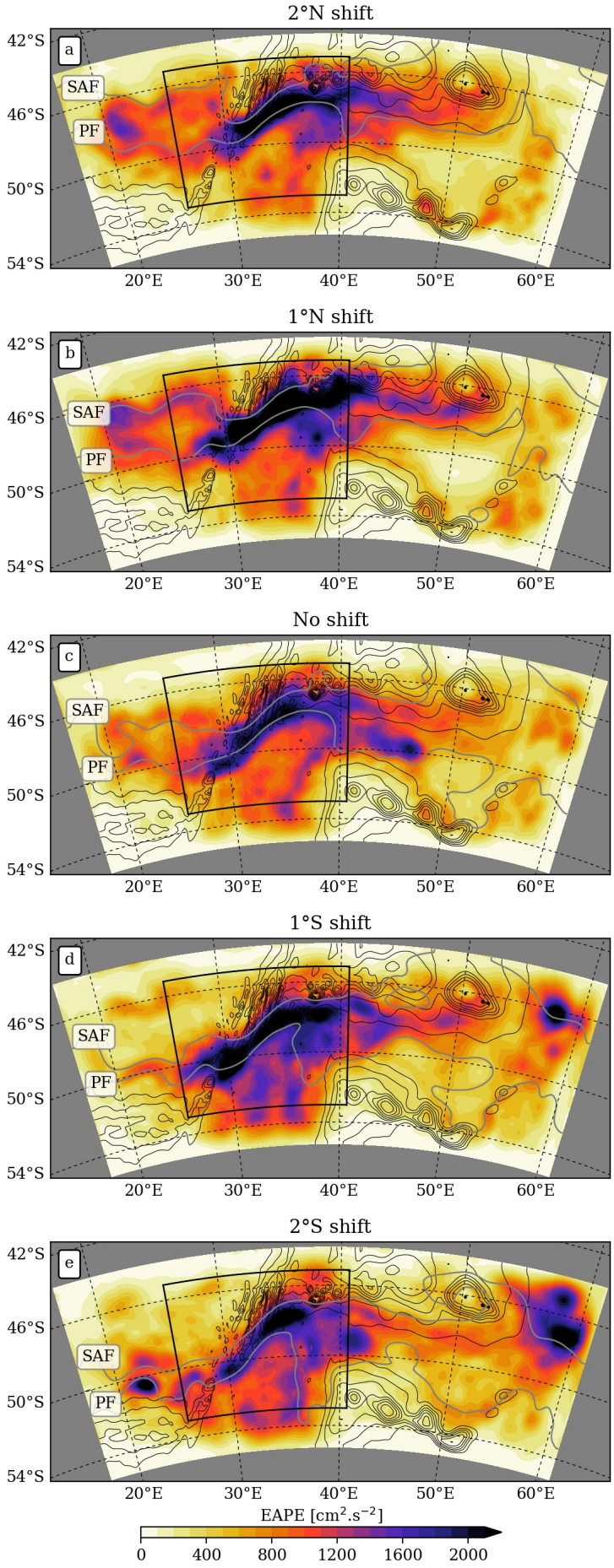

Figure 5.9: *Mean EAPE at 800 m in the five configurations.*

is observed at the extreme east of the studied domain. Interestingly, the original simulation (no shift, Figure 5.9 c) seems to have less EAPE. This simulation might represent a mean state which minimises the energy.

Figure 5.10 illustrates the profile of EAPE at 35°E-48°S, including the base simulation (no shift). It shows that, in all experiments, the maximum of EAPE is around 900 m and that this maximum varies from 2400 $cm^2.s^{-2}$ to 2600 $cm^2.s^{-2}$. The fact that the maximum is at approximately the same depth in the four cases suggests that the processes involved are the same. Thus, moving the fronts from their initial positions does not impact very much the depth of the EAPE maximum nor its value but impacts the extension of the pattern of this maximum.

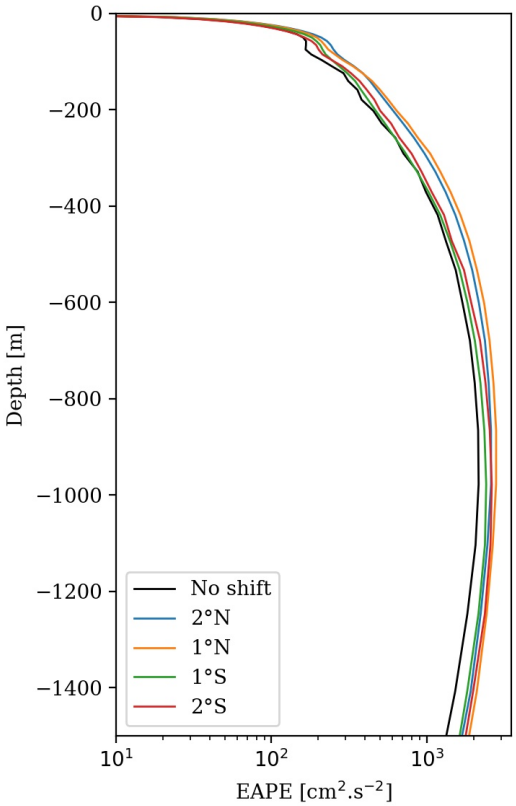

Figure 5.10: *EAPE profils at 35° E - 48° S.*

5.4.4 Impact of a front shift on eddy formation mechanisms

We have just seen that a southward shift of the fronts potentially decreases the number of eddies tracked in the vicinity of the archipelago. In this section, we focus on the impact of a SAF and PF migration on the mechanisms responsible for eddy formation.

Figure 5.11 highlights a serious decrease of energy transfer from eddy potential energy to EKE, when the fronts are shifted southwards. When the SAF is north of the islands (Figure 5.11 a,b),

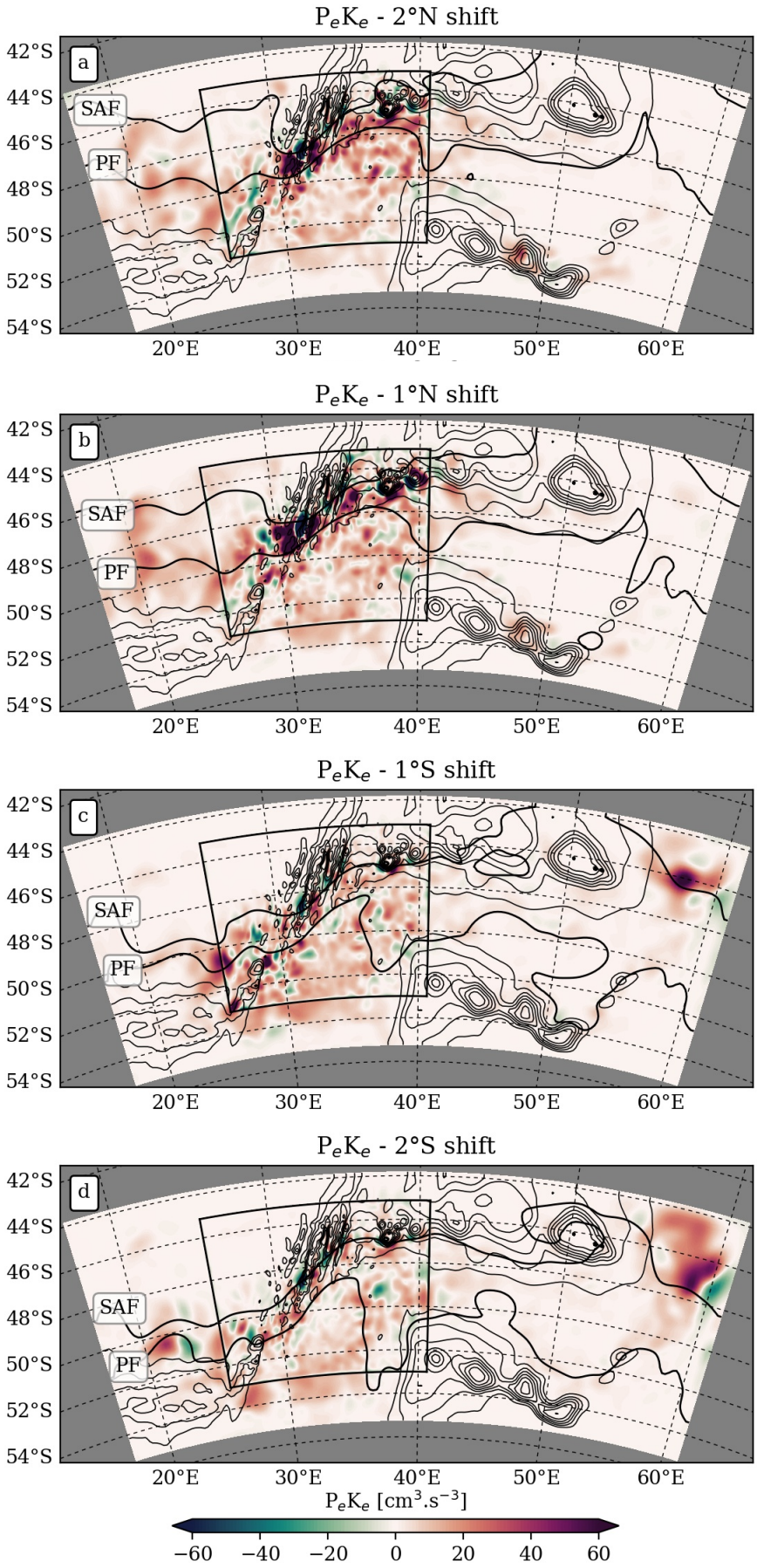

Figure 5.11: *Baroclinic conversion term (PeKe) averaged for the last 8 years of simulation and vertically integrated over 2000 m.*

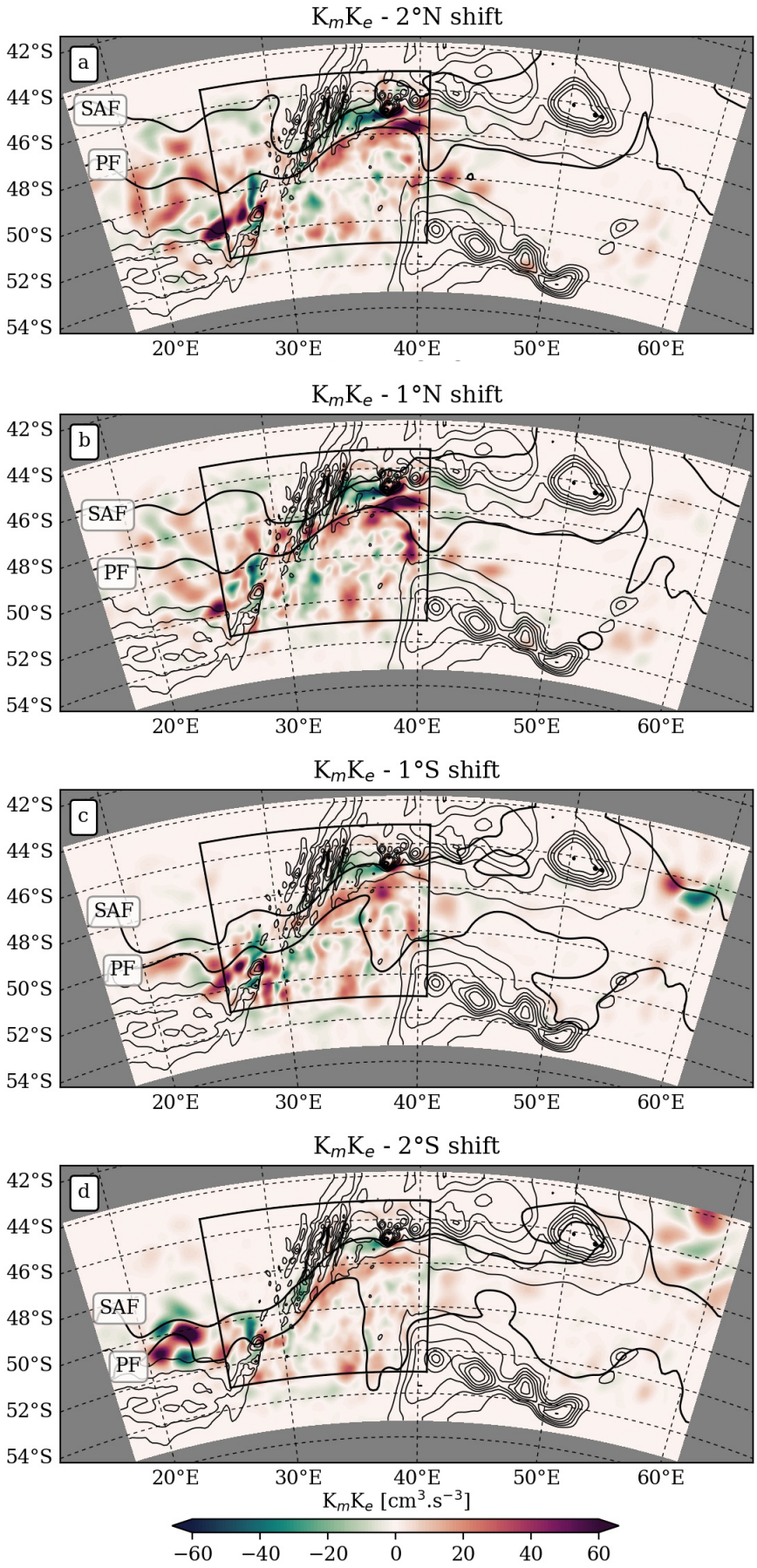

Figure 5.12: *Barotropic conversion term (KmKe) averaged for the last 8 years of simulation and vertically integrated over 2000 m.*

baroclinic instabilities along the eastern flank of the ridge (between 30°E and 40°E) are important. However, when the SAF switches south of the PEIs, PeKe becomes weak along the ridge. Even upstream the SWIR, we observe a substantial decrease of baroclinic instabilities. Regarding the conversion from the mean kinetic energy to the EKE (Figure 5.12), a similar decrease is noticed. The band of positive KmKe observed initially south of the islands tends to disappear when the SAF moves southwards. Moreover, the area right upstream the islands, at 35°E-47°S, where eddies dissipate, is no longer a place of energy conversion when the fronts have been shifted by 2°S. It is important to mention that shifting the fronts equatorwards (Figure 5.12 a,b) seems to increase barotropic instabilities upstream the SWIR, between 20°E and 30°E.

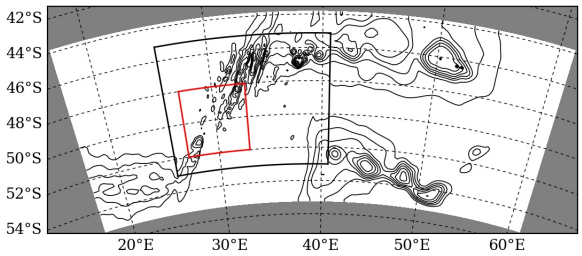

	PeKe [$cm^3.s^{-3}$]	KmKe [$cm^3.s^{-3}$]
2°N shift	5.83	-0.87
1°N shift	7.31	-0.92
No shift	4.78	-0.58
1°S shift	4.68	-0.84
2°S shift	2.02	-1.66

Table 5.1: *PeKe and KmKe averaged in the red box shown on the map above for each scenario.*

Table 5.1 displays the values of PeKe and KmKe averaged in the box 27-33°E/48-52°S, where mesoscale features are mostly generated. It is clear that a southward shift from their initial positions of the frontal systems leads to a decrease in PeKe. For the No shift experiment the averaged PeKe value is 4.78 $cm^3.s^{-3}$ and drops to 2.02 $cm^3.s^{-3}$ for the 2°S experiment. A southward shift of the fronts seems to impact the energy transfer from eddy potential energy to eddy kinetic energy, pointing out the decrease of baroclinic instabilities, essential mechanism in eddy formation. KmKe values, all negative, decrease as well which reveals an increase of eddy dissipation in the mean flow. This result supports what we have found in the previous sections, which was a decline in EKE and thus in eddies when the fronts are shifted southwards, through a reduction of transfer of energy by baroclinic instability.

Summary of Section 5.4: Impact of a front shift on eddies

- A decrease in the number of eddies per year.
- A serious decline in EKE is noted when the SAF is shifted 2° southwards.
- In our experiments, we have shown that moving the fronts southwards affect the energy but not the processes which remain the same.
- Moving the fronts from their initial positions affect the extension of the maximum pattern of EAPE but not its depth.
- A southward shift of the SAF affects the mean energy transfers: a decrease in baroclinic instabilities hence in the generation of eddies and an increase in eddy dissipation.

5.5 Conclusion

Migration of the frontal systems is analysed using an idealised regional simulation and by shifting its initial and boundaries conditions. Four experiments are performed, modelling four different positions of the SAF and PF.

Despite of important changes in the initial latitudinal position of the SAF and the PF, the topography exerts a strong control on them which implies weak variations in their positions. However, moving the fronts northwards reveals a better distribution of the streamlines upstream the ridge: the circulation is less constrained into jets. Even though the circulation is better solved in the northward shifts experiments, the configurations do not confirm the presence of a through-flow system between the islands when the SAF is in the vicinity of the islands.

The surface EKE is found to increase along the eastern flank of the ridge when the fronts migrate northwards. If the fronts move by 2°S from their initial position, the level of EKE produced in the region is significantly reduced. The eddy tracking result supports the idea of a decrease of eddies generated per year in the area when the fronts migrate polewards.

The study of EAPE reveals that a frontal shift mainly impacts the spreading of the EAPE maximum and that this maximum is always located between the SAF and PF. A poleward or equatorward migration of the fronts does not affect significantly the depth of the EAPE maximum in the model.

An analysis of the two energy conversions terms, KmKe and PeKe, highlights a serious decrease of energy conversion when the fronts are shifted southwards from there initial

position. Baroclinic instabilities tend to disappear in the region when the SAF moves south away from the islands. KmKe reveals an increase in eddy dissipation with the fronts migrating southwards. Therefore, this study of KmKe and PeKe explains, at least partially, why less eddies are observed in the region.

These idealised experiments have highlighted that a southward shift of the frontal systems, especially the SAF, could lead to a decrease of mesoscale features in the PEIs region. In Chapter 3, altimetry data have shown a southward trend in position of the SAF and a negative trend in EKE in the region of PEIs as well. Thanks to the simulations performed in this chapter, we can confirm a potential link between a southward migration of the SAF and a decrease in eddies. Eddies are known to be support the ecosystem of the islands, a decrease in eddy production might have consequences on the islands environment.

6 Conclusions & Perspectives

Contents

6.1 Conclusions

The PEIs are found in a zone of the ACC where the SAF position is highly variable in latitude and where mesoscale activity is intense. The overall objective of this thesis was to understand better the influence of these features in the variability of hydrodynamics at the islands, hence potentially local ecosystems.
In this final chapter, we recall the important questions addressed in Chapter 4, 5 and 6 and summarise the pertinent findings. This is followed by overall conclusions and then we give some perspectives for a future work.

6.1.1 Offshore processes versus local processes: What are their impacts on the circulation observed at the PEIs?

In Chapter 3, we investigated on PEIs ocean dynamics to improve our knowledge of PEIs circulation while differentiating offshore and local forcings. To carry out this study, we used observations available for the region like moorings, CTD and altimetry data. The islands are under the influence of large scale physical processes as well as local processes. We found that the SAF position, the most important large scale process driving the physical dynamics of the PEIs region, is highly variable at interrannual and monthly time scales. Furthermore, the SAF reveals a significant multidecadal southward trend which contrasts with recent studies supporting the long-term stability of the meridional position of the ACC fronts at the Southern Ocean scale (Graham et al., 2012; Gille, 2014; Shao et al., 2015; Chapman, 2017). This southward trend observed at the islands could have consequences on the archipelago's environment according to some studies. The SAF shows also similar time variations as SAM index at low and interannual frequencies. A sensitivity of the position of the fronts to SAM has been already highlighted by Sallée et al. (2008) and Kim and Orsi (2014) in the southeast Indian and southeast Pacific basins.
EKE shows a strong interannual and intra-annual variability in the region and also a negative trend. This trend is in contradiction with recent studies which has pointed out an increase in EKE in response to the strengthening of the westerly winds in the Southern Ocean (Meredith and Hogg, 2006; Hogg et al., 2015; Patara et al., 2016).
At local scale, we saw that eddies produced at the SWIR, upstream the islands, clearly influence the inter-islands environment, affecting temperature, mixed layer and velocity. The SAF, as well, impacts the temperature between the islands, bringing cold Antarctic waters around the PEIs when it is north and warmer subantarctic waters when it is south. The role of the tides has been studied and that helped to clarify their importance as driver of variability between the two islands.

6.1.2 What are the processes at play in eddies formation in this region?

In Chapter 4 we focused on the eddies produced at the SWIR to determine their properties and the nature of the mechanisms at play in their generation.
An idealised simulation evidenced the deep signature of the eddies originating at the SWIR and display similar properties for cyclones and anticyclones. A maximum of EAPE is found around 800 m at the ridge suggesting a local source of energy at this depth necessary to supply high mesoscale activity of the region. The presence of this maximum of energy confirms the deep reaching characteristic of the eddies. We also highlighted the fact that the eddies are the product of a combination of barotropic and baroclinic instabilities.

6.1.3 How does the southward shift of the SAF affect eddies generation?

In Chapter 5, we tackled the issue of whether the southward fronts migration observed at the Southern Ocean scale has an impact on hydrodynamic properties at the islands. Idealised sensitivity experiments were set up in order to simulate four different shifts of the SAF and PF.
The strong topographic control exerts on the ACC in this region has been confirmed. Even though important changes are initially made in the latitudinal positions of the fronts, they are still constrained by the SWIR and weak variations in there positions are observed at the longitude of the archipelago. Nonetheless, a northward shift of the fronts leads to a mean circulation less constrained into jets and streamlines more homogeneously distributed.
Moving the fronts northwards from their initial positions also increases surface EKE along the eastern flank of the SWIR whereas shifting the fronts by 2°S eddy energy is substantially reduced. Frontal system shift impacts the EAPE maximum spread without really impacting the value of the maximum and its depth.
Finally, shifting the fronts southwards implies a reduction in barotropic and baroclinic instabilities. Eddy dissipation is enhanced while energy transfer from the mean flow to the eddies decreases. Eddy tracking performed in the region supports the result of a diminution of eddies generated at the ridge when the fronts are shifted southwards.

6.1.4 Overall Conclusions

As a conclusion, in this dissertation, we clarified the role of changes in the large scale Southern Ocean on the archipelago's dynamics. Mesoscale features originated at the

SWIR affect the temperature, the depth of the mixed layer and velocities in the inter-islands region. The position of the SAF also affects the temperature between the islands. A southward trend in the position of the SAF have been underscored in the region of the PEIs, contrasting with what has been observed in the Southern Ocean at large scale (Graham et al., 2012; Gille, 2014; Shao et al., 2015; Chapman, 2017). On the other hand, this result supports, in a way, some observations of trends in the positions of the fronts made in specific regions (Sallée et al., 2008; Kim and Orsi, 2014). This comes locally with a negative trend in EKE which differs with an increase in EKE shown by recent studies (Meredith and Hogg, 2006; Hogg et al., 2015; Patara et al., 2016). This disagreement might be the result of a scale difference in the studies. Indeed, in this thesis, the study is very regional whereas Meredith and Hogg (2006), Hogg et al. (2015) and Patara et al. (2016) have performed their work at the Southern Ocean scale. This observed negative trend is consistent with the model experiments that highlighted that shifting the fronts southwards might seriously decreases the baroclinic and barotropic instabilies and so leads to a decrease in eddy production. In this context where eddies are known to support the ecosystems of the islands, a southward shift in SAF, hence a decrease in eddy production, might have significant, if not dramatic consequences on the islands environment and ecosystems.

6.2 Discussion

Observations of the hydrography and circulation around PEIs are very scarce, in particular in the deep ocean. We have attempted to make full benefit of all available observations, but that was clearly insufficient to determine the mechanisms of variability at the islands. This motivated the development of a model configuration to represent and study the processes at play in this oceanic environment. As we decided to focus on the interaction between the ACC and the PEIs, we chose to develop a configuration that would represent those processes correctly, at relatively high resolution, with a strong constraint on the lateral boundaries towards large scale oceanic variables. To simplify the development of the configuration, and because it was not of primary relevance for our scientific question, we made a few assumptions on the other forcings that deserve to be discussed. Atmospheric forcings of the configuration are based on a climatological product while we could use a realistic approach and time varying wind to perform interannual simulations. Indeed, even though the ACC is strongly controlled by the topography in the PEIs region, wind plays a role in driving the variability of the fronts. Hence a simulation that includes interannual variability in the large scale ACC fronts as well as in the wind forcing, could help understanding better the impact of large scale ocean and climate changes onto PEIs environment.

Another point which could be argued is the resolution of the model. As highlighted

in Chapter 5, the resolution in the model is not high enough to be able to detect any changes in the inter-island flow. Because the position of the SAF is supposed to modify the currents regime between the islands, it would be interesting to set up a configuration at higher resolution than $\frac{1}{12}^\circ$ to verify this.

6.3 Perspectives

This study should be considered as a first step towards understanding better the ocean dynamics around the archipelago. Further investigations are necessary to clarify the impact of global ocean and climate changes onto local ecosystems:

- ***Biogeochemical coupling***: The fronts, especially the SAF and the mesoscale features originating at the SWIR are important drivers of the ecosystems of the PEIs. The SAF influences the type of waters surrounding the archipelago by bringing Antarctic or subantarctic waters depending on its position. Eddies carry waters rich in nutrients to the islands and sustain the ecosystem. Hence it is expected that a change in SAF position has an impact on the primary and secondary production, thus all ecosystems at the islands. Developing a coupled physical and biogeochemical model around PEIs would be useful to test this hypothesis. Yet, one has to be aware of the complexity of local processes that seem to be at play in the close vicinity of the islands, for example the importance of tides as we highlighted in Chapter 3.

- ***Climatic scenario***: Southward migration of the ACC fronts is a low frequency process, and present day observations are still too short to characterize it at the regional scale. Using outputs from climate models as surface and lateral boundary conditions for our regional model, would allow to run multi-decadal scale simulations and represent directly the southward migration of the ACC fronts in the PEIs region.

- ***Extending moorings time series***: So far we have collected only 2 years of moorings data. The moorings are still between the islands and it would be interesting to complete the temperature time series to follow the evolution of the SAF.

- ***Same study applied to other islands***: Does a southward shift of a frontal system impact the hydrodynamics of subantarctic islands such as Crozet or Kerguelen islands? In the case of the PEIs, we have highlighted that the impact of the SAF migration goes through the production of eddies at the SWIR, because the topographic control on the ACC is very strong in that region. We suspect that this is also happening elsewhere in the Southern Ocean. Because topographic control also comes with eddy generation, we bring forward that the southward migration of fronts is a macroscopic picture that eventually conceals changes in EKE, which are,

in the end, the most relevant for ecosystems. As a result, we recommend that studies on the impact of large ocean and climate changes onto regional hydrodynamics and ecosystems take into account the mesoscale processes that are at play.

Bibliography

Abernathey, R., Marshall, J., and Ferreira, D. (2011). The Dependence of Southern Ocean Meridional Overturning on Wind Stress. *Journal of Physical Oceanography*, 41(12):2261–2278.

Allan, L. E. (2011). *Trophodynamics of the benthic and hyperbenthic communities inhabiting the subantarctic Prince Edward Islands: stable isotope and fatty acid signatures*. PhD thesis, Rhodes University, Grahamstown, South Africa.

Allan, L. E., Froneman, W. P., Durgadoo, J. V., McQuaid, C. D., Ansorge, I. J., and Richoux, N. B. (2013). Critical indirect effects of climate change on sub-antarctic ecosystem functioning. *Ecology and evolution*, 3(9):2994–3004.

Ansorge, I., Durgadoo, J., and Pakhomov, E. (2009). Dynamics of physical and biological systems of the prince edward islands in a changing climate. In *Papers and Proceedings of the Royal Society of Tasmania*, volume 143, pages 15–18.

Ansorge, I., Froneman, P., and Durgadoo, J. (2012). The marine ecosystem of the subantarctic, prince edward islands. In *Marine Ecosystems*. InTech.

Ansorge, I., Jackson, J., Reid, K., Durgadoo, J., Swart, S., and Eberenz, S. (2014a). Evidence of a southward eddy corridor in the south-west Indian ocean. *Deep Sea Research Part II: Topical Studies in Oceanography*.

Ansorge, I. and Lutjeharms, J. (2002). The hydrography and dynamics of the ocean environment of the Prince Edward Islands (Southern Ocean). *Journal of Marine Systems*, 37(1-3):107–127.

Ansorge, I. and Lutjeharms, J. (2003). Eddies originating at the South-West Indian Ridge. *Journal of Marine Systems*, 39(1-2):1–18.

Ansorge, I. J., Durgadoo, J. V., and Treasure, A. M. (2014b). Sentinels to climate change. The need for monitoring at South Africa's Subantarctic laboratory. *South African Journal of Science*, 110(1-2):1–4.

Ansorge, I. J., Froneman, P. W., Bernard, K., Backeburg, B., Blake, J., Bernard, A., Lange, L., Bland, S., Burls, N., Gerber, R., Gildenhuys, S., Ludford, A., Manzoni, T., Robertson, E., Southey, D., Swart, S., Rensburg, D. V., and Wynne, S. (2004). An interdisciplinary cruise dedicated to understanding ocean eddies upstream of the Prince Edward Islands. (August):48–50.

Ansorge, I. J., Froneman, P. W., Pakhomov, E. A., Lutjeharms, J. R. E., Perissinotto, R., and van Ballegooyen, R. C. (1999). Physical-biological coupling in the waters surrounding the Prince Edward Islands (Southern Ocean). *Polar Biology*, 21(3):135–145.

Ansorge, I. J. and Lutjeharms, J. R. E. (2000). Twenty-five years of physical oceanographic research at the Prince Edward Islands.

Ansorge, I. J. and Lutjeharms, J. R. E. (2005). Direct observations of eddy turbulence at a ridge in the Southern Ocean. *Geophysical Research Letters*, 32(14).

Arakawa, A. and Lamb, V. R. (1977). Computational design of the basic dynamical processes of the UCLA general circulation model.

Atkinson, A., Siegel, V., Pakhomov, E., and Rothery, P. (2004). Long-term decline in krill stock and increase in salps within the Southern Ocean. *Nature*, 432(7013):100–103.

Barker, P. and Burrell, J. (1977). The opening of Drake Passage. *Marine Geology*, 25(1-3):15–34.

Belkin, I. M. and Gordon, A. L. (1996). Southern Ocean fronts from the Greenwich meridian to Tasmania. *Journal of Geophysical Research: Oceans*, 101(C2):3675–3696.

Boden, B. P. (1988). Observations of the island mass effect in the Prince Edward archipelago. *Polar Biology*, 9(1):61–68.

Böning, C. W., Dispert, A., Visbeck, M., Rintoul, S. R., and Schwarzkopf, F. U. (2008). The response of the Antarctic Circumpolar Current to recent climate change. *Nature Geoscience*, 1(12):864–869.

Bost, C. A., Cotté, C., Terray, P., Barbraud, C., Bon, C., Delord, K., Gimenez, O., Handrich, Y., Naito, Y., Guinet, C., and Weimerskirch, H. (2015). Large-scale climatic anomalies affect marine predator foraging behaviour and demography. *Nature Communications*, 6(1):8220.

Bost, C. A., Georges, J. Y., Guinet, C., Cherel, Y., Pütz, K., Charrassin, J. B., Handrich, Y., Zorn, T., Lage, J., and Maho, Y. L. (1997). Foraging habitat and food intake of satellite-tracked king penguins during the austral summer at Crozet Archipelago. *Marine Ecology Progress Series*, 150:21–33.

Branch, G. M., Attwood, C. G., Gianakouras, D., and Branch, M. L. (1993). Patterns in the benthic communities on the shelf of the sub-Antarctic Prince Edward Islands. *Polar Biology*, 13(1):23–34.

Capet, X., Chérubin, L., and Morel, Y. (2002). Influence of the Transport on the Instability of a Boundary Current. *Journal of Physical Oceanography*, 32(10):2806–2815.

Carton, X. (2001). Hydrodynamical Modeling Of Oceanic Vortices. *Surveys in Geophysics*, 22(3):179–263.

Cazenave, A. and Llovel, W. (2010). Contemporary Sea Level Rise. *Annual Review of Marine Science*, 2(1):145–173.

Chapman, C. C. (2014). Southern Ocean jets and how to find them: Improving and comparing common jet detection methods. *Journal of Geophysical Research: Oceans*, 119(7):4318–4339.

Chapman, C. C. (2017). New Perspectives on Frontal Variability in the Southern Ocean. *Journal of Physical Oceanography*, 47(5):1151–1168.

Chelton, D. B., DeSzoeke, R. A., Schlax, M. G., El Naggar, K., Siwertz, N., Chelton, D. B., DeSzoeke, R. A., Schlax, M. G., Naggar, K. E., and Siwertz, N. (1998). Geographical Variability of the First Baroclinic Rossby Radius of Deformation. *Journal of Physical Oceanography*, 28(3):433–460.

Chelton, D. B., Schlax, M. G., and Samelson, R. M. (2011). Global observations of nonlinear mesoscale eddies. *Progress in Oceanography*, 91(2):167–216.

Chelton, D. B., Schlax, M. G., Witter, D. L., and Richman, J. G. (1990). Geosat altimeter observations of the surface circulation of the Southern Ocean. *Journal of Geophysical Research*, 95(C10):17877.

Condy, P. R. (1981). Annual food consumption, and seasonal fluctuations in biomass of seals at Marion Island. *Mammalia*, 45(1):21–30.

Constable, A. J., Melbourne-Thomas, J., Corney, S. P., Arrigo, K. R., Barbraud, C., Barnes, D. K., Bindoff, N. L., Boyd, P. W., Brandt, A., Costa, D. P., et al. (2014). Climate change and Southern Ocean ecosystems I: how changes in physical habitats directly affect marine biota. *Global Change Biology*, 20(10):3004–3025.

Cooper, J. and Headland, R. K. (1991). A history of South African involvement in Antarctica and at the Prince Edward Islands. *South African Journal of Antarctic Research*, 21:77–91.

Cotté, C., D'Ovidio, F., Dragon, A. C., Guinet, C., and Lévy, M. (2015). Flexible preference of southern elephant seals for distinct mesoscale features within the Antarctic Circumpolar Current. *Progress in Oceanography*, 131:46–58.

Craneguy, P. and Park, Y.-H. (1999). Topographic control of the Antarctic Circumpolar Current in the south Indian Ocean. *Earth & Planetary Sciences*, 328:583–589.

da Silva, A., Young, C., and Levitus, S. (1994). Atlas of surface marine data 1994, Vol. 4: Anomalies of fresh water fluxes. *NOAA Atlas, NESDIS*.

de Boyer Montégut, C., Madec, G., Fischer, A. S., Lazar, A., and Iudicone, D. (2004). Mixed layer depth over the global ocean: An examination of profile data and a profile-based climatology. *Journal of Geophysical Research*, 109(C12):C12003.

de Szoeke, R. A. and Levine, M. D. (1981). The advective flux of heat by mean geostrophic motions in the Southern Ocean. *Deep Sea Research Part A. Oceanographic Research Papers*, 28(10):1057–1085.

Deacon, G. E. R. (1982). Physical and biological zonation in the Southern Ocean. *Deep Sea Research Part A, Oceanographic Research Papers*, 29(1):1–15.

Debreu, L., Marchesiello, P., Penven, P., and Cambon, G. (2012). Two-way nesting in split-explicit ocean models: Algorithms, implementation and validation. *Ocean Modelling*, 49-50:1–21.

Dong, S., Sprintall, J., Gille, S. T., Dong, S., Sprintall, J., and Gille, S. T. (2006). Location of the Antarctic Polar Front from AMSR-E Satellite Sea Surface Temperature Measurements. *Journal of Physical Oceanography*, 36(11):2075–2089.

Downes, S. M., Budnick, A. S., Sarmiento, J. L., and Farneti, R. (2011). Impacts of wind stress on the Antarctic Circumpolar Current fronts and associated subduction. 38(May):3–8.

Ducet, N., Le Traon, P. Y., and Reverdin, G. (2000). Global high-resolution mapping of ocean circulation from TOPEX/Poseidon and ERS-1 and -2. *Journal of Geophysical Research*, 105(C8):19477.

Duncombe Rae, C. M. (1989). Frontal systems encountered between southern Africa and the Prince Edward Islands during April/May 1987. *South African Journal of Antarctic Research*, 19:21–25.

Durack, P. J., Wijffels, S. E., Durack, P. J., and Wijffels, S. E. (2010). Fifty-Year Trends in Global Ocean Salinities and Their Relationship to Broad-Scale Warming. *Journal of Climate*, 23(16):4342–4362.

Durgadoo, J. V., Ansorge, I. J., De Cuevas, B. A., Lutjeharms, J. R., and Coward, A. C. (2011). Decay of eddies at the South-West Indian Ridge. *South African Journal of Science*, 107(11/12):10 Pages.

Durgadoo, J. V., Ansorge, I. J., and Lutjeharms, J. R. (2010). Oceanographic observations of eddies impacting the Prince Edward Islands, South Africa. *Antarctic Science*, 22(03):211–219.

Egbert, G. D., Bennett, A. F., and Foreman, M. G. G. (1994). TOPEX/POSEIDON tides estimated using a global inverse model. *Journal of Geophysical Research*, 99(C12):24821.

Egbert, G. D., Erofeeva, S. Y., Egbert, G. D., and Erofeeva, S. Y. (2002). Efficient Inverse Modeling of Barotropic Ocean Tides. *Journal of Atmospheric and Oceanic Technology*, 19(2):183–204.

Farneti, R., Delworth, T. L., Rosati, A. J., Griffies, S. M., Zeng, F., Farneti, R., Delworth, T. L., Rosati, A. J., Griffies, S. M., and Zeng, F. (2010). The Role of Mesoscale Eddies in the Rectification of the Southern Ocean Response to Climate Change. *Journal of Physical Oceanography*, 40(7):1539–1557.

Froneman, P. W., Ansorge, I. J., Pakhomov, E. A., and Lutjeharms, J. R. E. (1999). Plankton community structure in the physical environment surrounding the Prince Edward Islands (Southern Ocean). *Polar Biology*, 22(3):145–155.

Fyfe, J. C., Boer, G. J., and Flato, G. M. (1999). The arctic and antarctic oscillations and their projected changes under global warming. *Geophysical Research Letters*, 26(11):1601–1604.

Fyfe, J. C. and Saenko, O. A. (2006). Simulated changes in the extratropical Southern Hemisphere winds and currents. *Geophysical Research Letters*, 33(6):L06701.

Garabato, A. C. N., Polzin, K. L., King, B. A., Heywood, K. J., and Visbeck, M. (2004). Widespread Intense Turbulent Mixing in the Southern Ocean. *Science*, 303(5655).

Gent, P. R. (2016). Effects of Southern Hemisphere Wind Changes on the Meridional Overturning Circulation in Ocean Models. *Annual Review of Marine Science*, 8(1):79–94.

Gille, S. T. (1994). Mean sea surface height of the Antarctic Circumpolar Current from Geosat data: Method and application. *Journal of Geophysical Research*, 99(C9):18255.

Gille, S. T. (2002). Warming of the Southern Ocean since the 1950s. *Science*, 295(5558):1275–7.

Gille, S. T. (2003). Float Observations of the Southern Ocean. Part II: Eddy Fluxes. *Journal of Physical Oceanography*, 33(6):1182–1196.

Gille, S. T. (2008). Decadal-Scale Temperature Trends in the Southern Hemisphere Ocean. *Journal of Climate*, 21(18):4749–4765.

Gille, S. T. (2014). Meridional displacement of the Antarctic Circumpolar Current. *Philosophical transactions. Series A, Mathematical, physical, and engineering sciences*, 372(2019):20130273.

Gorgues, T., Menkes, C., Aumont, O., Vialard, J., Dandonneau, Y., and Bopp, L. (2005). Biogeochemical impact of tropical instability waves in the equatorial Pacific. *Geophysical Research Letters*, 32(24):L24615.

Gouretski, V. V. and Danilov, A. I. (1994). Characteristics of warm rings in the African sector of the Antarctic Circumpolar Current. *Deep-Sea Research Part I*, 41(8):1131–1157.

Graham, R. M. (2014). *The role of the Antarctic in the global climate system*. PhD thesis, Stockholm University, Department of Geological Sciences.

Graham, R. M. and De Boer, A. M. (2013). The dynamical subtropical front. *Journal of Geophysical Research: Oceans*, 118(10):5676–5685.

Graham, R. M., De Boer, A. M., Heywood, K. J., Chapman, M. R., and Stevens, D. P. (2012). Southern Ocean fronts: Controlled by wind or topography? *Journal of Geophysical Research: Oceans*, 117(8):1–14.

Guinet, C., Xing, X., Walker, E., Monestiez, P., Marchand, S., Picard, B., Jaud, T., Authier, M., Cotté, C., Dragon, A. C., Diamond, E., Antoine, D., Lovell, P., Blain, S., D'Ortenzio, F., and Claustre, H. (2013). Calibration procedures and first dataset of Southern Ocean chlorophyll a profiles collected by elephant seals equipped with a newly developed CTD-fluorescence tags. *Earth System Science Data*, 5(1):15–29.

Hallberg, R., Gnanadesikan, A., Hallberg, R., and Gnanadesikan, A. (2006). The Role of Eddies in Determining the Structure and Response of the Wind-Driven Southern Hemisphere Overturning: Results from the Modeling Eddies in the Southern Ocean (MESO) Project. *Journal of Physical Oceanography*, 36(12):2232–2252.

Halo, I., Penven, P., Backeberg, B., Ansorge, I., Shillington, F., and Roman, R. (2014). Mesoscale eddy variability in the southern extension of the East Madagascar Current: Seasonal cycle, energy conversion terms, and eddy mean properties. *Journal of Geophysical Research: Oceans*, 119(10):7324–7356.

Haumann, F., Gruber, N., Münnich, M., Frenger, I., and Kern, S. (2016). Sea-ice transport driving Southern Ocean salinity and its recent trends. *Nature*.

Helm, K. P., Bindoff, N. L., and Church, J. A. (2010). Changes in the global hydrological-cycle inferred from ocean salinity. *Geophysical Research Letters*, 37(18).

Hofmeyr, G. J. G., Bester, M. N., Makhado, A. B., and Pistorius, P. A. (2006). Population changes in Subantarctic and Antarctic fur seals at Marion Island. *South African Journal of Wildlife Research*, 36(1):55–68.

Hogg, A. M., Meredith, M. P., Chambers, D. P., Abrahamsen, E. P., Hughes, C. W., and Morrison, A. K. (2015). Recent trends in the Southern Ocean eddy field. *Journal of Geophysical Research: Oceans*, 120(1):257–267.

Hogg, A. M. C., Meredith, M. P., Blundell, J. R., Wilson, C., Hogg, A. M. C., Meredith, M. P., Blundell, J. R., and Wilson, C. (2008). Eddy Heat Flux in the Southern Ocean: Response to Variable Wind Forcing. *Journal of Climate*, 21(4):608–620.

Holland, M. M., Landrum, L., Kostov, Y., and Marshall, J. (2017). Sensitivity of Antarctic sea ice to the Southern Annular Mode in coupled climate models. *Climate Dynamics*, 49(5-6):1813–1831.

Hoskins, B. J., Karoly, D. J., Hoskins, B. J., and Karoly, D. J. (1981). The Steady Linear Response of a Spherical Atmosphere to Thermal and Orographic Forcing. *Journal of the Atmospheric Sciences*, 38(6):1179–1196.

Hughes, C. W. and Ash, E. R. (2001). Eddy forcing of the mean flow in the Southern Ocean. *Journal of Geophysical Research: Oceans*, 106(C2):2713–2722.

Jacobs, S. S., Giulivi, C. F., Jacobs, S. S., and Giulivi, C. F. (2010). Large Multidecadal Salinity Trends near the Pacific–Antarctic Continental Margin. *Journal of Climate*, 23(17):4508–4524.

Jacobs, S. S., Giulivi, C. F., and Mele, P. A. (2002). Freshening of the Ross Sea during the late 20th century. *Science (New York, N.Y.)*, 297(5580):386–9.

Jayne, S. R. and Marotzke, J. (2002). The oceanic eddy heat transport. *Journal of Physical Oceanography*, 32(12):3328–3345.

Jones, D. C., Ito, T., and Lovenduski, N. S. (2011). The transient response of the Southern Ocean pycnocline to changing atmospheric winds. *Geophysical Research Letters*, 38(15).

Jonker, F. C. and Bester, M. N. (1998). Seasonal movements and foraging areas of adult southern female elephant seals, Mirounga leonina, from Marion Island. *Antarctic Science*, 10(01):21–30.

José, Y., Aumont, O., Machu, E., Penven, P., Moloney, C., and Maury, O. (2014). Influence of mesoscale eddies on biological production in the Mozambique Channel: Several contrasted examples from a coupled ocean-biogeochemistry model. *Deep Sea Research Part II: Topical Studies in Oceanography*, 100:79–93.

Joyce, T., Patterson, S., and Millard, R. (1981). Anatomy of a cyclonic ring in the drake passage. *Deep Sea Research Part A. Oceanographic Research Papers*, 28(11):1265–1287.

Keffer, T. and Holloway, G. (1988). Estimating southern ocean eddy flux of heat and salt from satellite altimetry. *Nature*, 332(6165):624–626.

Khatiwala, S., Tanhua, T., Mikaloff Fletcher, S., Gerber, M., Doney, S. C., Graven, H. D., Gruber, N., McKinley, G. A., Murata, A., Ríos, A. F., and Sabine, C. L. (2013). Global ocean storage of anthropogenic carbon. *Biogeosciences*, 10(4):2169–2191.

Kim, Y. S. and Orsi, A. H. (2014). On the Variability of Antarctic Circumpolar Current Fronts Inferred from 1992–2011 Altimetry*. *Journal of Physical Oceanography*, 44(12):3054–3071.

Kuhlbrodt, T., Griesel, a., Montoya, M., Levermann, a., Hofmann, M., and Rahmstorf, S. (2007). On the driving processes of the Atlantic meridional overturning circulation. *Atlantic*, 45(2004):RG2001.

Lacasce, J. H. (2000). Floats and f/h. *Journal of Marine Research*, 58(1):61–95.

Large, W. G., McWilliams, J. C., and Doney, S. C. (1994). Oceanic vertical mixing: A review and a model with a nonlocal boundary layer parameterization. *Reviews of Geophysics*, 32(4):363.

Laubscher, R. K., Perissinotto, R., and McQuaid, C. D. (1993). Phytoplankton production and biomass at frontal zones in the Atlantic sector of the Southern Ocean. *Polar Biology*, 13(7):471–481.

Le Quéré, C., Rödenbeck, C., Buitenhuis, E. T., Conway, T. J., Langenfelds, R., Gomez, A., Labuschagne, C., Ramonet, M., Nakazawa, T., Metzl, N., Gillett, N., and Heimann, M. (2007). Saturation of the Southern Ocean CO2 Sink Due to Recent Climate Change. *Science*, 316(5832).

Le Quéré, C., Takahashi, T., Buitenhuis, E. T., Rödenbeck, C., and Sutherland, S. C. (2010). Impact of climate change and variability on the global oceanic sink of CO2. *Global Biogeochemical Cycles*, 24(4):n/a–n/a.

le Roux, P. C. and McGeoch, M. A. (2008). Changes in climate extremes, variability and signature on sub-Antarctic Marion Island. *Climatic Change*, 86(3-4):309–329.

Le Traon, P., Nadal, F., and Ducet, N. (1998). An Improved Mapping Method of Multi-satellite Altimeter Data. *Atmospheric, Journal of Technology, Oceanic*, pages 522–534.

Lee, M.-M., Nurser, A. J. G., Coward, A. C., and de Cuevas, B. A. (2007). Eddy Advective and Diffusive Transports of Heat and Salt in the Southern Ocean. *Journal of Physical Oceanography*, 37(5):1376–1393.

Lévy, M., Klein, P., Tréguier, A.-M., Iovino, D., Madec, G., Masson, S., and Takahashi, K. (2010). Modifications of gyre circulation by sub-mesoscale physics. *Ocean Modelling*, 34(1-2):1–15.

Lovenduski, N. S. and Gruber, N. (2005). Impact of the Southern Annular Mode on Southern Ocean circulation and biology. *Geophysical Research Letters*, 32(11):1–4.

Lutjeharms, J. (1985). Location of frontal systems between Africa and Antarctica: some preliminary results. *Deep Sea Research Part A. Oceanographic Research Papers*, 32(12):1499–1509.

Lutjeharms, J. and Baker, D. (1980). A statistical analysis of the meso-scale dynamics of the Southern Ocean. *Deep Sea Research Part A. Oceanographic Research Papers*, 27(2):145–159.

Marchesiello, P., McWilliams, J. C., Shchepetkin, A., Physics, P., and Angeles, L. (2003). Equilibrium Structure and Dynamics of the California Current System. *Journal of Physical Oceanography*, 33(4):753–783.

Marshall, G. J. (2003). Trends in the Southern Annular Mode from Observations and Reanalyses. *Journal of Climate*, 16(24):4134–4143.

Marshall, G. J. (2016). The climate data guide: Marshall southern annular mode (sam) index (station-based). National Center for Atmospheric Research Staff (Eds), Retrieved from *https://climatedataguide.ucar.edu/climate-data/marshall-southern-annular-mode-sam-index-station-based*.

Marshall, G. J. and Speer, K. (2012). Closure of the meridional overturning circulation through Southern Ocean upwelling. *Nature Geoscience*, 5(3):171–180.

McDougal, I. (1971). Geochronology. In van Zinderen Bakker, E. M., Winterbottom, J. M., and Dyer, R. A., editors, *Marion and Prince Edward Islands: Report on the South African Biological and Geological Expeditions, 1965-1966*, pages 72–77. Cape Town, balkema edition.

McGillicuddy, D. J., Anderson, L. A., Bates, N. R., Bibby, T., Buesseler, K. O., Carlson, C. A., Davis, C. S., Ewart, C., Falkowski, P. G., Goldthwait, S. A., Hansell, D. A., Jenkins, W. J., Johnson, R., Kosnyrev, V. K., Ledwell, J. R., Li, Q. P., Siegel, D. A., and Steinberg, D. K. (2007). Eddy/Wind Interactions Stimulate Extraordinary Mid-Ocean Plankton Blooms. *Science*, 316(5827).

McQuaid, C. D. and Froneman, P. W. (2008). Biology in the oceanographic environment. In Chown, S. L. and Froneman, P. W., editors, *The Prince Edward Islands - Land-Sea Interactions in a Changing Ecosystem*, pages 97–120. Stellenbosch, sun press edition.

Melet, A., Hallberg, R., Legg, S., and Nikurashin, M. (2014). Sensitivity of the Ocean State to Lee Wave–Driven Mixing. *Journal of Physical Oceanography*, 44(3):900–921.

Mélice, J. L., Lutjeharms, J. R. E., Rouault, M., and Ansorge, I. J. (2003). Sea-surface temperatures at the sub-Antarctic islands Marion and Gough during the past 50 years. *South African Journal of Science*, 99(7-8):363–366.

Meredith, M. P. and Hogg, A. M. (2006). Circumpolar response of Southern Ocean eddy activity to a change in the Southern Annular Mode. *Geophysical Research Letters*, 33(16):2–5.

Meredith, M. P., Naveira Garabato, A. C., Hogg, A. M., and Farneti, R. (2011). Sensitivity of the overturning circulation in the Southern Ocean to decadal changes in wind forcing. *Journal of Climate*, 25(1):99–110.

Moore, J. K., Abbott, M. R., and Richman, J. G. (1999). Location and dynamics of the Antarctic Polar Front from satellite sea surface temperature data. *Journal of Geophysical Research: Oceans*, 104(C2):3059–3073.

Morrison, A. K., Fr??licher, T. L., and Sarmiento, J. L. (2015). Upwelling in the Southern Ocean. *Physics Today*, 68(1):27–32.

Morrow, R., Donguy, J.-R., Chaigneau, A., and Rintoul, S. R. (2004). Cold-core anomalies at the subantarctic front, south of Tasmania. *Deep Sea Research Part I: Oceanographic Research Papers*, 51(11):1417–1440.

Morrow, R., Valladeau, G., and Sallee, J.-B. (2008). Observed subsurface signature of Southern Ocean sea level rise. *Progress in Oceanography*, 77(4):351–366.

Nagata, Y., Michida, Y., and Umimura, Y. (1988). Variation of Positions and Structures of the Oceanic Fronts in the Indian Ocean Sector of the Southern Ocean in the Period from 1965 to 1987. *Antarctic Ocean and ressources variability*, pages 92–98.

Nel, D. C., Lutjeharms, J. R., Pakhomov, E. A., Ansorge, I. J., Ryan, P. G., and Klages, N. T. (2001). Exploitation of mesoscale oceanographic features by grey-headed albatross Thalassarche chrysostoma in the southern Indian Ocean. *Marine Ecology Progress Series*, 217:15–26.

Nikurashin, M. and Ferrari, R. (2013). Overturning circulation driven by breaking internal waves in the deep ocean. *Geophysical Research Letters*, 40(12):3133–3137.

Nikurashin, M., Ferrari, R., Nikurashin, M., and Ferrari, R. (2010). Radiation and Dissipation of Internal Waves Generated by Geostrophic Motions Impinging on Small-Scale Topography: Theory. *Journal of Physical Oceanography*, 40(5):1055–1074.

Nikurashin, M., Vallis, G. K., and Adcroft, A. (2012). Routes to energy dissipation for geostrophic flows in the Southern Ocean. *Nature Geoscience*, 6(1):48–51.

Nowlin, W. D., Worley, S. J., and Whitworth, T. (1985). Methods for making point estimates of eddy heat flux as applied to the Antarctic Circumpolar Current. *Journal of Geophysical Research*, 90(C2):3305.

Okubo, A. (1970). Horizontal dispersion of floatable particles in the vicinity of velocity singularities such as convergences. *Deep Sea Research and Oceanographic Abstracts*, 17(3):445–454.

Orsi, A. H., Nowlin, W. D., and Whitworth, T. (1993). On the circulation and stratification of the Weddell Gyre. *Deep Sea Research Part I: Oceanographic Research Papers*, 40(1):169–203.

Orsi, A. H., Whitworth, T., and Nowlin, W. D. (1995). On the meridional extent and fronts of the Antarctic Circumpolar Current. *Deep Sea Research Part I: Oceanographic Research Papers*, 42(5):641–673.

Pakhomov, E. A., Ansorge, I. J., and Froneman, P. W. (2000). Variability in the inter-island environment of the Prince Edward Islands (Southern Ocean). *Polar Biology*, 23(9):593–603.

Pakhomov, E. A. and Chown, S. L. (2003). The Prince Edward Islands: Southern Ocean oasis. *Ocean Yearbook*, 17(1):348–379.

Pakhomov, E. A., Froneman, P., and McQuaid, C. (2001). Prince Edward Islands life support system and variability of living resource systems in the Southern Ocean. *South African National Antarctic Research Programme (SANARP). Final Project report*, pages 1–53.

Park, Y.-H., Charriaud, E., Craneguy, P., and Kartavtseff, A. (2001). Fronts, transport, and Weddell Gyre at 30°E between Africa and Antarctica. *Journal of Geophysical Research*, 106(C2):2857.

Patara, L., Böning, C. W., and Biastoch, A. (2016). Variability and trends in Southern Ocean eddy activity in 1/12° ocean model simulations. *Geophysical Research Letters*, 43(9):4517–4523.

Penven, P., Debreu, L., Marchesiello, P., and McWilliams, J. C. (2006). Evaluation and application of the ROMS 1-way embedding procedure to the central california upwelling system. *Ocean Modelling*, 12(1-2):157–187.

Penven, P., Echevin, V., Pasapera, J., Colas, F., and Tam, J. (2005). Average circulation, seasonal cycle, and mesoscale dynamics of the Peru Current System: A modeling approach. *Journal of Geophysical Research*, 110(C10):C10021.

Perissinotto, R. and Duncombe Rae, C. (1990). Occurrence of anticyclonic eddies on the Prince Edward Plateau (Southern Ocean): effects on phytoplankton biomass and production. *Deep Sea Research Part A. Oceanographic Research Papers*, 37(5):777–793.

Perissinotto, R., Lutjeharms, J., and van Ballegooyen, R. (2000). Biological–physical interactions and pelagic productivity at the Prince Edward Islands, Southern Ocean. *Journal of Marine Systems*, 24(3-4):327–341.

Phillips, H. E., Rintoul, S. R., Phillips, H. E., and Rintoul, S. R. (2000). Eddy Variability and Energetics from Direct Current Measurements in the Antarctic Circumpolar Current South of Australia. *Journal of Physical Oceanography*, 30(12):3050–3076.

Pollard, R. T. and Read, J. F. (2001). Circulation pathways and transports of the Southern Ocean in the vicinity of the Southwest Indian Ridge. *Journal of Geophysical Research*, 106(C2):2881–2898.

Pollard, R. T., Venables, H. J., Read, J. F., and Allen, J. T. (2007). Large-scale circulation around the Crozet Plateau controls an annual phytoplankton bloom in the Crozet Basin. *Deep-Sea Research Part II: Topical Studies in Oceanography*, 54(18-20):1915–1929.

Rintoul, S. R. and Naveira Garabato, A. C. (2013). Dynamics of the Southern Ocean Circulation. In *Ocean Circulation and Climate: A 21st Century Perspective*, volume 103, pages 471–492. Elsevier Ltd., 2 edition.

Rintoul, S. R. and Sokolov, S. (2001). Baroclinic transport variability of the Antarctic Circumpolar Current south of Australia (WOCE repeat section SR3). *Journal of Geophysical Research: Oceans*, 106(C2):2815–2832.

Rio, M.-H., Mulet, S., and Picot, N. (2014). Beyond GOCE for the ocean circulation estimate: Synergetic use of altimetry, gravimetry, and in situ data provides new insight into geostrophic and Ekman currents. *Geophysical Research Letters*, 41(24):8918–8925.

Risien, C. M., Chelton, D. B., Risien, C. M., and Chelton, D. B. (2008). A Global Climatology of Surface Wind and Wind Stress Fields from Eight Years of QuikSCAT Scatterometer Data. *Journal of Physical Oceanography*, 38(11):2379–2413.

Rouault, M., Mélice, J. L., Reason, C., and Lutjeharms, J. (2005). Climate variability at Marion Island, Southern Ocean, since 1960. *Journal of Geophysical Research*, 110(C5):C05007.

Roullet, G., Capet, X., and Maze, G. (2014). Global interior eddy available potential energy diagnosed from Argo floats. *Geophysical Research Letters*, 41(5):1651–1656.

Ryan, P. G. and Bester, M. N. (2008). Pelagic predators. In Chown, S. L. and Froneman, P. W., editors, *The Prince Edward Islands - Land-Sea Interactions in a Changing Ecosystem*, pages 121–164. Sun press edition.

Ryan, P. G., Jones, M. G., Dyer, B. M., Upfold, L., and Crawford, R. J. (2009). Recent population estimates and trends in numbers of albatrosses and giant petrels breeding at the sub-Antarctic Prince Edward Islands. *African Journal of Marine Science*, 31(3):409–417.

Sallée, J. B., Speer, K., and Morrow, R. (2008). Response of the Antarctic Circumpolar Current to Atmospheric Variability. *Journal of Climate*, 21(12):3020–3039.

Sallée, J. B., Speer, K. G., and Rintoul, S. R. (2010). Zonally asymmetric response of the Southern Ocean mixed-layer depth to the Southern Annular Mode. *Nature Geoscience*, 3(4):273–279.

Schmittner, A., Chiang, J. C. H., and Hemming, S. R. (2013). Introduction: The Ocean's Meridional Overturning Circulation. In Schmittner, A., Chiang, J. C. H., and Hemming, S. R., editors, *Ocean Circulation: Mechanisms and Impacts - Past and Future Changes of Meridional Overturning*, pages 1–4. American Geophysical Union, Washington, D. C.

Sen Gupta, A., England, M. H., Gupta, A. S., and England, M. H. (2006). Coupled Ocean–Atmosphere–Ice Response to Variations in the Southern Annular Mode. *Journal of Climate*, 19(18):4457–4486.

Shao, A. E., Gille, S. T., Mecking, S., and Thompson, L. (2015). Properties of the Subantarctic Front and Polar Front from the skewness of sea level anomaly. *Journal of Geophysical Research: Oceans*, 120(7):5179–5193.

Shchepetkin, A. F. and McWilliams, J. C. (2005). The regional oceanic modeling system (ROMS): a split-explicit, free-surface, topography-following-coordinate oceanic model. *Ocean Modelling*, 9(4):347–404.

Shchepetkin, A. F., McWilliams, J. C., Shchepetkin, A. F., and McWilliams, J. C. (1998). Quasi-Monotone Advection Schemes Based on Explicit Locally Adaptive Dissipation. *Monthly Weather Review*, 126(6):1541–1580.

Siegert, M. J., Barrett, P., DeConto, R., Dunbar, R., Ó Cofaigh, C., Passchier, S., and Naish, T. (2008). Recent advances in understanding Antarctic climate evolution. *Antarctic Science*, 20(04).

Simmons, S., Crocker, D., Kudela, R., and Costa, D. (2007). Linking foraging behaviour of the northern elephant seal with oceanography and bathymetry at mesoscales. *Marine Ecology Progress Series*, 346:265–275.

Simpkins, G. R., Ciasto, L. M., Thompson, D. W. J., England, M. H., Simpkins, G. R., Ciasto, L. M., Thompson, D. W. J., and England, M. H. (2012). Seasonal Relationships between Large-Scale Climate Variability and Antarctic Sea Ice Concentration. *Journal of Climate*, 25(16):5451–5469.

Sinha, B. and Richards, K. J. (1999). Jet Structure and Scaling in Southern Ocean Models. *Journal of Physical Oceanography*, 29(6):1143–1155.

Smith, V. R. (2002). Climate Change in the Sub-Antarctic: An Illustration from Marion Island. *Climatic Change*, 52(3):345–357.

Sokolov, S. and Rintoul, S. R. (2007). Multiple Jets of the Antarctic Circumpolar Current South of Australia*. *Journal of Physical Oceanography*, 37(5):1394–1412.

Sokolov, S. and Rintoul, S. R. (2009a). Circumpolar structure and distribution of the Antarctic Circumpolar Current fronts: 1. Mean circumpolar paths. *Journal of Geophysical Research*, 114(C11):C11018.

Sokolov, S. and Rintoul, S. R. (2009b). Circumpolar structure and distribution of the antarctic circumpolar current fronts: 1. Mean circumpolar paths. *Journal of Geophysical Research: Oceans*, 114(11):C11018.

Sokolov, S. and Rintoul, S. R. (2009c). Circumpolar structure and distribution of the Antarctic Circumpolar Current fronts: 2. Variability and relationship to sea surface height. 114:1–15.

Speer, K., Rintoul, S. R., and Sloyan, B. (2000). The Diabatic Deacon Cell*. *Journal of Physical Oceanography*, 30(12):3212–3222.

Sprintall, J. (2008). Long-term trends and interannual variability of temperature in Drake Passage. *Progress in Oceanography*, 77(4):316–330.

Straub, D. N. and Straub, D. N. (1993). On the Transport and Angular Momentum Balance of Channel Models of the Antarctic Circumpolar Current. *Journal of Physical Oceanography*, 23(4):776–782.

Sumner, P. D., Meiklejohn, K. I., Boelhouwers, J. C., and Hedding, D. W. (2004). Climate change melts Marion Island's snow and ice. *South African Journal of Science*, 100(7-8):395–398.

Sun, C. (2002). Heat flux carried by the Antarctic Circumpolar Current mean flow. *Journal of Geophysical Research*, 107(C9):3119.

Swart, N. C., Ansorge, I. J., and Lutjeharms, J. R. E. (2008). Detailed characterization of a cold Antarctic eddy. *Journal of Geophysical Research*, 113(C1):C01009.

Swart, N. C. and Fyfe, J. C. (2012). Observed and simulated changes in the Southern Hemisphere surface westerly wind-stress. *Geophysical Research Letters*, 39(16).

Swart, S., Speich, S., Ansorge, I. J., and Lutjeharms, J. R. E. (2010). An altimetry-based gravest empirical mode south of Africa: 1. Development and validation. *Journal of Geophysical Research*, 115(C3):C03002.

Talley, L. D., Pickard, G. L., Emery, W. J., and Swift, J. H. (2011). *Descriptive Physical Oceanography*. Elsevier.

Thompson, D. W. J. and Solomon, S. (2002). Interpretation of Recent Southern Hemisphere Climate Change. *Science*, 296(5569).

Thompson, D. W. J., Wallace, J. M., Thompson, D. W. J., and Wallace, J. M. (2000). Annular Modes in the Extratropical Circulation. Part I: Month-to-Month Variability*. *Journal of Climate*, 13(5):1000–1016.

Thompson, S. R. (1993). Estimation of the transport of heat in the southern ocean using a fine-resolution numerical model. *Journal of physical oceanography*, 23(11):2493–2497.

Tollefson, J. (2016). The hostile ocean that slowed climate change. *Nature*, 539:346–348.

Trenberth, K. E., Jones, P., Ambenje, P., Bojariu, R., Easterling, D., Klein Tank, A., Parker, D., Rahimzadeh, F., Renwick, J., Rusticucci, M., Soden, B., Zhai, P., and Mote, P. (2007). Observations: surface and atmospheric climate change. Chapter 3. In Solomon, S., Qin, D., Manning, M., Chen, Z., Marquis, M., Averyt, K., Tignor, M., and Miller, H., editors, *Climate Change 2007: The Physical Science Basis. Contribution of Working Group I to the Fourth Assessment Report of the Intergovernmental Panel on Climate Change*, number 236 - 336, pages 235–336. Cambridge University Press, Cambridge, United Kingdom and New York, NY, USA.

Tynan, C. T. (1998). Ecological importance of the Southern Boundary of the Antarctic Circumpolar Current. *Nature*, 392(6677):708–710.

Volkov, D. L., Lee, T., and Fu, L.-L. (2008). Eddy-induced meridional heat transport in the ocean. *Geophysical Research Letters*, 35(20).

von der Meden, C. E. O., Atkinson, L. J., Branch, G. M., Asdar, S., Ansorge, I. J., and van den Berg, M. (2017). Long-term change in epibenthic assemblages at the Prince Edward Islands: a comparison between 1988 and 2013. *Polar Biology*, 40(11):2171–2185.

Weiss, J. (1991). The dynamics of enstrophy transfer in two-dimensional hydrodynamics. *Physica D: Nonlinear Phenomena*, 48(2-3):273–294.

Whitworth, T. and Peterson, R. G. (1985). Volume Transport of the Antarctic Circumpolar Current from Bottom Pressure Measurements. *Journal of Physical Oceanography*, 15(6):810–816.

Williams, A. J., Siegfried, W. R., Burger, A. E., and Berruti, A. (1979). The Prince Edward Islands: A sanctuary for seabirds in the Southern Ocean. *Biological Conservation*, 15(1):59–71.